A&A 656, A148 (2021)
https://doi.org/10.1051/0004-6361/202141616
© ESO 2021

Astronomy & Astrophysics

# Mechanisms for gas-phase molecular formation of neutral formaldehyde ($H_2CO$) in cold astrophysical regions

Juan C. Ramal-Olmedo[1,2], César A. Menor-Salván[2,3], and Ryan C. Fortenberry[4]

[1] Departamentos de Física & Matemáticas y de Ingeniería Automática, Universidad de Alcalá, 28805 Alcalá de Henares, Madrid, Spain
[2] Departamento de Biología de Sistemas, Instituto de Investigación Química "Andrés del Rio" (IQAR), Universidad de Alcalá, 28805 Alcalá de Henares, Madrid, Spain
e-mail: juan.ramal@edu.uah.es; cesar.menor@uah.es
[3] NSF-NASA Center for Chemical Evolution, Georgia Institute of Technology, Atlanta, GA 33000, USA
[4] Department of Chemistry & Biochemistry, University of Mississippi, University, MS 38677, USA
e-mail: r410@olemiss.edu

Received 23 June 2021 / Accepted 27 August 2021

**ABSTRACT**

*Context.* Formaldehyde is a potential biogenic precursor involved in prebiotic chemical evolution. The cold conditions of the interstellar medium (ISM) allow $H_2CO$ to be reactive, playing a significant role as a chemical intermediate in formation pathways leading to interstellar complex organic molecules. However, gas-phase molecular formation mechanisms in cold regions of the ISM are poorly understood.

*Aims.* We computationally determine the most favored gas-phase molecular formation mechanisms at local thermodynamic equilibrium conditions that can produce the detected amounts of $H_2CO$ in diffuse molecular clouds (DMCs), in dark, cold, and dense molecular clouds (DCDMCs), and in three regions of circumstellar envelopes of low-mass protostars (CELMPs).

*Methods.* The potential energy surfaces, thermodynamic functions, and single-point energies for transition states were calculated at the CCSD(T)-F12/cc-pVTZ-F12 and MP2/aug-cc-pVDZ levels of theory and basis sets. Molecular thermodynamics and related partition functions were obtained by applying the Maxwell-Boltzmann quantum statistics theory from energies computed at CCSD(T)-F12/cc-pVTZ-F12 with corrections for zero-point energy. A literature review on detected abundances of reactants helped us to propose the most favorable formation routes.

*Results.* The most probable reactions that produce $H_2CO$ in cold astrophysical regions are: $^1CH_2 + {}^{\cdot 3}O_2 \rightarrow {}^1H_2CO + O\cdot(^3P)$ in DMCs, ${}^{\cdot 3}CH_2 + {}^{\cdot 3}O_2 \rightarrow {}^1H_2CO + \cdot O(^3P)$ in DCDMCs, and $\cdot CH_3 + \cdot O(^3P) \rightarrow {}^1H_2CO + \cdot H$ in region III, $\cdot CH_3 + \cdot O(^1D) \rightarrow {}^1H_2CO + \cdot H$ in region II, and $^1CH_2 + {}^{\cdot 3}O_2 \rightarrow {}^1H_2CO + \cdot O(^3P)$ in region I belonging to CELMPs.

*Conclusions.* Quantum chemical calculations suggest that the principal carbonaceous precursors of $H_2CO$ in cold regions for the gas-phase are $CH_2(a^1A_1)$, and $\cdot CH_2(X^3B_1)$ combined with $\cdot O_2(^3\Sigma_g)$ and $\cdot CH_3(^2A'') + \cdot O(^3P)$ / $O(^1D)$. Reactions based on more complex reagents yield less effective thermodynamics in the gas-phase $H_2CO$ molecular formation.

**Key words.** astrobiology – astrochemistry – ISM: molecules – molecular processes

## 1. Introduction

After the early discovery of sugar formation by base-catalyzed aldol condensations of formaldehyde ($H_2CO$) in the presence of calcium (Butlerow 1861), collectively known as formose reactions (Loew 1889), $H_2CO$ has been considered as a plausible primordial source of sugars on prebiotic Earth (Delidovich et al. 2014). Additionally, the syntheses of glycine ($C_2H_5NO_2$) and glycolic acid ($C_2H_4O_3$) by Strecker synthesis require $H_2CO$, as well as hydrogen cyanide (HCN), ammonia ($NH_3$), or other amines and aldehydes for the formation of amino acids (Choughuley et al. 1975). The Strecker-type syntheses and the related Bucherer-Bergs synthesis from alpha-aminonitriles (Ruiz-Mirazo et al. 2014) could explain the presence of amino acids in meteorites and model prebiotic reactions including the classic Miller-Urey experiment (Miller 1953; Oró et al. 1959; Choughuley et al. 1975). The formose and Strecker reactions highlight the relevance of formaldehyde as a key precursor in prebiotic chemical evolution (Menor-Salván 2018), but its role during bio-genesis on Earth is still a subject of much debate (Cleaves II 2008). Recently, the formation of sugar mixtures compatible with formose reactions has been observed after ultraviolet irradiation of interstellar ices (Meinert et al. 2016) as well, and this might further result in formaldehyde oligomerization (Furukawa et al. 2019). These findings highlight the possible relevance of formaldehyde in the interstellar medium (ISM) and its reactions in current prebiotic chemical evolution models. The origin of formaldehyde itself is less clear.

The presence of $H_2CO$ in the ISM was first reported in 1969 by Snyder et al. (1969) from 15 radio sources with galactic and extragalactic origins, becoming the first organic polyatomic molecule (OPM) identified in the ISM. Since then, it has been detected through absorption and emission bands as continually being present in vast and varied astrophysical objects, such as molecular clouds, envelopes of low- and high-mass protostars, commentary media, and asteroids (see the main detection of formaldehyde and references therein in Appendix A). Consequently, $H_2CO$ is recognized as one of the most abundant OPMs

known in space (Mangum et al. 2008). Due to its ubiquity, $H_2CO$ and some of its isotopologs (e.g., $H_2{}^{13}CO$; $H_2{}^{13}C^{16}O$; $H_2{}^{12}C^{17}O$ or $H_2C^{18}O$), Zuckerman et al. (1969); Maret (2003); Blair et al. (2008) are commonly selected for tracing and modeling the astrophysical properties of the gases (e.g., kinetic energy, kinetic temperature, and density) in objects such as galaxies (Shuter 1982; Muhle et al. 2007), cold and dense molecular clouds (Tang et al. 2017), and in star-forming regions (Wiebe et al. 2008). Formaldehyde is known to be a very labile molecule under cold ISM conditions (Cody et al. 2011) and is considered a crucial chemical intermediary in the formation pathways leading to interstellar complex organic molecules (iCOMs) at low temperatures (Vasyunin & Herbst 2013; Barone et al. 2015).

Chemical reactions above 20 K and up to ~250 K are largely accepted to be governed by gas-phase chemistry in molecular processes (Eschenmoser 1994; Lazcano & Miller 1996). Formaldehyde gas-phase reactions are frequently linked to para-$H_2CO$ formation, while the chemistry in grain-iced mantles normally refers to the formation of its nuclear isomer, ortho-$H_2CO$ (Roueff et al. 2006; Ceccarelli et al. 2001). In this way, defining an ortho-to-para ratio (OTP) for $H_2CO$ can help to distinguish whether its formation has been produced in either the gas-phase or on icy-grain surfaces (Eschenmoser 1994; Guzmán et al. 2011, 2013). Below 20 K (the CO snow line), $H_2CO$ has been suggested to form on surfaces of icy interstellar dust grains by a double hydrogenation process of CO ($CO + \cdot H \rightarrow HCO + \cdot H \rightarrow H_2CO$, (Tielens & Whittet 1997; Woon 2002). After a migration of the dust to warmer regions, a sublimation process occurs desorbing formaldehyde from the grains and entering in the gas-phase. $H_2CO$ desorption energy has experimentally been defined to be 7.21 ± 0.21 kcal mol$^{-1}$ if grain sublayers are composed of iced water and to be 6.48 ± 0.12 kcal mol$^{-1}$ if grains are based on olivine. In both cases a zeroth-order kinetic velocity of $\omega_0 = 10^{28}$ mol cm$^{-2}$ s$^{-1}$ is obtained (Noble et al. 2012). In addition, CO hydrogenation seems to be 250 times more efficient in $H_2O$-rich ices than in CO-rich ice mantles, as estimated by Ceccarelli et al. (2001). This might justify why a portion of the $H_2CO$ abundances detected in some regions of ISM cannot be explained solely through gas-phase formation mechanisms with the abundances detected in excess typically attributed to dust grain formation (Hasegawa & Herbst 1993; Tielens & Whittet 1997; Woon 2002; Roueff et al. 2006; Persson et al. 2018). Despite the frequent $H_2CO$ detection, neither gas- nor grain-phase formations match the abundances that most modern astrochemical models predict. This is usually attributed to the fact that gas-phase reactions of formaldehyde and their associated molecular formation mechanisms in space are poorly understood (Dickens & Irvine 1999; Schöier et al. 2002; Ceccarelli et al. 2002; Roueff et al. 2006). The main aim of this paper therefore is quantum chemically to pinpoint viable molecular formation mechanisms of neutral $H_2CO$ in the gas-phase in cold regions of the ISM under local thermal equilibrium (LTE) conditions where this molecule has been detected.

## 2. Formaldehyde and cold astrophysical regions

Diffuse clouds (DC) can be described as irregular spatial confinements of interstellar gas and dust (silicate grains and amorphous crystals) at low temperatures and densities from 10 to a few 100 particles × cm$^{-3}$ (Ballesteros-Paredes et al. 1999; Ceccarelli et al. 2002; Yamamoto 2017; Velusamy et al. 2017). In this astrophysical environment, neutral atomic hydrogen ($H_I$) dominates showing a column density of $N_{HI} < 5 \times 10^{20}$ cm$^{-2}$ (Millar et al. 1979; Liszt & Lucas 1995). In addition to enabling observations in direct lines of sight (LOS) from terrestrial and space telescopes (Wooden et al. 2004), the low particle density facilitates UV radiation transmission (which is the main source of energy, with a minor contribution from cosmic rays, CR) to penetrate the cloud, subsequently warming it. As a result, the kinetic temperature ($T_k$) of the gases ranges between 30 and 100 K (Ballesteros-Paredes et al. 1999) from external to the innermost regions with fluctuations in pressure from ~6100 to 7700 K cm$^{-3}$ (Yamamoto 2017). Because of the abundance and related absorption produced by $H_I$, UV radiation does not exceed of 13.60 eV (313.62 kcal mol$^{-1}$) (Ballesteros-Paredes et al. 1999). Formaldehyde has been detected specifically in regions of this classification, along with other carbonaceous compounds, such as HCN, HCO, HNO, $C_2H$, and $C_3H$. The core of the cloud, known as a translucent cloud, is denser ($5 \times 10^4$ cm$^{-3}$) with a central dust visual extinction of ~2.5 magnitudes (van der Tak et al. 2000; Di Francesco et al. 2002). The dominant form of hydrogen in the core is neutral atomic with a column density ($N_{HI}$) associated with $1.7 \times 10^{21}$ cm$^{-2}$ mag$^{-1}$ × AV (Liszt & Lucas 1995). Molecular hydrogen ($H_2$) is formed in this region on dust grain surfaces reaching a fractional density ($N_{HI}/N_{H2}$) of $10^2$ cm$^{-3}$ at a temperature of ~100 K (Liszt & Lucas 1995). The average abundance density detected for atomic nitrogen has been estimated to be $4.3 \times 10^{-5}$ cm$^{-3}$ and for atomic oxygen this is ~$3.5 \times 10^{-7}$ cm$^{-3}$ (Yamamoto 2017), while $H_2CO$ shows a number density value of ~$10^{-10}$ cm$^{-3}$ (Millar et al. 1979; Liszt & Lucas 1995). In this way diffuse molecular clouds (DMCs) are prone to transforming interstellar atoms into molecules. As a case in point, formaldehyde forms at ~100 K under an average pressure of ~$6.9 \times 10^3$ K cm$^{-3}$.

Dark, cold, and dense molecular clouds (DCDMCs) are commonly associated with star-forming regions (Maciel 2013). The most common form of hydrogen is neutral molecular ($H_2$) with a typical particle spatial density of 10 cm$^{-3}$–10 cm$^{-6}$ cm$^{-3}$ (Spitzer 1998). The temperature inside these clouds is lower than in DMCs. It typically oscillates from 10 to 20 (Combes & Pineau des Forets 1999; Marmet 2000). The main source of energy is UV radiation (primary and secondary – UV pumping; Klessen & Glover 2014) generated by collisions between CRs and $H_2$ that cause the molecular bonds to break. The excess energy per collision has been defined empirically to be 4.48 eV or, equivalently, 103.44 kcal mol$^{-1}$ (Klessen & Glover 2014). A particular type of dark cloud, known as "Bok globules" (Bok & Reilly 1947), are small (0.2–1 pc; Launhardt et al. 2010), cold, and dense confinements of interstellar dust and gas in hydrostatic equilibrium at the edge of gravitational collapse where the prevailing hydrogen is also in the molecular form (Dickman 1977). Multiple molecular species have been detected inside Bok globules, such as formaldehyde ($H_2CO$; Palmer et al. 1969; Rickard et al. 1977; Minn & Greenberg 1979), carbon monoxide (CO; Wang et al. 1995; Cecchi-Pestellini et al. 2001), or carbon monosulfide (CS; Wang et al. 1995; Turner 1995), as well as isotopologs of these species such as $C^{18}O$ (Wang et al. 1995). Additionally, nitrogenated compounds as ammonia ($NH^3$; Minn & Greenberg 1979; Turner 1995; Bourke et al. 1995), and some ionized species such as $HCO^+$ (Turner 1995; Bourke et al. 1995), are also present in these astrophysical objects. The $H_2CO$ abundances relative to molecular hydrogen detected toward this type of clouds are a few orders of magnitude higher than DMCs. They notably differ in composition from cloud to cloud. Some example values are $4 \times 10^{-10}$ cm$^{-3}$ in B68 (Di Francesco et al. 2002) or $2 \times 10^{-8}$ cm$^{-3}$ in L134N and TMC-1 (Ohishi et al. 1992). Applying the Bonnor-Ebert sphere model (Ebert 1955;

Bonnor 1956) and using observational data from ten different Bok globules, Kandori et al. (2005) determined an effective temperature of $T_{\rm eff}$ = 13.2 K and an averaged confining pressure of $P_{\rm gas} = 5.3 \times 10^4$ K cm$^{-3}$. These two variables of the state equation are considered here alongside computational calculations of the formation mechanisms of $H_2CO$ for this kind of astrophysical scenario.

After the gravitational collapse and if the total mass of the individual cloud is approximately the mass of the Sun ($2 \times 10^{30}$ Kg; (van Dishoeck 2014), a new astrophysical system forms that is dominated gravitationally by a low-mass protostar known as a young stellar object (YSO). The protostar is in the center of the system and is surrounded by a Keplerian-rotating envelope of dust and gas, that is gravitationally connected and in which the angular momentum is conserved (Cassen & Moosman 1981). The distance to the star will define the surrounding energy, which is dominantly thermal and capable of heating the more distant dust grain mantles. The processes progressively inject chemical constituents into the gas-phase (Ceccarelli et al. 2001) and determine what types of physical-chemical processes govern in every region of the disk. Circumstellar envelopes of low-mass protostars (CELMP) are environments that are extraordinarily rich in organic molecules as $H_2CO$ or HNCO and in iCOMs such as $CH_3CN$, $CH_3CHO$, and $C_2H_5OH$ (Schöier et al. 2002), in addition to other O- and N-bearing complexes (JØrgensen et al. 2012). IRAS 16293-2422 (hereafter IRAS 16293) was chosen for this work as the quintessential example of such an object. IRAS 16293 is adequate for this role because formaldehyde has previously been detected with notable variations in abundances in three differentiated regions of its protodisk (Ceccarelli et al. 2001; JØrgensen et al. 2012; Jaber et al. 2014; van der Wiel et al. 2019). Additionally, glycolaldehyde ($C_2H_4O_2$), the simplest form of sugar and one of the first intermediates in the formose reaction (Larralde et al. 1995), has also been detected in this object for the first time in space in 2012 (JØrgensen et al. 2012). The more distant regions of the disk (>4000 AU) contain species such as CO, $H_2CO$, $CH_3OH$, or $H_2O$ (van Dishoeck et al. 1995) at low temperatures (10–20 K) where the gas is slightly warmer than the dust grains as they are tightly coupled to them. Energy from collisions among dust and gas is therefore considered to be the main heating mechanism in this region. Nevertheless, the thermal energy generated by those collisions is not enough to activate the formation of molecules with barriers at or below 20 K (0.0397 kcal mol$^{-1}$). The gas column density of molecular hydrogen has been estimated to be $N(H_2) = 1.3 \times 10^{23}$ cm$^{-2}$ (Ward-Thompson et al. 1999), with a fractional abundance of formaldehyde – $N(H_2CO)/N(H_2)$ – $\sim 4 \times 10^{-10}$ cm$^{-3}$ in the gas-phase (Ceccarelli et al. 2001). When the temperature rises above ~20 K, CO starts to desorb from the ice grains and enters the gas-phase with an increase of $\sim 10^3$ cm$^{-3}$ in detected densities with respect to $H_2$ (Cassen & Moosman 1981; Aikawa et al. 2015). Formaldehyde starts to deplete from frozen grains at around ~ 40 K and it is fully desorbed at ~60 K (Ceccarelli et al. 2001). The additional $H_2CO$ mixes with the existing circumstellar mass of gas, which may justify why at ~700 AU from the core and at gas temperatures between 80 and 100 K ~ 50 kcal mol$^{-1}$), the detected fractional abundances of formaldehyde reach $N(H_2CO)/N(H_2) = \sim 4.0 \times 10^{-9}$ cm$^{-3}$ (Ceccarelli et al. 2001). This implies an $H_2$ column density that is estimated to be $N(H_2) = \sim 5.0 \times 10^{21}$cm$^{-2}$ (Bottinelli et al. 2014). The inner part of the envelope at ~150 AU in a region with temperatures of 100–150 K has a higher density of formaldehyde with an $N(H_2CO)/N(H_2)$ of $\sim 10 \times 10^{-7}$ cm$^{-3}$, as well as an increase in fractional abundances for $H_2O$ (which desorbs from iced mantles at ~80 K) (Ceccarelli et al. 2001). This region also produces new molecules principally due to the thermal energy emitted from the YSO ( 99.99 kcal mol$^{-1}$). One example is trans-HONO. This chemical compound has recently been detected for first time in space and in this part of the disk (Coutens et al. 2019). Its proposed formation has inspired some reactions proposed in this work that may lead to $H_2CO$. In this region, a column density for molecular hydrogen is considered like that in region II ($N_{(H2)}$ = $\sim 5.0 \times 10^{21}$ cm$^{-2}$). The three regions of IRAS 16293 dictate the physical parameters for the presentation of our computations which are defined as follows:

- Region I/ $d$ ~ 4000 AU, $T_{\rm gas}$ = 20 K, $P_{\rm gas}$ = $2.29 \times 10^7$ K cm$^{-3}$;
- Region II/ $d$~ 700 AU, $T_{\rm gas}$ = 80 K, $P_{\rm gas}$ = $7.06 \times 10^7$ K cm$^{-3}$;
- Region III/ $d$~150 AU, $T_{\rm gas}$ = 150 K, $P_{\rm gas}$ = $6.08 \times 10^8$ K cm$^{-3}$.

## 3. Method and computational details

Ninety-six known molecular reaction mechanisms that lead to ground electronic state $H_2CO$ in the gas-phase, in turn composed of smaller chemical species that are reported in the literature (NIST; Linstrom & Mallard 1997) or are defined as in Table 1 were considered as the starting point of our computational calculations. The possible selected reaction mechanisms themselves are composed of chemical species that have already been detected in the ISM (McGuire 2018), except for the likely $H_2^+$, $CH_2^+$, $CH_3$+, cis-HONO and $NO_2$ species. The molecular energy (atomic when required) of chemical species, reactants, and products is computed using quantum chemical computational methods at two different levels of theory and basis set. Explicitly correlated, coupled-cluster theory at the single and double level, with perturbative triple corrections (CCSD(T)-F12; Adler et al. 2007; Knizia et al. 2009) and second-order MØller–Plesset perturbation theory (MP2; Möller & Plesset 1934) were selected. The basis set for CCSD(T)-F12 is the explicitly correlated correlation-consistent triple-zeta basis set (Dunning 1989; Peterson et al. 2008; Hill & Peterson 2010), or abbreviated cc-pVTZ-F12. This combination provides a similar accuracy as but a computation two orders of magnitude faster than CCSD(T)/aug-pV5Z (Knizia et al. 2009). On the other hand, MP2 (Möller & Plesset 1934), with a double-zeta basis set (aug-cc-pVDZ) was selected because it offers a suitable compromise between accuracy and computational cost (Kaminsky et al. 2008).

The Molpro quantum chemistry package, version 2020.01 (Patch Level 3; Werner et al. 2020) was employed for CCSD(T)-F12/cc-pVTZ-F12 computations, while Gaussian 16, Revision B.01 (Frisch et al. 2016) was used for the MP2/aug-cc-pVDZ computations. Restricted references for closed-shell molecules were used, while restricted open-shell references were employed for species with non-spin-paired electrons. To proceed with initial computations, for every chemical compound, spare reactants, and (spare) products, the spin multiplicity (SpM) belonging to every spatial electronic wave function and net charge must be defined (Hund 1925, 1927). For the thermodynamic function, calculations at different temperature and pressure profiles and the Maxwell-Boltzmann (Muncaster 1979, and ref. therein; Rowlinson 2005) through related partition functions from statistical quantum mechanics theory were applied. This was used to determine reactions as exothermic ($\Delta H^\circ < 0$) and exergonic ($\Delta G^\circ < 0$) in the three astrophysical scenarios we studied. The

**Table 1.** Chemical reactions of formaldehyde ($H_2CO$) proposed in this research.

| R/id | Reaction mechanism | R/id | Reaction mechanism | R/id | Reaction mechanism | R/id | Reaction mechanism | R/id | Reaction mechanism | R/id | Reaction mechanism |
|---|---|---|---|---|---|---|---|---|---|---|---|
| R1 | $\cdot C + {}^1H_2O \rightarrow {}^1H_2CO$ | R17 | $\cdot CH + {}^{\cdot 2}OH \rightarrow {}^1H_2CO$ | R33 | ${}^{\cdot 3}CH_2 + {}^{\cdot 2}OH \rightarrow {}^1H_2CO + \cdot H$ | R49 | $\cdot CH_3 + {}^{\cdot 2}OH \rightarrow {}^1H_2CO + {}^{\cdot 3}H_2$ | R65 | $C^+H_3 + {}^1O_2 \rightarrow {}^1H_2CO + \cdot OH^+$ | R81 | $\cdot CHO + trans\text{-}HONO \rightarrow {}^1H_2CO + \cdot NO_2$ |
| R2 | ${}^1CO + {}^1H_2 \rightarrow {}^1H_2CO$ | R18 | $\cdot CH + {}^{\cdot 4}OH \rightarrow {}^1H_2CO$ | R34 | ${}^{\cdot 2}C^+ H_2 + {}^1O_2 \rightarrow {}^1H_2CO + \cdot O^+$ | R50 | $\cdot CH_3 + {}^{\cdot 3}O_2 \rightarrow {}^1H_2CO + {}^{\cdot 4}OH$ | R66 | $C^+H_3 + {}^1O_2 \rightarrow {}^1H_2CO + \cdot O^+H$ | R82 | $\cdot CHO + \cdot CHO \rightarrow {}^1H_2CO + {}^1CO$ |
| R3 | ${}^{\cdot 3}CO + {}^{\cdot 3}H_2 \rightarrow {}^1H_2CO$ | R19 | $\cdot CH + {}^1H_2O \rightarrow {}^1H_2CO + \cdot H$ | R35 | ${}^{\cdot 2}C^+H_2 + {}^{\cdot 3}O_2 \rightarrow {}^1H_2CO + \cdot O^+$ | R51 | $\cdot CH_3 + {}^{\cdot 3}O_2 \rightarrow {}^1H_2CO + {}^{\cdot 2}OH$ | R67 | $CH_3^+ + {}^{\cdot 4}OH \rightarrow {}^1H_2CO + \cdot H_2^+$ | R83 | $\cdot CHO + \cdot CHO \rightarrow {}^1H_2CO + {}^{\cdot 3}CO$ |
| R4 | ${}^{\cdot 3}CO + {}^1H_2 \rightarrow {}^1H_2CO$ | R20 | ${}^1CH_2 + O({}^1D) \rightarrow {}^1H_2CO$ | R36 | ${}^{\cdot 4}CH_2{}^+ + {}^1O_2 \rightarrow {}^1H_2CO + \cdot O^+$ | R52 | $\cdot CH_3 + {}^1O_2 \rightarrow {}^1H_2CO + {}^{\cdot 4}OH$ | R68 | $CH_3^+ + {}^{\cdot 2}OH \rightarrow {}^1H_2CO + \cdot H_2^+$ | R84 | $\cdot CHO + HNO \rightarrow {}^1H_2CO + \cdot NO$ |
| R5 | ${}^1CO + {}^{\cdot 3}H_2 \rightarrow {}^1H_2CO$ | R21 | ${}^1CH_2 + \cdot O({}^3P) \rightarrow {}^1H_2CO$ | R37 | ${}^{\cdot 4}CH_2 + + {}^{\cdot 3}O_2 \rightarrow {}^1H_2CO + \cdot O^+$ | R53 | $\cdot CH_3 + {}^1O_2 \rightarrow {}^1H_2CO + {}^{\cdot 2}OH$ | R69 | $C^+H_3 + {}^{\cdot 4}OH \rightarrow {}^1H_2CO + \cdot H_2+$ | R85 | $\cdot CHO + HCN \rightarrow {}^1H_2CO + \cdot CN$ |
| R6 | ${}^1CO + {}^1H_2O \rightarrow {}^1H_2CO + O({}^1D)$ | R22 | ${}^{\cdot 3}CH_2 + O({}^1D) \rightarrow {}^1H_2CO$ | R38 | ${}^{\cdot 2}C^+H_2 + CO_2 \rightarrow {}^1H_2CO + \cdot CO^+$ | R54 | $\cdot CH_3 + \cdot NO_2 \rightarrow {}^1H_2CO + HNO$ | R70 | $C^+H_3 + {}^{\cdot 2}OH \rightarrow {}^1H_2CO + \cdot H_2^+$ | R86 | $\cdot CHO + CH_4 \rightarrow {}^1H_2CO + \cdot CH_3$ |
| R7 | ${}^{\cdot 3}CO + {}^1H_2O \rightarrow {}^1H_2CO + O({}^1D)$ | R23 | ${}^{\cdot 3}CH_2 + \cdot O({}^3P) \rightarrow {}^1H_2CO$ | R39 | ${}^{\cdot 2}C^+H_2 + CO_2 \rightarrow {}^1H_2CO + \cdot C^+O$ | R55 | $C^+H_3 + O({}^1D) \rightarrow {}^1H_2CO + \cdot H^+$ | R71 | $\cdot CHO + \cdot H \rightarrow {}^1H_2CO$ | R87 | $HCN + {}^1H_2O \rightarrow {}^1H_2CO + {}^1NH$ |
| R8 | ${}^1CO + {}^1H_2O \rightarrow {}^1H_2CO + \cdot O({}^3P)$ | R24 | ${}^1CH_2 + {}^1O_2 \rightarrow {}^1H_2CO + O({}^1D)$ | R40 | ${}^{\cdot 4}CH_2{}^+ + CO_2 \rightarrow {}^1H_2CO + \cdot CO^+$ | R56 | $C^+H_3 + \cdot O({}^3P) \rightarrow {}^1H_2CO + \cdot H^+$ | R72 | $\cdot CHO + {}^{\cdot 2}OH \rightarrow {}^1H_2CO + \cdot O({}^3P)$ | R88 | $HCN + {}^1H_2O \rightarrow {}^1H_2CO + {}^{\cdot 3}NH$ |
| R9 | ${}^{\cdot 3}CO + {}^1H_2O \rightarrow {}^1H_2CO + \cdot O({}^3P)$ | R25 | ${}^1CH_2 + {}^1O_2 \rightarrow {}^1H_2CO + \cdot O({}^3P)$ | R41 | ${}^{\cdot 4}CH_2{}^+ + CO_2 \rightarrow {}^1H_2CO + \cdot C^+O$ | R57 | $CH_3 + + O({}^1D) \rightarrow {}^1H_2CO + \cdot H^+$ | R73 | $\cdot CHO + {}^{\cdot 4}OH \rightarrow {}^1H_2CO + \cdot O({}^3P)$ | R89 | $CH_4 + O({}^1D) \rightarrow {}^1H_2CO + 2\cdot H$ |
| R10 | ${}^1CO + NH_3 \rightarrow {}^1H_2CO + {}^1NH$ | R26 | ${}^1CH_2 + {}^{\cdot 3}O_2 \rightarrow {}^1H_2CO + O({}^1D)$ | R42 | ${}^{\cdot 2}C + H_2 + {}^{\cdot 2}OH \rightarrow {}^1H_2CO + H^+$ | R58 | $CH_3{}^+ + \cdot O({}^3P) \rightarrow {}^1H_2CO + \cdot H^+$ | R74 | $\cdot CHO + {}^{\cdot 2}OH \rightarrow {}^1H_2CO + O({}^1D)$ | R90 | $CH_4 + \cdot O({}^3P) \rightarrow {}^1H_2CO + 2\cdot H$ |
| R11 | ${}^1CO + NH_3 \rightarrow {}^1H_2CO + {}^{\cdot 3}NH$ | R27 | ${}^1CH_2 + {}^{\cdot 3}O_2 \rightarrow {}^1H_2CO + \cdot O({}^3P)$ | R43 | ${}^{\cdot 2}C^+H_2 + {}^{\cdot 4}OH \rightarrow {}^1H_2CO + H^+$ | R59 | $CH_3{}^+ + {}^{\cdot 3}O_2 \rightarrow {}^1H_2CO + \cdot OH^+$ | R75 | $\cdot CHO + {}^{\cdot 4}OH \rightarrow {}^1H_2CO + O({}^1D)$ | R91 | $CH_4 + O({}^1D) \rightarrow {}^1H_2CO + {}^1H_2$ |
| R12 | ${}^{\cdot 3}CO + NH_3 \rightarrow {}^1H_2CO + {}^{\cdot 3}NH$ | R28 | ${}^3CH_2 + {}^3O_2 \rightarrow {}^1H_2CO + \cdot O({}^3P)$ | R44 | $\cdot CH_3 + O({}^1D) \rightarrow {}^1H_2CO + \cdot H$ | R60 | $CH_3{}^+ + {}^{\cdot 3}O_2 \rightarrow {}^1H_2CO + \cdot O^+H$ | R76 | $\cdot CHO + {}^1H_2O \rightarrow {}^1H_2CO + {}^{\cdot 4}OH$ | R92 | $CH_4 + \cdot O({}^3P) \rightarrow {}^1H_2CO + {}^1H_2$ |
| R13 | ${}^{\cdot 3}CO + NH_3 \rightarrow {}^1H_2CO + {}^1NH$ | R29 | ${}^1CH_2 + {}^{\cdot 4}OH \rightarrow {}^1H_2CO + \cdot H$ | R45 | $\cdot CH_3 + \cdot O({}^3P) \rightarrow {}^1H_2CO + \cdot H$ | R61 | $CH_3{}^+ + {}^1O_2 \rightarrow {}^1H_2CO + \cdot OH^+$ | R77 | $\cdot CHO + {}^1H_2O \rightarrow {}^1H_2CO + {}^{\cdot 2}OH$ | R93 | $CH_4 + O({}^1D) \rightarrow {}^1H_2CO + {}^{\cdot 3}H_2$ |
| R14 | $CO_2 + H_2O \rightarrow {}^1H_2CO + {}^{\cdot 3}O_2$ | R30 | ${}^1CH_2 + {}^{\cdot 2}OH \rightarrow {}^1H_2CO + \cdot H$ | R46 | $\cdot CH_3 + {}^{\cdot 4}OH \rightarrow {}^1H_2CO + {}^1H_2$ | R62 | $CH_3{}^+ + {}^1O_2 \rightarrow {}^1H_2CO + \cdot O^+H$ | R78 | $\cdot CHO + H_2O_2 \rightarrow {}^1H_2CO + \cdot H + {}^1O_2$ | R94 | $CH_4 + \cdot O({}^3P) \rightarrow {}^1H_2CO + {}^{\cdot 3}H_2$ |
| R15 | $CO_2 + H_2O \rightarrow {}^1H_2CO + {}^1O_2$ | R31 | ${}^1CH_2 + CO_2 \rightarrow {}^1H_2CO + {}^1CO$ | R47 | $\cdot CH_3 + {}^{\cdot 4}OH \rightarrow {}^1H_2CO + {}^{\cdot 3}H_2$ | R63 | $C^+H_3 + {}^{\cdot 3}O_2 \rightarrow {}^1H_2CO + \cdot OH^+$ | R79 | $\cdot CHO + H_2O_2 \rightarrow {}^1H_2CO + \cdot H + {}^{\cdot 3}O_2$ | R95 | $C_2H_4 + O({}^1D) \rightarrow {}^1H_2CO + {}^{\cdot 1}CH_2$ |
| R16 | $CO_2 + NH_3 \rightarrow {}^1H_2CO + HNO$ | R32 | ${}^1CH_2 + CO_2 \rightarrow {}^1H_2CO + {}^{\cdot 3}CO$ | R48 | $\cdot CH_3 + {}^{\cdot 2}OH \rightarrow {}^1H_2CO + {}^1H_2$ | R64 | $C^+H_3 + {}^{\cdot 3}O_2 \rightarrow {}^1H_2CO + \cdot O^+H$ | R80 | $\cdot CHO + cis\text{-}HONO \rightarrow {}^1H_2CO + \cdot NO_2$ | R96 | $C_2H_4 + \cdot O({}^3P) \rightarrow {}^1H_2CO + {}^{\cdot 1}CH_2$ |

**Notes.** This table presents the 96 initial reactions subject to investigation to produce neutral formaldehyde in cold astrophysical regions. Source: NIST; Linstrom & Mallard (1997) and own elaboration. R/id = reaction number.

reaction and thermodynamic energies contained in this research are corrected for the corresponding zeropoint energy (ZPE) and vibrational frequencies from the harmonic approximation.

Known favorable reactions involving reactants and their relative abundances for each scenario were incorporated into a detailed search on the energetically easiest path to pass from reactants to products on their potential energy surface (PES) and possible transition states (TS). There is no unique or unified method to find TS structures with success, and to avoid intuition as much as possible, we used two different scientific approaches. The first approach consists of obtaining the TS with the PM7 semi-empirical quantum mechanical method (SQM; Stewart 2013), confirmed by an intrinsic reaction coordinate (IRC) process (Fukui 1981; Zhixing 1989). For this purpose, the automated reaction mechanisms and kinetics program (AutoMeKin) (Martínez-Núñez 2015a,b; MOPAC2016 2016; Rodríguez et al. 2018) was employed. Before going to high-level calculations, every suggested trajectory was analyzed in detail to determine whether it produces a physically meaningful pathway on the grid of the reaction PES. After a TS structure was confirmed at SQM, geometries and energies were reoptimized via DFT (Hohenberg & Kohn 1964; Kohn & Sham 1965) with the global hybrid B3LYP method (Becke 1988) and the aug-cc-pVTZ basis set before we proceeded with the application of the higher-level calculations. Additionally, a direct TS search in Gaussian 16 (Frisch et al. 2016) by applying the synchronous transit-guided quasi-Newton method (STQN; Schlegel 1982) using B3LYP/aug-cc-pVTZ was executed. After a definitive TS structure given was obtained and confirmed by IRC (Fukui 1981; Zhixing 1989) through B3LYP/aug-cc-pVTZ, single-point energy (SPE) calculations on that specific saddle point of the PES were computed at the CCSD(T)-F12/cc-pVTZ-F12 and MP2/aug-cc-pVDZ levels of theory and basis sets. On the other hand, some reactions that are able to proceed are composed of excited electronic state reagents; their abundances are discussed in a different section. As result, three types of reactions were obtained composed of reactants that were previously detected in the astronomical objects under study. These include (i) barrier-less reactions, (ii) reactions with outer transition states, and (iii) reactions with inner transitions states. With respect to (i) barrier-less reactions, it must be emphasized that they rely upon radiative association (RA) processes, a feature that will significantly slow their kinetic progression down without the presence of catalysts. (ii) Reactions with outer transition states that are composed of a "real" energy barrier(s) where the transition state energy is entirely or partially above than that of the separated reactants. This feature notably penalize the formation of the products in cold conditions of space. In contrast, reactions (iii) with an inner transition state(s), in which the energy is totally submerged along the reaction path below the asymptotic reactant's energy, are the most likely reactions to proceed. We subsequently focus the discussions and conclusions on them. As computations consider gas-phase structures at LTE, the effect of a third physical phenomenon beyond temperature and pressure (e.g., the state of ionization of the medium, the presence of magnetic fields, hyper-gas turbulence, the morphological or chemical composition thereof, effects of gravity, existence of catalyst agents during reactions, or the quantum tunneling effect) are considered beyond the scope this research.

## 4. Results and discussions

Ninety-six molecular reaction mechanisms have been proposed at various points in history to form formaldehyde in the gas-phase (Table 1). These reactions in turn are composed of 45 different chemical species, including excited electronic states. Initial computations return the thermodynamic function values for each reaction mechanism at $T$ = 298.15 K and $P$ = 1 atm, for the two levels of theory and basis set, presented in Table 2 as an initial reference. Under the cold conditions of the ISM the most favorable reactions are those that are exothermic and exergonic. After applying TS searching methods on the reactions presented in Table 2, (R18) $\cdot CH + {}^{\cdot 4}OH \rightarrow {}^1H_2CO$, (R23) ${}^{\cdot 3}CH_2 + \cdot O({}^3P) \rightarrow {}^1H_2CO$ and (R75) $\cdot CHO + {}^4OH \rightarrow {}^1H_2CO + O({}^1D)$ are found not to converge in the computed pathway to the desired products, and therefore removed from the reactions we consider.

### 4.1. Diffuse molecular clouds

In DMCs where $T_{gas}$ = 100 K and $P_{gas}$ = 6.9 × $10^3$ K $cm^{-3}$ for this study, 56 reactions from the preliminary reaction list presented in Table 1 at the CCSD(T)-F12/cc-pVTZ-F12 level of theory and basis set return favorable thermodynamics. Again, the nonviable R18, R23, and R75 reactions and then undetected ionized species were removed from consideration. R1 ($C_I + H_2O \rightarrow {}^1H_2CO$) cannot be considered either because

**Table 2.** Thermodynamic function values of initial reactions (Table 1).

| R/id | Reaction mechanism | $\Delta H°$ | $\Delta S°$ | $\Delta G°$ | $\Delta H°$ | $\Delta S°$ | $\Delta G°$ |
|---|---|---|---|---|---|---|---|
| R1 | $\cdot C + {}^1H_2O \rightarrow {}^1H_2CO$ | −138.60 | −28.42 | −130.13 | −133.93 | −28.40 | −125.46 |
| R2 | $^1CO + {}^1H_2 \rightarrow {}^1H_2CO$ | 0.68 | −26.11 | 8.46 | 0.85 | −26.17 | 8.65 |
| R3 | $^3CO + {}^3H_2 \rightarrow {}^1H_2CO$ | −329.80 | −31.70 | −320.35 | −328.16 | −31.52 | −318.76 |
| R4 | $^3CO + {}^1H_2 \rightarrow {}^1H_2CO$ | −137.97 | −28.55 | −129.45 | −144.76 | −28.45 | −136.27 |
| R5 | $^1CO + {}^3H_2 \rightarrow {}^1H_2CO$ | −191.16 | −29.25 | −182.44 | −182.55 | −29.24 | −173.83 |
| R6 | $^1CO + {}^1H_2O \rightarrow {}^1H_2CO + O(^1D)$ | 166.89 | −5.79 | 168.62 | 187.04 | −5.84 | 188.78 |
| R7 | $^3CO + {}^1H_2O \rightarrow {}^1H_2CO + O(^1D)$ | 28.25 | −8.24 | 30.70 | 41.43 | −8.12 | 43.85 |
| R8 | $^1CO + {}^1H_2O \rightarrow {}^1H_2CO + \cdot O(^3P)$ | 117.10 | −3.61 | 118.18 | 119.10 | −3.66 | 120.19 |
| R9 | $^3CO + {}^1H_2O \rightarrow {}^1H_2CO + \cdot O(^3P)$ | −21.55 | −6.06 | −19.74 | −26.50 | −5.93 | −24.73 |
| R10 | $^1CO + NH_3 \rightarrow {}^1H_2CO + {}^1NH$ | 138.74 | −2.07 | 139.36 | 151.91 | −2.08 | 152.53 |
| R11 | $^1CO + NH_3 \rightarrow {}^1H_2CO + {}^3NH$ | 96.26 | 0.14 | 96.22 | 96.43 | 0.10 | 96.40 |
| R12 | $^3CO + NH_3 \rightarrow {}^1H_2CO + \cdot {}^3NH$ | −42.38 | −2.30 | −41.70 | −49.18 | −2.18 | −48.53 |
| R13 | $^3CO + NH_3 \rightarrow {}^1H_2CO + {}^1NH$ | 0.09 | −4.52 | 1.44 | 6.30 | −4.36 | 7.60 |
| R14 | $CO_2 + H_2O \rightarrow {}^1H_2CO + {}^3O_2$ | 125.10 | 4.10 | 123.87 | 128.02 | 4.11 | 126.79 |
| R15 | $CO_2 + H_2O \rightarrow {}^1H_2CO + {}^1O_2$ | 154.23 | 1.96 | 153.64 | 158.36 | 2.03 | 157.75 |
| R16 | $CO_2 + NH_3 \rightarrow {}^1H_2CO + HNO$ | 103.85 | 4.78 | 102.42 | 107.61 | 4.78 | 106.18 |
| R17 | $\cdot CH + {}^2OH \rightarrow {}^1H_2CO$ | −176.42 | −64.02 | −157.33 | −179.62 | −64.00 | −160.54 |
| R18 | $\cdot CH + {}^4OH \rightarrow {}^1H_2CO$ | −278.10 | −74.51 | −255.89 | −274.73 | −75.86 | −252.11 |
| R19 | $\cdot CH + {}^1H_2O \rightarrow {}^1H_2CO + \cdot H$ | −58.16 | −39.14 | −46.49 | −63.44 | −39.15 | −51.77 |
| R20 | $^1CH_2 + O(^1D) \rightarrow {}^1H_2CO$ | −236.91 | −28.57 | −228.39 | −259.01 | −28.56 | −250.50 |
| R21 | $^1CH_2 + \cdot O(^3P) \rightarrow {}^1H_2CO$ | −187.12 | −30.75 | −177.95 | −191.08 | −30.74 | −181.91 |
| R22 | $^3CH_2 + O(^1D) \rightarrow {}^1H_2CO$ | −228.05 | −30.06 | −219.09 | −243.57 | −30.07 | −234.60 |
| R23 | $^3CH_2 + \cdot O(^3P) \rightarrow {}^1H_2CO$ | −178.26 | −32.24 | −168.64 | −175.64 | −32.26 | −166.02 |
| R24 | $^1CH_2 + {}^1O_2 \rightarrow {}^1H_2CO + O(^1D)$ | −48.42 | −6.90 | −46.36 | −34.89 | −7.05 | −32.79 |
| R25 | $^1CH_2 + {}^1O_2 \rightarrow {}^1H_2CO + \cdot O(^3P)$ | −98.21 | −4.72 | −96.80 | −102.83 | −4.87 | −101.38 |
| R26 | $^1CH_2 + {}^3O_2 \rightarrow {}^1H_2CO + O(^1D)$ | −19.29 | −9.04 | −16.59 | −4.55 | −9.13 | −1.83 |
| R27 | $^1CH_2 + {}^3O_2 \rightarrow {}^1H_2CO + \cdot O(^3P)$ | −69.08 | −6.86 | −67.03 | −72.49 | −6.94 | −70.42 |
| R28 | $^3CH_2 + {}^3O_2 \rightarrow {}^1H_2CO + \cdot O(^3P)$ | −60.22 | −8.36 | −57.73 | −57.05 | −8.46 | −54.52 |
| R29 | $^1CH_2 + {}^4OH \rightarrow {}^1H_2CO + \cdot H$ | −186.76 | −19.97 | −180.81 | −190.74 | −21.35 | −184.37 |
| R30 | $^1CH_2 + {}^2OH \rightarrow {}^1H_2CO + \cdot H$ | −85.08 | −9.48 | −82.25 | −95.64 | −9.49 | −92.81 |
| R31 | $^1CH_2 + CO_2 \rightarrow {}^1H_2CO + {}^1CO$ | −61.08 | 0.85 | −61.34 | −63.57 | 0.82 | −63.82 |
| R32 | $^1CH_2 + CO_2 \rightarrow {}^1H_2CO + {}^3CO$ | 77.56 | 3.30 | 76.58 | 82.03 | 3.10 | 81.11 |
| R33 | $^3CH_2 + {}^2OH \rightarrow {}^1H_2CO + \cdot H$ | −76.22 | −10.98 | −72.95 | −80.20 | −11.01 | −76.91 |
| R34 | $^2C^+ H_2 + {}^1O_2 \rightarrow {}^1H_2CO + \cdot O^+$ | 66.84 | −6.10 | 68.66 | 86.24 | −6.26 | 88.11 |
| R35 | $^2C^+H_2 + {}^3O_2 \rightarrow {}^1H_2CO + \cdot O^+$ | 95.97 | −8.24 | 98.43 | 116.58 | −8.34 | 119.07 |
| R36 | $^4CH_2^+ + {}^1O_2 \rightarrow {}^1H_2CO + \cdot O^+$ | −17.86 | −8.74 | −15.25 | 7.29 | −8.82 | 9.92 |
| R37 | $^4CH_2^+ + {}^3O_2 \rightarrow {}^1H_2CO + \cdot O^+$ | 11.27 | −10.88 | 14.52 | 37.63 | −10.90 | 40.88 |
| R38 | $^2C^+H_2 + CO_2 \rightarrow {}^1H_2CO + \cdot CO^+$ | 171.85 | 3.65 | 170.77 | 197.01 | 3.61 | 195.93 |
| R39 | $^2C^+H_2 + CO_2 \rightarrow {}^1H_2CO + \cdot C^+O$ | 32.05 | 1.61 | 31.57 | 42.80 | 1.43 | 42.37 |
| R40 | $^4CH_2^+ + CO_2 \rightarrow {}^1H_2CO + \cdot CO^+$ | 87.15 | 1.01 | 86.85 | 118.06 | 1.06 | 117.74 |
| R41 | $^4CH_2^+ + CO_2 \rightarrow {}^1H_2CO + \cdot C^+O$ | −52.65 | −1.03 | −52.34 | −36.15 | −1.13 | −35.81 |
| R42 | $^2C+H_2 + {}^2OH \rightarrow {}^1H_2CO + H^+$ | −85.77 | −14.08 | −81.58 | −81.30 | −14.02 | −77.12 |
| R43 | $^2C^+H_2 + {}^4OH \rightarrow {}^1H_2CO + H^+$ | −102.76 | −21.93 | −96.22 | −97.46 | −23.32 | −90.51 |
| R44 | $\cdot CH_3 + O(^1D) \rightarrow {}^1H_2CO + \cdot H$ | −117.92 | −2.52 | −117.17 | −141.11 | −2.54 | −140.35 |
| R45 | $\cdot CH_3 + \cdot O(^3P) \rightarrow {}^1H_2CO + \cdot H$ | −68.13 | −4.71 | −66.73 | −73.18 | −4.73 | −71.77 |
| R46 | $\cdot CH_3 + {}^4OH \rightarrow {}^1H_2CO + {}^1H_2$ | −171.66 | −17.59 | 166.41 | −166.21 | −18.92 | −160.57 |
| R47 | $\cdot CH_3 + {}^4OH \rightarrow {}^1H_2CO + {}^3H_2$ | 20.18 | −14.44 | 24.48 | 17.19 | −15.85 | 21.92 |
| R48 | $\cdot CH_3 + {}^2OH \rightarrow {}^1H_2CO + {}^1H_2$ | −69.97 | −7.10 | −67.86 | −71.11 | −7.06 | −69.00 |
| R49 | $\cdot CH_3 + {}^2OH \rightarrow {}^1H_2CO + {}^3H_2$ | 121.86 | −3.95 | 123.04 | 112.29 | −3.99 | 113.48 |
| R50 | $\cdot CH_3 + {}^3O_2 \rightarrow {}^1H_2CO + \cdot {}^4OH$ | 49.55 | 8.40 | 47.05 | 45.07 | 9.68 | 42.1 |
| R51 | $\cdot CH_3 + {}^3O_2 \rightarrow {}^1H_2CO + \cdot {}^2OH$ | −52.13 | −2.09 | −51.51 | −50.03 | −2.18 | −49.38 |
| R52 | $\cdot CH_3 + {}^1O_2 \rightarrow {}^1H_2CO + \cdot {}^4OH$ | 20.42 | 10.55 | 17.27 | 14.74 | 11.76 | 11.23 |
| R53 | $\cdot CH_3 + {}^1O_2 \rightarrow {}^1H_2CO + \cdot {}^2OH$ | −81.26 | 0.06 | −81.28 | −80.37 | −0.10 | −80.34 |
| R54 | $\cdot CH_3 + \cdot NO_2 \rightarrow {}^1H_2CO + HNO$ | −51.00 | −1.92 | −50.43 | −41.41 | −1.65 | −40.92 |
| R55 | $C^+H_3 + O(^1D) \rightarrow {}^1H_2CO + \cdot H^+$ | −30.37 | −1.97 | −29.79 | −50.31 | −1.94 | −49.73 |
| R56 | $C^+H_3 + \cdot O(^3P) \rightarrow {}^1H_2CO + \cdot H^+$ | 19.42 | −4.15 | 20.65 | 17.63 | −4.13 | 18.86 |
| R57 | $CH_3+ + O(^1D) \rightarrow {}^1H_2CO + \cdot H^+$ | −121.74 | −6.66 | −119.75 | −135.45 | −6.60 | −133.48 |
| R58 | $CH_3^+ + \cdot O(^3P) \rightarrow {}^1H_2CO + \cdot H^+$ | −71.95 | −8.84 | −69.31 | −67.51 | −8.78 | −64.90 |
| R59 | $CH_3^+ + {}^3O_2 \rightarrow {}^1H_2CO + \cdot OH^+$ | −70.48 | −3.81 | −69.34 | −64.41 | −3.84 | −63.26 |
| R60 | $CH_3^+ + {}^3O_2 \rightarrow {}^1H_2CO + \cdot O^+H$ | −13.52 | −6.00 | −11.73 | 10.44 | −6.01 | 12.23 |
| R61 | $CH_3^+ + {}^1O_2 \rightarrow {}^1H_2CO + \cdot OH^+$ | −99.61 | −1.67 | −99.11 | −94.74 | −1.76 | −94.22 |
| R62 | $CH_3^+ + {}^1O_2 \rightarrow {}^1H_2CO + \cdot O^+H$ | −42.65 | −3.86 | −41.50 | −19.90 | −3.93 | −18.73 |
| R63 | $C^+H_3 + {}^3O_2 \rightarrow {}^1H_2CO + \cdot OH^+$ | 20.89 | 0.89 | 20.62 | 20.73 | 0.81 | 20.49 |
| R64 | $C^+H_3 + {}^3O_2 \rightarrow {}^1H_2CO + \cdot O^+H$ | 77.85 | −1.30 | 78.23 | 95.58 | −1.36 | 95.98 |
| R65 | $C^+H_3 + {}^1O_2 \rightarrow {}^1H_2CO + \cdot OH^+$ | −8.25 | 3.03 | −9.15 | −9.60 | 2.89 | −10.47 |
| R66 | $C^+H_3 + {}^1O_2 \rightarrow {}^1H_2CO + \cdot O^+H$ | 48.71 | 0.84 | 48.46 | 65.24 | 0.72 | 65.02 |
| R67 | $CH_3^+ + {}^4OH \rightarrow {}^1H_2CO + \cdot H_2^+$ | −133.55 | −17.56 | −128.31 | −128.60 | −18.87 | −122.97 |
| R68 | $CH_3^+ + {}^2OH \rightarrow {}^1H_2CO + \cdot H_2^+$ | −31.87 | −7.07 | −29.76 | −33.50 | −7.01 | −31.41 |
| R69 | $C^+H_3 + {}^4OH \rightarrow {}^1H_2CO + \cdot H_2^+$ | −42.19 | −12.86 | −38.35 | −43.46 | −14.22 | −39.22 |
| R70 | $C^+H_3 + {}^2OH \rightarrow {}^1H_2CO + \cdot H_2^+$ | 59.50 | −2.37 | 60.20 | 51.64 | −2.36 | 52.35 |
| R71 | $\cdot CHO + \cdot H \rightarrow {}^1H_2CO$ | −87.90 | −28.74 | −79.33 | −82.33 | −28.76 | −73.75 |
| R72 | $\cdot CHO + {}^2OH \rightarrow {}^1H_2CO + \cdot O(^3P)$ | 14.14 | −7.48 | 16.37 | 13.11 | −7.51 | 15.35 |
| R73 | $\cdot CHO + {}^4OH \rightarrow {}^1H_2CO + \cdot O(^3P)$ | −87.54 | −17.97 | −82.19 | −81.99 | −19.37 | −76.21 |
| R74 | $\cdot CHO + {}^2OH \rightarrow {}^1H_2CO + O(^1D)$ | 63.93 | −9.66 | 66.81 | 81.05 | −9.69 | 83.94 |
| R75 | $\cdot CHO + {}^4OH \rightarrow {}^1H_2CO + O(^1D)$ | −37.75 | −20.15 | −31.74 | −14.05 | −21.55 | −7.63 |
| R76 | $\cdot CHO + {}^1H_2O \rightarrow {}^1H_2CO + {}^4OH$ | 132.05 | 6.63 | 130.07 | 128.96 | 7.95 | 126.59 |
| R77 | $\cdot CHO + {}^1H_2O \rightarrow {}^1H_2CO + {}^2OH$ | 30.37 | −3.86 | 31.52 | 33.86 | −3.91 | 35.02 |
| R78 | $\cdot CHO + H_2O_2 \rightarrow {}^1H_2CO + \cdot H + {}^1O_2$ | 76.89 | 18.55 | 71.36 | 70.65 | 18.66 | 65.08 |
| R79 | $\cdot CHO + H_2O_2 \rightarrow {}^1H_2CO + \cdot H + {}^3O_2$ | 47.76 | 20.69 | 41.59 | 40.31 | 20.74 | 34.13 |
| R80 | $\cdot CHO + cis{-}HONO \rightarrow {}^1H_2CO + \cdot NO_2$ | −2.39 | −1.44 | −1.96 | −11.48 | −1.80 | −10.94 |
| R81 | $\cdot CHO + trans{-}HONO \rightarrow {}^1H_2CO + \cdot NO_2$ | −2.07 | −1.65 | −1.58 | −10.93 | −2.09 | −10.31 |
| R82 | $\cdot CHO + \cdot CHO \rightarrow {}^1H_2CO + {}^1CO$ | −72.59 | −7.73 | −70.29 | −72.13 | −7.76 | −69.82 |
| R83 | $\cdot CHO + \cdot CHO \rightarrow {}^1H_2CO + {}^3CO$ | 66.05 | −5.28 | 67.63 | 73.48 | −5.49 | 75.11 |
| R84 | $\cdot CHO + HNO \rightarrow {}^1H_2CO + \cdot NO$ | −39.79 | −5.04 | −38.28 | −35.80 | −5.19 | −34.25 |
| R85 | $\cdot CHO + HCN \rightarrow {}^1H_2CO + \cdot CN$ | 38.26 | −1.13 | 38.60 | 59.27 | −1.41 | 59.69 |
| R86 | $\cdot CHO + CH_4 \rightarrow {}^1H_2CO + \cdot CH_3$ | 16.47 | 2.09 | 15.84 | 16.74 | 2.10 | 16.12 |
| R87 | $HCN + {}^1H_2O \rightarrow {}^1H_2CO + {}^1NH$ | 127.77 | 0.04 | 127.76 | 143.56 | −0.05 | 143.57 |
| R88 | $HCN + {}^1H_2O \rightarrow {}^1H_2CO + {}^3NH$ | 85.29 | 2.25 | 84.62 | 88.08 | 2.13 | 87.45 |

**Table 2.** continued.

| | | | | | | | |
|---|---|---|---|---|---|---|---|
| R89 | $CH_4 + O(^1D) \rightarrow {}^1H_2CO + 2\cdot H$ | −13.56 | 28.31 | −22.00 | −42.04 | 28.31 | −50.48 |
| R90 | $CH_4 + \cdot O(^3P) \rightarrow {}^1H_2CO + 2\cdot H$ | 36.23 | 26.12 | 28.44 | 25.89 | 26.13 | 18.10 |
| R91 | $CH_4 + O(^1D) \rightarrow {}^1H_2CO + {}^1H_2$ | −117.44 | 4.65 | −118.83 | −135.41 | 4.73 | −136.82 |
| R92 | $CH_4 + \cdot O(^3P) \rightarrow {}^1H_2CO + {}^1H_2$ | −67.65 | 2.47 | −68.38 | −67.48 | 2.54 | −68.24 |
| R93 | $CH_4 + O(^1D) \rightarrow {}^1H_2CO + {}^3H_2$ | 74.39 | 7.79 | 72.07 | 47.99 | 7.80 | 45.66 |
| R94 | $CH_4 + \cdot O(^3P) \rightarrow {}^1H_2CO + {}^3H_2$ | 124.19 | 5.61 | 122.51 | 115.92 | 5.62 | 114.25 |
| R95 | $C_2H_4 + O(^1D) \rightarrow {}^1H_2CO + \cdot {}^1CH_2$ | −103.80 | 12.11 | −107.42 | −61.18 | 12.25 | −64.83 |
| R96 | $C_2H_4 + \cdot O(^3P) \rightarrow {}^1H_2CO + \cdot {}^1CH_2$ | −54.01 | 9.93 | −56.97 | 6.75 | 10.06 | 3.75 |

**Notes.** The presented values of enthalpy ($\Delta H°$), entropy ($\Delta S°$), and Gibbs free-energy ($\Delta G°$) were calculated at the CCSD(T)-F12/cc-pVTZ-F12 (black) and MP2/aug-cc-pVDZ (blue), corrected for ZPE, at a $T_{gas}$ = 298.15 K, and $P_{gas}$ = 1 Atm. The energy units of $\Delta H°$ and $\Delta G°$ are given in kcal mol$^{-1}$, while for $\Delta S°$ are in cal mol$^{-1}$ K$^{-1}$.

**Table 3.** Thermodynamic functions values of reactions able to form $H_2CO$ in DMCs.

| R/id | Reaction mechanism | $\Delta H°$ | $\Delta S°$ | $\Delta G°$ | $\Delta H°$ | $\Delta S°$ | $\Delta G°$ |
|---|---|---|---|---|---|---|---|
| R3 | $^3CO + {}^3H_2 \rightarrow {}^1H_2CO$ | −328.64 | −53.85 | −323.26 | −327.00 | −53.68 | −321.63 |
| R4 | $^3CO + {}^1H_2 \rightarrow {}^1H_2CO$ | −136.81 | 50.71 | −131.74 | −143.60 | −50.61 | −138.54 |
| R5 | $^1CO + {}^3H_2 \rightarrow {}^1H_2CO$ | −190.00 | −51.41 | −184.86 | −181.39 | −51.41 | −176.25 |
| R9 | $^3CO + {}^1H_2O \rightarrow {}^1H_2CO + \cdot O(^3P)$ | −21.17 | −3.97 | −20.77 | −26.13 | −3.85 | −25.75 |
| R12 | $^3CO + NH_3 \rightarrow {}^1H_2CO + {}^3NH$ | −42.38 | −2.30 | −42.15 | −49.18 | −2.18 | −48.96 |
| R17 | $\cdot CH + {}^2OH \rightarrow {}^1H_2CO$ | −175.26 | −85.10 | −166.75 | −178.47 | −85.08 | −169.96 |
| R19 | $\cdot CH + {}^1H_2O \rightarrow {}^1H_2CO + \cdot H$ | −57.78 | −35.97 | −54.19 | −63.07 | −35.98 | −59.47 |
| R20 | $^1CH_2 + O(^1D) \rightarrow {}^1H_2CO$ | −235.94 | −51.79 | −230.76 | −258.05 | −51.79 | −252.87 |
| R21 | $^1CH_2 + \cdot O(^3P) \rightarrow {}^1H_2CO$ | −186.15 | −53.98 | −180.75 | −190.11 | −53.97 | −184.72 |
| R22 | $^3CH_2 + O(^1D) \rightarrow {}^1H_2CO$ | −227.07 | −53.24 | −221.75 | −242.60 | −53.27 | −237.27 |
| R24 | $^1CH_2 + {}^1O_2 \rightarrow {}^1H_2CO + O(^1D)$ | −48.24 | −4.79 | −47.76 | −34.70 | −4.92 | −34.21 |
| R25 | $^1CH_2 + {}^1O_2 \rightarrow {}^1H_2CO + \cdot O(^3P)$ | −98.03 | −2.61 | −97.77 | −102.64 | −2.73 | −102.37 |
| R26 | $^1CH_2 + {}^3O_2 \rightarrow {}^1H_2CO + O(^1D)$ | −19.11 | −6.94 | −18.41 | −4.37 | −7.02 | −3.67 |
| R27 | $^1CH_2 + {}^3O_2 \rightarrow {}^1H_2CO + \cdot O(^3P)$ | −68.90 | −4.75 | −68.42 | −72.31 | −4.83 | −71.82 |
| R28 | $^3CH_2 + {}^3O_2 \rightarrow {}^1H_2CO + \cdot O(^3P)$ | −60.03 | −6.20 | −59.41 | −56.86 | −6.31 | −56.22 |
| R29 | $^1CH_2 + {}^4OH \rightarrow {}^1H_2CO + \cdot H$ | −186.00 | −15.77 | −184.43 | −189.97 | −17.11 | −188.26 |
| R30 | $^1CH_2 + {}^2OH \rightarrow {}^1H_2CO + \cdot H$ | −84.70 | −7.38 | −83.97 | −95.26 | −7.39 | −94.52 |
| R33 | $^3CH_2 + {}^2OH \rightarrow {}^1H_2CO + \cdot H$ | −75.83 | −8.83 | −74.95 | −79.81 | −8.87 | −78.92 |
| R44 | $\cdot CH_3 + O(^1D) \rightarrow {}^1H_2CO + \cdot H$ | −117.80 | −1.96 | −117.61 | −140.99 | −1.94 | −140.79 |
| R45 | $\cdot CH_3 + \cdot O(^3P) \rightarrow {}^1H_2CO + \cdot H$ | −68.01 | −4.14 | −67.60 | −73.05 | −4.13 | −72.64 |
| R46 | $\cdot CH_3 + {}^4OH \rightarrow {}^1H_2CO + {}^1H_2$ | −171.15 | −14.92 | −169.66 | −165.69 | −16.18 | −164.08 |
| R48 | $\cdot CH_3 + {}^2OH \rightarrow {}^1H_2CO + {}^1H_2$ | −69.85 | −6.53 | −69.20 | −70.98 | −6.46 | −70.34 |
| R51 | $\cdot CH_3 + {}^3O_2 \rightarrow {}^1H_2CO + \cdot {}^2OH$ | −52.20 | −1.51 | −52.05 | −50.09 | −1.57 | −49.94 |
| R53 | $\cdot CH_3 + {}^1O_2 \rightarrow {}^1H_2CO + \cdot {}^2OH$ | −81.34 | 0.64 | −81.40 | −80.43 | 0.53 | −80.48 |
| R71 | $\cdot CHO + \cdot H \rightarrow {}^1H_2CO$ | −86.92 | −51.93 | −81.73 | −81.35 | −51.94 | −76.16 |
| R73 | $\cdot CHO + \cdot {}^4OH \rightarrow {}^1H_2CO + \cdot O(^3P)$ | −86.77 | −13.72 | −85.40 | −81.21 | −15.08 | −79.70 |
| R82 | $\cdot CHO + \cdot CHO \rightarrow {}^1H_2CO + {}^1CO$ | −72.39 | −6.61 | −71.73 | −71.93 | −6.64 | −71.26 |
| R84 | $\cdot CHO + HNO \rightarrow {}^1H_2CO + \cdot NO$ | −39.59 | −3.97 | −39.20 | −35.60 | −4.11 | −35.19 |

**Notes.** The values were calculated at the CCSD(T)-F12/cc-pVTZ-F12 (black) and MP2/aug-cc-pVDZ (blue) levels of theory and basis set, which include corrections for ZPE, at $T_{gas}$ = 100 K and $P_{gas}$ = 6.9 × 10$^3$ K cm$^{-3}$. The units of $\Delta H°$ and $\Delta G°$ are given in kcal mol$^{-1}$, while $\Delta S°$ are cal mol$^{-1}$ K$^{-1}$.

interstellar radiation in DMCs is capable of photoionizing any existing atomic carbon ($C_I$), with its predominant form being ionized ($C^+$; Snow & McCall 2006). Additionally, $CH_4$, $CO_2$, and trans-HONO do not form in these environments. Subsequently, 28 reactions composed of reactants already present in DMCs might contribute to the detected amount of formaldehyde ($N(H_2CO)/N(H_2) = \sim 10^{-10}$ cm$^{-3}$; Millar et al. 1979; Liszt & Lucas 1995) in DMCs. The computed values of the thermodynamic functions for these reactions are presented in Table 3. As a result, candidate reactions to produce formaldehyde in this environment are comprised of 11 reagents in addition to neutral atomic ($\cdot H_I$) and molecular hydrogen ($H_2$). To return to Fig. 1, the fractional abundances for these reagents (detected in the ground electronic state) with respect to $H_2$ ($N(\times)/N(H_2)$) as well as the abundance of $H_2CO$ can be understood. This diagram shows that ·CHO, HNO, and $NH_3$ in their ground electronic states are less abundant than $H_2CO$ which affects the reactions composed containing them. From the transition-state energy perspective on PES profiles and after detailed computational work under astrophysical conditions characteristic of DMCs, the emerged (+) / submerged (−) Gibbs free energies

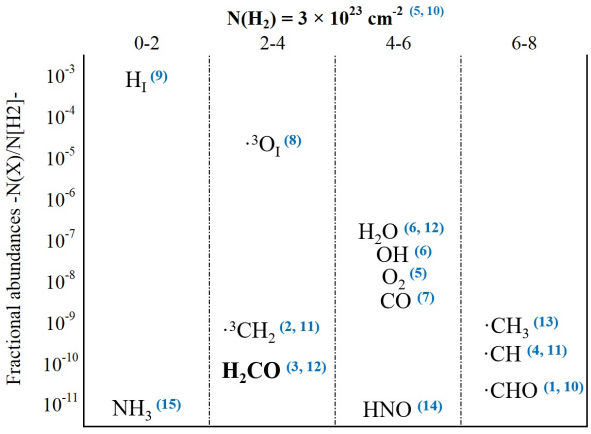


**Fig. 1.** Fractional abundances $N(X)/N(H_2)$ ($cm^{-3}$) of reagents and $H_2CO$ in DMC of reactions from Table 3. References: 1. Liszt et al. (2006). 2. Hollis et al. (1995). 3. Liszt & Lucas (1995). 4. Sheffer et al. (2008). 5. Goldsmith et al. (2000); Larsson et al. (2007); Liseau et al. (2012). 6. Wiesemeyer et al. (2012). 7. Sheffer et al. 2002. 8. Yamamoto (2017). 9. Snow & McCall (2006). 10. Goicoechea & Cernicharo (2001). 11. Polehampton et al. (2005). 12. Millar et al. (1979). 13. Feuchtgruber et al. (2000). 14. Ziurys et al. (1994); Snyder et al. (1993). 15. Liszt et al. (2006).

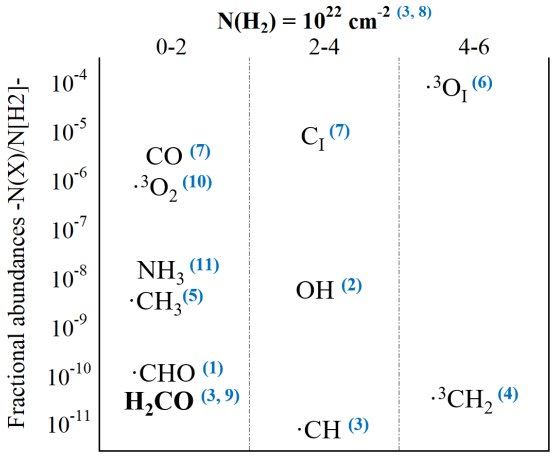


**Fig. 2.** Fractional abundances $N(X)/N(H_2)$ ($cm^{-3}$) of reactants vs. $H_2CO$ as product detected in DCDMCs, and Bok globules. References: 1. Agúndez et al. (2015). 2. Martin & Barrett (1978). 3. Ohishi et al. (1992). 4. Polehampton et al. (2005). 5. Feuchtgruber et al. (2000). 6. Meyer et al. (1997). 7. Cecchi-Pestellini et al. (2001). 8. Sakai et al. (2009). 9. Di Francesco et al. (2002). 10. Aikawa et al. (2008). 11. Marka et al. (2011).

belonging to transition states (in kcal $mol^{-1}$) are presented in Table 4. In this way and after reactions composed of $NH_3$, ·CHO, and HNO were excluded because of their low abundance in this environment, 13 reactions (R9, R17, R24, R25, R26, R27, R28, R30, R33, R44, R45, R46, and R53) with an inner transition state were considered for further discussion.

### 4.2. Dark, cold, and dense molecular clouds

The drop in temperature and increase in gas pressure by one order of magnitude ($T_{gas}$ = 13.2 K and $P_{gas} = 5.3 \times 10^4$ K $cm^{-3}$) representative of DCDMCs promises interesting disparities in molecular energetics compared to DMCs. The main source of energy (UV radiation) in these objects decreases to 4.48 eV (Klessen & Glover 2014), limiting the energy able to ionize, excite, and/or brake or produce new molecular ligands. This energy is in accordance with our computed calculations related to $H_2$ dissociation (4.4855 eV at CCSD(T)-F12/cc-pVTZ-F12 with corrected ZPE). Because there is scant evidence that nitrosyl-hydride (HNO) will be present in DCDMCs and $H_2O$ remains mostly frozen on the dust grain surfaces, R9, R19, and R84 cannot be considered as part of $H_2CO$ production. These reactions were subsequently removed from consideration in this environment. One of the affected species is $C_I$, which might survive as a neutral in DCDMCs (Cecchi-Pestellini et al. 2001). However, as $H_2O$ abundance (the second necessary reactant) is negligible in the gas-phase, R1 cannot be considered either. In Table 5, we list the 25 most probable reactions and their thermodynamic function values, typical of DCDMCs, that are able to produce some quantities of formaldehyde. This means that the 25 reactions mentioned and presented in Table 1 are possible ways to form $H_2CO$ in DCDMCs in the gas-phase.

Their viability will depend upon the density of the reagents, as displayed in Fig. 2, driven again, by a maximum photonic energy of 4.48 eV. In the same figure we show the notably

**Table 4.** Emerged (+) / submerged (−) TS Gibbs free-energy ($\Delta^{\ddagger}G$) relative to the reactants free-energy ($\Delta G^{\circ}$) in DMCs.

| R/id | CCSD(T)-F12/ cc-pVTZ-F12 | MP2/ aug-cc-pVDZ | TS type | Reaction paths |
|---|---|---|---|---|
| R3 | −323.26 | −321.63 | RA | 2 |
| R4 | −131.74 | −138.54 | RA | 2 |
| R5 | −184.86 | −176.25 | RA | 2 |
| R9 | −10.87 | 1.44 | Inner TS | 6 |
| R12 | 6.90 | 18.93 | Outer TS | 6 |
| R17 | −59.72 | −60.03 | Inner TS | 4 |
| R19 | 7.50 | 7.24 | Outer TS | 3 |
| R20 | −230.76 | −252.87 | RA | 2 |
| R21 | −180.75 | −184.72 | RA | 2 |
| R22 | −149.80 | −158.75 | RA | 2 |
| R24 | −47.76 | −34.21 | Inner TS | 3 |
| R25 | −65.05 | −47.26 | Inner TS | 4 |
| R26 | −18.41 | −3.67 | Inner TS | 4 |
| R27 | −35.70 | −16.71 | Inner TS | 3 |
| R28 | −26.69 | −1.11 | Inner TS | 3 |
| R29 | −184.43 | −188.26 | Direct | 2 |
| R30 | −67.94 | −68.62 | Inner TS | 3 |
| R33 | −58.63 | −64.53 | Inner TS | 3 |
| R44 | −110.60 | −126.39 | Inner TS | 3 |
| R45 | −60.60 | −58.24 | Inner TS | 3 |
| R46 | −95.34 | −90.79 | Inner TS | 3 |
| R48 | 5.12 | 2.95 | Outer TS | 3 |
| R51 | 21.30 | 35.21 | Outer TS | 3 |
| R53 | −10.38 | 12.32 | Inner TS | 3 |
| R71 | 9.12 | 12.10 | Outer TS | 3 |
| R73 | −85.40 | −79.70 | Direct | 2 |
| R82 | −8.11 | −9.10 | Inner TS | 3 |
| R84 | 10.39 | 15.90 | Outer TS | 3 |

**Notes.** The presented Gibbs free energy values were calculated at the CCSD(T)-F12/cc-pVTZ-F12 (black) and MP2/aug-cc-pVDZ (blue) levels of theory and basis set, which include corrections for ZPE, at $T_{gas}$ = 100 K and $P_{gas} = 6.9 \times 10^3$ K $cm^{-3}$, for reactions with detected reactants in DMCs. TS type (inner = submerged energy, outer = emerged energy, RA = radiative association), and reaction paths = number of reaction steps required to form products. The energy units of $\Delta G^{\circ}$ are given in kcal $mol^{-1}$.

**Table 5.** Thermodynamic function values of reactions able to form $H_2CO$ in DCDMCs.

| R/id | Reaction mechanism | $\Delta H°$ | $\Delta S°$ | $\Delta G°$ | $\Delta H°$ | $\Delta S°$ | $\Delta G°$ |
|---|---|---|---|---|---|---|---|
| R3 | $^{\cdot 3}CO + {}^{\cdot 3}H_2 \rightarrow {}^1H_2CO$ | −328.12 | −37.73 | −327.63 | −326.48 | −37.56 | −325.99 |
| R4 | $^{\cdot 3}CO + {}^1H_2 \rightarrow {}^1H_2CO$ | −136.29 | −34.59 | −135.83 | −143.08 | −34.49 | −142.63 |
| R5 | $^1CO + {}^{\cdot 3}H_2 \rightarrow {}^1H_2CO$ | −189.48 | −35.29 | −189.01 | −180.88 | −35.28 | −180.41 |
| R12 | $^{\cdot 3}CO + NH_3 \rightarrow {}^1H_2CO + {}^{\cdot 3}NH$ | −42.38 | −2.30 | −42.35 | −49.18 | −2.18 | −49.15 |
| R17 | $\cdot CH + {}^{\cdot 2}OH \rightarrow {}^1H_2CO$ | −174.74 | −66.96 | −173.86 | −177.95 | −66.95 | −177.07 |
| R20 | $^1CH_2 + O(^1D) \rightarrow {}^1H_2CO$ | −235.51 | −37.68 | −235.01 | −257.62 | −37.68 | −257.12 |
| R21 | $^1CH_2 + \cdot O(^3P) \rightarrow {}^1H_2CO$ | −185.72 | −39.87 | −185.19 | −189.68 | −39.86 | −189.16 |
| R22 | $^{\cdot 3}CH_2 + O(^1D) \rightarrow {}^1H_2CO$ | −226.64 | −39.13 | −226.12 | −242.17 | −39.16 | −241.65 |
| R24 | $^1CH_2 + {}^1O_2 \rightarrow {}^1H_2CO + O(^1D)$ | −48.15 | −0.77 | −48.14 | −34.62 | −0.89 | −34.61 |
| R25 | $^1CH_2 + {}^1O_2 \rightarrow {}^1H_2CO + \cdot O(^3P)$ | −97.94 | 1.42 | −97.96 | −102.55 | 1.29 | −102.57 |
| R26 | $^1CH_2 + {}^{\cdot 3}O_2 \rightarrow {}^1H_2CO + O(^1D)$ | −19.02 | −2.91 | −18.98 | −4.29 | −2.99 | −4.25 |
| R27 | $^1CH_2 + {}^{\cdot 3}O_2 \rightarrow {}^1H_2CO + \cdot O(^3P)$ | −68.81 | −0.73 | −68.80 | −72.22 | −0.81 | −72.21 |
| R28 | $^3CH_2 + {}^3O_2 \rightarrow {}^1H_2CO + \cdot O(^3P)$ | −59.94 | −2.18 | −59.91 | −56.77 | −2.29 | −56.74 |
| R29 | $^1CH_2 + {}^{\cdot 4}OH \rightarrow {}^1H_2CO + \cdot H$ | −185.72 | −9.67 | −185.59 | −189.66 | −10.18 | −189.52 |
| R30 | $^1CH_2 + {}^{\cdot 2}OH \rightarrow {}^1H_2CO + \cdot H$ | −84.53 | −3.36 | −84.49 | −95.09 | −3.37 | −95.05 |
| R33 | $^{\cdot 3}CH_2 + {}^{\cdot 2}OH \rightarrow {}^1H_2CO + \cdot H$ | −75.66 | −4.81 | −75.60 | −79.64 | −4.85 | −79.57 |
| R44 | $\cdot CH_3 + O(^1D) \rightarrow {}^1H_2CO + \cdot H$ | −117.80 | −1.94 | −117.78 | −140.98 | −1.93 | −140.96 |
| R45 | $\cdot CH_3 + \cdot O(^3P) \rightarrow {}^1H_2CO + \cdot H$ | −68.01 | −4.13 | −67.96 | −73.05 | −4.11 | −72.99 |
| R46 | $\cdot CH_3 + {}^{\cdot 4}OH \rightarrow {}^1H_2CO + {}^1H_2$ | −171.03 | −12.83 | −170.87 | −165.55 | −13.26 | −165.37 |
| R48 | $\cdot CH_3 + {}^{\cdot 2}OH \rightarrow {}^1H_2CO + {}^1H_2$ | −69.85 | −6.52 | −69.77 | −70.98 | −6.45 | −70.90 |
| R51 | $\cdot CH_3 + {}^{\cdot 3}O_2 \rightarrow {}^1H_2CO + {}^{\cdot 2}OH$ | −52.29 | −1.50 | −52.27 | −50.18 | −1.55 | −50.16 |
| R53 | $\cdot CH_3 + {}^1O_2 \rightarrow {}^1H_2CO + {}^{\cdot 2}OH$ | −81.42 | 0.65 | −81.43 | −80.51 | 0.55 | −80.52 |
| R71 | $\cdot CHO + \cdot H \rightarrow {}^1H_2CO$ | −86.49 | −37.82 | −85.99 | −80.92 | −37.83 | −80.42 |
| R73 | $\cdot CHO + \cdot {}^4OH \rightarrow {}^1H_2CO + \cdot O(^3P)$ | −86.48 | −7.62 | −86.38 | −80.90 | −8.15 | −80.79 |
| R82 | $\cdot CHO + \cdot CHO \rightarrow {}^1H_2CO + {}^1CO$ | −72.30 | −4.60 | −72.24 | −71.84 | −4.63 | −71.78 |

**Notes.** The presented values were calculated at the CCSD(T)-F12/cc-pVTZ-F12 (black) and MP2/aug-cc-pVDZ (blue) levels of theory and basis set with corrected ZPE, at $T_{gas}$ = 13.2 K and $P_{gas}$ = 5.3 × $10^4$ K cm$^{-3}$. The energy units of $\Delta H°$ and $\Delta G°$ are given in kcal mol$^{-1}$ while for $\Delta S°$ are in cal mol$^{-1}$ K$^{-1}$.

**Table 6.** Emerged (+) / submerged (−) TS Gibbs free-energy ($\Delta^{\ddagger}G$) relative to the reactants free-energy ($\Delta G°$) in DCDMCs.

| R/id | CCSD(T)-F12/ cc-pVTZ-F12 | MP2/ aug-cc-pVDZ | TS type | Reaction paths |
|---|---|---|---|---|
| R3 | −327.63 | −325.99 | RA | 2 |
| R4 | −135.83 | −142.63 | RA | 2 |
| R5 | −189.01 | −180.41 | RA | 2 |
| R12 | −4.18 | 14.35 | Outer TS | 6 |
| R17 | −66.50 | −66.82 | Inner TS | 4 |
| R20 | −235.01 | −257.12 | RA | 2 |
| R21 | −185.19 | −189.16 | RA | 2 |
| R22 | −153.84 | −162.80 | RA | 2 |
| R24 | −48.14 | −34.61 | Inner TS | 3 |
| R25 | −69.38 | −51.60 | Inner TS | 4 |
| R26 | −18.98 | −4.25 | Inner TS | 4 |
| R27 | −40.22 | −21.24 | Inner TS | 3 |
| R28 | −31.33 | −5.76 | Inner TS | 3 |
| R29 | −185.59 | −189.52 | Direct | 2 |
| R30 | −67.94 | −68.62 | Inner TS | 3 |
| R33 | −58.63 | −52.73 | Inner TS | 3 |
| R44 | −114.53 | −130.32 | Inner TS | 3 |
| R45 | −64.71 | −62.36 | Inner TS | 3 |
| R46 | −100.43 | −95.98 | Inner TS | 3 |
| R48 | 0.67 | −1.50 | Outer TS | 3 |
| R51 | 16.65 | 30.56 | Outer TS | 3 |
| R53 | −14.83 | 7.86 | Inner TS | 3 |
| R71 | 5.24 | 8.21 | Outer TS | 3 |
| R73 | −86.38 | −80.79 | Direct | 2 |
| R82 | −13.36 | −14.36 | Inner TS | 3 |

**Notes.** The presented values were calculated at the CCSD(T)-F12/cc-pVTZ-F12 (black) and MP2/aug-cc-pVDZ (blue) levels of theory and basis set which include corrections for ZPE, at $T_{gas}$ = 13.2 K and 5.30 × $10^4$ K cm$^{-3}$ K cm$^{-3}$ for reactions with detected reactants in DCDMCs. TS type (inner = submerged energy, outer = emerged energy, RA = radiative association), and reaction paths = number of reaction steps required to form products. The energy units of $\Delta G°$ are kcal mol$^{-1}$.

increasing abundances of oxygen (atomic and molecular) in DCDMCs, as well as the remarkable reduction of ·CH and $^{\cdot 3}CH_2$ below the $H_2CO$ abundance. This will undeniably affect formaldehyde production through the most promising channels R27 & R28. In contraposition, DCDMCs are richer in ·CHO, exceeding $H_2CO$ abundances, reinforcing the role of R71 in this scenario from the perspective of the molecular density. Exothermic and exergonic reaction mechanisms (as is the case presently) are expected to be more spontaneous and highly favor increasing kinetic feasibility. This is the case of reactions that correspond in particular to reaction mechanisms with submerged TS(s), and thus, with a higher energy respect to the reactants energy. The emerged (+) / submerged (–) Gibbs free energies belonging to transition states to respect the asymptotic energy of the reactants, at the two levels of theory and basis sets per reaction ID, are presented for this type of astronomic environment in Table 6. This shows that the most probable mechanisms with submerged TS able to produce $H_2CO$ are R24, R25, R26, R27, R28, R30, R33, R44, R45, R46, R53, and R82, when reactions with methylidyne (·CH; see Fig. 2) are excluded.

### 4.3. Circumstellar envelopes of low-mass protostars

Applying the P&T profiles defined in Sect. 2 for the three regions of IRAS 16293 our computations imply that 56 mechanisms possess valid reaction thermodynamic function values to proceed with the formation of $H_2CO$. Twenty-six of these can produce $H_2CO$ in region I, 32 in region II, and 33 in region III (please see Table 7). These are the amended reactions with detected reagents in every region of the disk. The presence of methane ($CH_4$) and neutral atomic carbon ($C_I$) in this astronomical object, in addition to trans-HONO in region III (detected at ∼150 AU from the core – Coutens et al. 2019), confirms the hypothetical feasibility of these mechanisms. Moreover, because nitrosyl hydride (HNO) has not been detected in IRAS 16293, R84 cannot be included in any circumstellar envelope region, as it was in DCDMCs. In Fig. 3 we show the abundance of reactants and formaldehyde itself already detected in the three regions of the disk. They have been calculated for the methylene ($^{\cdot 3}CH_2$) (Vasyunin & Herbst 2013), methyl radical ($\cdot CH_3$) (Sakai et al. 2012; Woon 2002), and methane ($CH_4$) (Sakai et al. 2012) ground electronic state abundances rather than detected. The reason is that they are planar (or linear) symmetric-top molecules and therefore have a small permanent electric dipole moment, which makes them undetectable through terrestrial radio telescopes by rotational spectroscopy. On the other side of the spectrum, neither high-resolution infrared absorption nor ultraviolet-visible spectroscopy telescopes can identify them in the gas-phase because they lack of a powerful enough source of electromagnetic radiation. The abundance values for the triplet ground-state of methylene ($\cdot CH_2(X^3B_1)$) have therefore been estimated by using Monte Carlo algorithms (Vasyunin & Herbst 2013) which in turn are based on known abundances of derived species. The presence of the methyl radical ($\cdot CH_3$) in region I just before the CO depletion zone from icy grains should be negligible because $\cdot CH_3$ is thought to be mainly produced in this region by $CH_4$ photodissociation (Sakai et al. 2012) and $CH^3OH$ (Woon 2002) desorbs from the grains in region II. Consequently, reactions based on

**Table 7.** Thermodynamic function values of reactions able to form $H_2CO$ in CELMPs.

| | | Region I (20K) | | | | | | Region II (80K) | | | | | | Region III (150K) | | | | | |
|---|---|---|---|---|---|---|---|---|---|---|---|---|---|---|---|---|---|---|---|
| R/id | Mechanism | $\Delta H^\circ_{20}$ | $\Delta S^\circ_{20}$ | $\Delta G^\circ_{20}$ | $\Delta H^\circ_{20}$ | $\Delta S^\circ_{20}$ | $\Delta G^\circ_{20}$ | $\Delta H^\circ_{80}$ | $\Delta S^\circ_{80}$ | $\Delta G^\circ_{80}$ | $\Delta H^\circ_{80}$ | $\Delta S^\circ_{80}$ | $\Delta G^\circ_{80}$ | $\Delta H^\circ_{150}$ | $\Delta S^\circ_{150}$ | $\Delta G^\circ_{150}$ | $\Delta H^\circ_{150}$ | $\Delta S^\circ_{150}$ | $\Delta G^\circ_{150}$ |
| R1 | $\cdot C + {}^1H_2O \rightarrow {}^1H_2CO$ | −137.24 | −27.55 | −136.69 | −132.57 | −27.53 | −132.02 | −137.54 | −32.20 | −134.96 | −132.87 | −32.18 | −130.29 | −137.88 | −31.04 | −133.23 | −133.21 | −31.02 | −128.56 |
| R3 | $^3CO + {}^3H_2 \rightarrow {}^1H_2CO$ | −328.17 | −28.15 | −327.60 | −326.52 | −27.98 | −325.96 | −328.52 | −34.18 | −325.79 | −326.88 | −34.01 | −324.16 | −328.94 | −33.64 | −323.89 | −327.30 | −33.47 | −322.28 |
| R4 | $^3CO + {}^1H_2 \rightarrow {}^1H_2CO$ | −136.33 | −25.00 | −135.83 | −143.12 | −24.91 | −142.62 | −136.69 | −31.03 | −134.21 | −143.48 | −30.93 | −141.00 | −137.11 | −30.50 | −132.53 | −143.90 | −30.40 | −139.34 |
| R5 | $^1CO + {}^3H_2 \rightarrow {}^1H_2CO$ | −189.52 | −25.70 | −189.01 | −180.92 | −25.70 | −180.40 | −189.88 | −31.73 | −187.34 | −181.27 | −31.73 | −178.74 | −190.29 | −31.20 | −185.62 | −181.69 | −31.19 | −177.01 |
| R9 | $^3CO + {}^1H_2O \rightarrow {}^1H_2CO + \cdot O(^3P)$ | −21.01 | −0.77 | −21.00 | −25.97 | −0.65 | −25.96 | −21.13 | −3.52 | −20.85 | −26.09 | −3.40 | −25.82 | −21.27 | −4.77 | −20.55 | −26.23 | −4.65 | −25.53 |
| R12 | $^3CO + NH_3 \rightarrow {}^1H_2CO + {}^3NH$ | −42.38 | −2.30 | −42.34 | −49.18 | −2.18 | −49.13 | −42.38 | −2.30 | −42.20 | −49.18 | −2.18 | −49.00 | −42.38 | −2.30 | −42.04 | −49.18 | −2.18 | −48.85 |
| R17 | $\cdot CH + {}^2OH \rightarrow {}^1H_2CO$ | −174.78 | −57.79 | −173.63 | −177.99 | −57.78 | −176.83 | −175.14 | −65.20 | −169.93 | −178.35 | −65.18 | −173.13 | −175.56 | −65.29 | −165.76 | −178.76 | −65.27 | −168.97 |
| R19 | $\cdot CH + {}^1H_2O \rightarrow {}^1H_2CO + \cdot H$ | −57.62 | −31.17 | −57.00 | −62.91 | −31.18 | −62.28 | −57.74 | −35.30 | −54.92 | −63.03 | −35.32 | −60.20 | −57.88 | −37.17 | −52.31 | −63.17 | −37.19 | −57.59 |
| R20 | $^1CH_2 + O(^1D) \rightarrow {}^1H_2CO$ | −235.55 | −27.69 | −234.99 | −257.65 | −27.68 | −257.10 | −235.84 | −32.34 | −233.26 | −257.95 | −32.33 | −255.36 | −236.19 | −31.18 | −231.51 | −258.30 | −31.17 | −253.62 |
| R21 | $^1CH_2 + \cdot O(^3P) \rightarrow {}^1H_2CO$ | −185.75 | −29.87 | −185.16 | −189.72 | −29.86 | −189.12 | −186.05 | −34.52 | −183.29 | −190.01 | −34.51 | −187.25 | −186.40 | −33.36 | −181.40 | −190.36 | −33.36 | −185.36 |
| R22 | $^3CH_2 + O(^1D) \rightarrow {}^1H_2CO$ | −226.67 | −29.14 | −226.09 | −242.20 | −29.16 | −241.62 | −226.97 | −33.79 | −224.27 | −242.50 | −33.81 | −239.79 | −227.32 | −32.63 | −222.43 | −242.85 | −32.65 | −237.95 |
| R24 | $^1CH_2 + {}^1O_2 \rightarrow {}^1H_2CO + O(^1D)$ | −48.16 | −1.59 | −48.13 | −34.62 | −1.72 | −34.59 | −48.22 | −4.35 | −47.87 | −34.68 | −4.47 | −34.33 | −48.29 | −5.60 | −47.45 | −34.75 | −5.72 | −33.90 |
| R25 | $^1CH_2 + {}^1O_2 \rightarrow {}^1H_2CO + \cdot O(^3P)$ | −97.95 | 0.59 | −97.96 | −102.56 | 0.47 | −102.57 | −98.01 | −2.16 | −97.84 | −102.62 | −2.29 | −102.44 | −98.08 | −3.41 | −97.57 | −102.69 | −3.54 | −102.16 |
| R26 | $^1CH_2 + {}^3O_2 \rightarrow {}^1H_2CO + O(^1D)$ | −19.03 | −3.74 | −18.95 | −4.29 | −3.82 | −4.22 | −19.09 | −6.49 | −18.57 | −4.35 | −6.57 | −3.83 | −19.16 | −7.74 | −17.99 | −4.42 | −7.82 | −3.25 |
| R27 | $^1CH_2 + {}^3O_2 \rightarrow {}^1H_2CO + \cdot O(^3P)$ | −68.82 | −1.55 | −68.79 | −72.23 | −1.63 | −72.19 | −68.88 | −4.31 | −68.53 | −72.29 | −4.39 | −71.94 | −68.95 | −5.56 | −68.11 | −72.36 | −5.64 | −71.51 |
| R28 | $^3CH_2 + {}^3O_2 \rightarrow {}^1H_2CO + \cdot O(^3P)$ | −59.95 | −3.00 | −59.89 | −56.78 | −3.12 | −56.71 | −60.01 | −5.76 | −59.55 | −56.84 | −5.87 | −56.37 | −60.08 | −7.01 | −59.03 | −56.91 | −7.12 | −55.84 |
| R29 | $^1CH_2 + \cdot {}^4OH \rightarrow {}^1H_2CO + \cdot H$ | −185.73 | −10.57 | −185.52 | −189.68 | −11.30 | −189.45 | −185.93 | −14.93 | −184.73 | −189.90 | −16.24 | −188.60 | −186.20 | −17.34 | −183.60 | −190.17 | −18.70 | −187.37 |
| R30 | $^1CH_2 + \cdot {}^2OH \rightarrow {}^1H_2CO + \cdot H$ | −84.54 | −4.18 | −84.46 | −95.10 | −4.19 | −95.02 | −84.66 | −6.94 | −84.11 | −95.22 | −6.95 | −94.67 | −84.80 | −8.19 | −83.57 | −95.36 | −8.20 | −94.13 |
| R31 | $^1CH_2 + CO_2 \rightarrow {}^1H_2CO + {}^1CO$ | −60.94 | 1.48 | −60.97 | −63.42 | 1.50 | −63.45 | −60.94 | 1.48 | −61.06 | −63.42 | 1.50 | −63.54 | −60.95 | 1.44 | −61.16 | −63.43 | 1.44 | −63.65 |
| R33 | $^3CH_2 + \cdot {}^2OH \rightarrow {}^1H_2CO + \cdot H$ | −75.67 | −5.63 | −75.56 | −79.65 | −5.68 | −79.54 | −75.79 | −8.39 | −75.12 | −79.77 | −8.43 | −79.10 | −75.93 | −9.64 | −74.49 | −79.91 | −9.68 | −78.46 |
| R44 | $\cdot CH_3 + O(^1D) \rightarrow {}^1H_2CO + \cdot H$ | | | | | | | −117.80 | −1.95 | −117.65 | −140.98 | −1.93 | −140.83 | −117.81 | −2.03 | −117.51 | −141.00 | −2.03 | −140.69 |
| R45 | $\cdot CH_3 + \cdot O(^3P) \rightarrow {}^1H_2CO + \cdot H$ | | | | | | | −68.01 | −4.13 | −67.68 | −73.05 | −4.12 | −72.72 | −68.02 | −4.22 | −67.39 | −73.06 | −4.21 | −72.43 |
| R46 | $\cdot CH_3 + \cdot {}^4OH \rightarrow {}^1H_2CO + {}^1H_2$ | | | | | | | −171.12 | −14.51 | −169.95 | −165.65 | −15.74 | −164.40 | −171.26 | −15.76 | −168.89 | −165.80 | −17.05 | −163.24 |
| R48 | $\cdot CH_3 + \cdot {}^2OH \rightarrow {}^1H_2CO + {}^1H_2$ | | | | | | | −69.85 | −6.52 | −69.33 | −70.98 | −6.45 | −70.46 | −69.86 | −6.61 | −68.87 | −70.99 | −6.55 | −70.01 |
| R51 | $\cdot CH_3 + {}^3O_2 \rightarrow {}^1H_2CO + \cdot {}^2OH$ | | | | | | | −52.22 | −1.50 | −52.10 | −50.11 | −1.56 | −49.99 | −52.17 | −1.59 | −51.93 | −50.06 | −1.65 | −49.81 |
| R53 | $\cdot CH_3 + {}^1O_2 \rightarrow {}^1H_2CO + \cdot {}^2OH$ | | | | | | | −81.36 | 0.65 | −81.41 | −80.45 | 0.54 | −80.49 | −81.30 | 0.56 | −81.38 | −80.39 | 0.45 | −80.46 |
| R71 | $\cdot CHO + \cdot H \rightarrow {}^1H_2CO$ | −86.52 | −27.82 | −85.97 | −80.95 | −27.84 | −80.40 | −86.82 | −32.47 | −84.22 | −81.25 | −32.49 | −78.65 | −87.17 | −31.32 | −82.47 | −81.60 | −31.33 | −76.90 |
| R73 | $\cdot CHO + \cdot {}^4OH \rightarrow {}^1H_2CO + \cdot O(^3P)$ | −86.50 | −8.52 | −86.33 | −80.91 | −9.27 | −80.73 | −86.70 | −12.88 | −85.67 | −81.13 | −14.21 | −80.00 | −86.97 | −15.29 | −84.67 | −81.41 | −16.68 | −78.91 |
| R81 | $\cdot CHO + trans\text{–}HONO \rightarrow {}^1H_2CO + \cdot NO_2$ | | | | | | | | | | | | | −1.89 | −0.86 | −1.76 | −10.73 | −1.24 | −10.55 |
| R82 | $\cdot CHO + \cdot CHO \rightarrow {}^1H_2CO + {}^1CO$ | −72.31 | −5.01 | −72.21 | −71.85 | −5.04 | −71.75 | −72.37 | −6.39 | −71.86 | −71.91 | −6.42 | −71.39 | −72.44 | −7.01 | −71.39 | −71.98 | −7.05 | −70.92 |
| R89 | $CH_4 + O(^1D) \rightarrow {}^1H_2CO + 2\cdot H$ | −14.94 | 27.35 | −15.49 | −43.42 | 27.36 | −43.97 | −14.65 | 32.01 | −17.21 | −43.12 | 32.02 | −45.68 | −14.30 | 30.85 | −18.93 | −42.78 | 30.86 | −47.40 |
| R91 | $CH_4 + O(^1D) \rightarrow {}^1H_2CO + {}^1H_2$ | −117.99 | −0.72 | −117.98 | −135.97 | −0.64 | −135.95 | −117.88 | 2.03 | −118.04 | −135.85 | 2.11 | −136.02 | −117.74 | 3.28 | −118.23 | −135.71 | 3.36 | −136.21 |
| R92 | $CH_4 + \cdot O(^3P) \rightarrow {}^1H_2CO + {}^1H_2$ | −68.20 | −2.91 | −68.14 | −68.03 | −2.82 | −67.97 | −68.08 | −0.15 | −68.07 | −67.91 | −0.07 | −67.91 | −67.94 | 1.10 | −68.11 | −67.77 | 1.18 | −67.95 |

**Notes.** The thermodynamic values were calculated at the CCSD(T)-F12/cc-pVTZ-F12 (black) and MP2/aug-cc-pVDZ (blue) levels of theory and basis set, corrected for ZPE. The considered temperature and pressure for calculations for the different regions were as following: region I - $T_{gas}$ = 20 K and $P_{gas} = 2.29 \times 10^7$ K cm$^{-3}$, region II - $T_{gas}$ = 80 K and $P_{gas} = 7.06 \times 10^7$ K cm$^{-3}$, and region III - $T_{gas}$ = 150 K and $P_{gas} = 6.08 \times 10^8$ K cm$^{-3}$. The energy units of $\Delta H^\circ$ and $\Delta G^\circ$ are given in kcal mol$^{-1}$ while for $\Delta S^\circ$ are in cal mol$^{-1}$ K$^{-1}$. In gray we highlight reactions that were excluded for lack of detected reactants in that specific region (see text).

$\cdot CH_3$ were considered only for regions II and III, assuming for both an abundance of $6.40 \times 10^{-9}$ cm$^{-3}$ (Sakai et al. 2012).

Methane ($CH_4$) is known to play a crucial role in the chemical processes belonging to envelopes of low-mass protostars. Hence, the $CH_4$ abundances considered in this work were determined from $CH^3D$ abundances, tentatively detected in IRAS 16293 by Sakai et al. (2012). As described above, Fig. 3 shows the chemical species and their associated abundances that are detected or calculated in three regions of IRAS 16293. In addition, the figure shows three desorption zones (upright gray bars) in which CO, $H_2CO$, and $H_2O$ are thought that are returned into the gas-phase due to grain mantles heating by radiation of YSO. This in turn allows us to better understand the increase in the abundance with rising temperature, and to determine the species that accompany these molecules. $\cdot CHO$ is the only species below the formaldehyde abundance that is detected in all regions of IRAS 16293, but $\cdot OH$, $H_2O$, CO, and $C_I$ remain above the $H_2CO$ abundance in the three regions. The abundances of excited chemical compounds present in the reactions in Table 7 are considered below. In Fig. 3, we show an increase of one order of magnitude increase in $H_2CO$ abundance in region II compared to region I. This value increases up to three orders of magnitude in region III. This growth in abundance is normally attributed to formaldehyde desorption of $H_2CO$ from the ice grain mantles. By applying the deducted OTP of 3:1 (Ceccarelli et al. 2000, 2001) in evaporation regions II and III, an abundance of $1.33 \times 10^{-9}$ cm$^{-3}$ for para-$H_2CO$ in region II can therefore be estimated, while for region III, this would be $3.33 \times 10^{-8}$ cm$^{-3}$. This is the $H_2CO$ amount to be formed in the gas-phase for reactions proposed in regions II and III after the destruction processes that may occur. As in previous scenarios, according to computations and as shown in Table 8, an initial classification of the reactions according to the values of their emerged or submerged TS Gibbs free-energy with respect to the reactants per region of the disk is presented.

### 4.4. Considerations about electronically excited reactants

All chemical compounds illustrated in Figs. 1–3 detected in DMCs, DCDMCs, and CELMPs, respectively, correspond to species in ground electronic states. However, some of the reactions proposed and presented in Table 3, Table 5, and Table 7 are composed of reactants which are in an excited electronic state. These reagents are $CH_2(a^1A_1)$, $O_2(^1\Delta_g)$, $O_I(^1D)$, $\cdot OH(^4\Pi)$, $\cdot CO(^3\Pi)$, and $H_2(^3\Sigma)$. As a first approach, we computationally calculated excitation enthalpies with CCSD(T)-F12/cc-pVTZ-F12 with corrected ZPE for a temperature range between 13.2–150 K. The results are presented in Table 9. We list the most notable observations below:

– i. According to our calculations, the $\cdot CH_2(X^3B_1)$ ground-state requires a photonic energy of only 0.38 eV (or 8.87 kcal mol$^{-1}$) to access the singlet-excited level

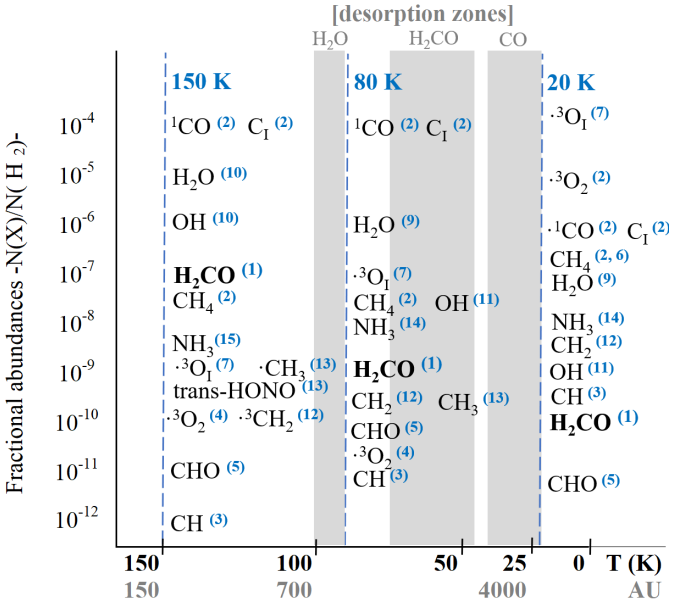


**Fig. 3.** Chemical species and detected fractional abundances in the three studied regions of IRAS 16293. Upright bars in gray correspond to desorption zones of $H_2O$, $H_2CO$ and CO (see text). The temperature is given in K, the molecular density in $cm^{-3}$, and the distance in AU. References: 1. Ceccarelli et al. (2001). 2. Doty et al. (2004). 3. Bottinelli et al. (2014). 4. Carty et al. (2005). 5. Rivilla et al. (2018). 6. Sakai et al. (2012). 7. Aikawa et al. (2015). 8. Coutens et al. (2019). 9. Crimier et al. (2010). 10. Ceccarelli et al. (1998). 11. Parise et al. (2012). 12. Monte Carlo calculations from Vasyunin & Herbst (2013). 13. Sakai et al. (2012). 14. Hily-Blant et al. (2010). 15. Schwarz & Bergin (2014).

$CH_2(a^1A_1)$, which agrees well with experiments (Leopold et al. 1985). However, methylene $CH_2(a^1A_1)$ could have a second formation route from methane photolysis (Gans et al. 2011; Lodriguito et al. 2009; Park et al. 2008; Wang et al. 2000) which produces ~50% of $CH_2(a^1A_1)$ in its photodissociation. The energy required for a primary decomposition $CH_4$ is 5.01 eV, (or 115.53 kcal $mol^{-1}$) according to Blitz & Seakins (2012). Consequently, the abundances for $CH_2(a^1A_1)$ incorporating the second formation route are amended, which mainly affects IRAS 16293 region III.

– ii. The principal accepted source for $O(^1D)$ in cold gas clouds is also produced by photodissociation through reactions $O_2(^3\Sigma_g^-) + h\nu \rightarrow O_I(^3P) + O_I(^1D)$ and $CO_2(^1\Sigma^+) + h\nu \rightarrow CO(^1)\Sigma + O_I(^1D)$ at 2424 Å (5.15 eV) and 2275 Å (5.45 eV), respectively (d'Hendecourt et al. 1986; from von Hagen 1982). Therefore its abundance in this regard is accommodated in scenarios in which the required energy might be present.
– iii. $O_2(^1\Delta_g)$ formation from triplet ground-state species by direct radiation is highly unlikely because this state corresponds to a forbidden transition. Subsequently, and after pathways from $H_2O_2$ or from more complex molecules were discarded, the most probable way of forming singlet molecular oxygen in the cold ISM is in icy grain mantles of amorphous solid water (ASW) through the reaction $O(^3P) + O(^3P) \rightarrow O_2(^1\Delta_g)$ as Pezzella et al. (2020) experimentally demonstrated.
– iv. $\cdot CO(^3\Pi)$ abundances were revised, considering that one-third of the singlet species might be applicable according to Ridgway et al. (1976) and Burke et al. (1996), in studies of the cold regions of the ISM.

**Table 8.** Emerged (+) / submerged (−) TS Gibbs free-energy ($\Delta^{\ddagger}G$) relative to the reactants free-energy ($\Delta G°$) in CELMPs.

| | Region I (20K) | | Region II (80K) | | Region III (150K) | | | |
|---|---|---|---|---|---|---|---|---|
| R/id | CCSD(T)-F12 | MP2 | CCSD(T)-F12 | MP2 | CCSD(T)-F12 | MP2 | TS type | R/paths |
| R1 | 7.42 | 11.46 | 8.89 | 12.93 | 10.32 | 14.37 | Outer TS | 5 |
| R3 | −327.60 | −325.96 | −325.79 | −324.16 | −323.89 | −322.28 | RA | 2 |
| R4 | −135.83 | −142.62 | −134.21 | −141.00 | −132.53 | −139.34 | RA | 2 |
| R5 | −189.01 | −180.40 | −187.34 | −178.74 | −185.62 | −177.01 | RA | 3 |
| R9 | −21.42 | −3.15 | −14.96 | −1.16 | −7.59 | 0.98 | Inner TS | 6 |
| R12 | −3.64 | 14.38 | 2.81 | 16.35 | 10.16 | 18.41 | Outer TS | 6 |
| R17 | −66.30 | −66.61 | −62.82 | −63.13 | −58.92 | −59.22 | Inner TS | 4 |
| R19 | 0.91 | 0.65 | 4.39 | 4.13 | 8.33 | 8.08 | Outer TS | 3 |
| R20 | −234.99 | −257.10 | −233.26 | −255.36 | −231.51 | −253.62 | RA | 2 |
| R21 | −185.16 | −189.12 | −183.29 | −187.25 | −181.40 | −185.36 | RA | 2 |
| R22 | −153.83 | −162.79 | −152.24 | −161.20 | −150.67 | −159.62 | RA | 2 |
| R24 | −48.13 | −34.59 | −47.87 | −34.33 | −47.45 | −33.90 | Inner TS | 3 |
| R25 | −69.37 | −51.59 | −67.58 | −49.79 | −65.70 | −47.90 | Inner TS | 4 |
| R26 | −18.95 | −4.22 | −18.57 | −3.83 | −17.99 | −3.25 | Inner TS | 4 |
| R27 | −40.19 | −21.21 | −38.28 | −19.28 | −36.25 | −17.24 | Inner TS | 3 |
| R28 | −31.29 | −5.72 | −29.29 | −3.71 | −27.16 | −1.57 | Inner TS | 3 |
| R29 | −185.52 | −189.45 | −184.73 | −188.60 | −183.60 | −187.37 | Direct | 2 |
| R30 | −74.58 | −75.29 | −72.85 | −73.55 | −71.08 | −71.78 | Inner TS | 3 |
| R31 | −19.32 | −23.99 | −17.34 | −22.00 | −15.22 | −19.87 | Inner TS | 3 |
| R33 | −65.68 | −59.81 | −63.86 | −57.98 | −61.99 | −56.10 | Inner TS | 3 |
| R44 | | | −113.02 | −128.80 | −111.56 | −127.34 | Inner TS | 3 |
| R45 | | | −63.06 | −60.70 | −61.45 | −59.09 | Inner TS | 3 |
| R46 | | | −98.07 | −93.54 | −95.45 | −90.82 | Inner TS | 3 |
| R48 | | | 2.56 | 0.39 | 4.57 | 2.41 | Outer TS | 3 |
| R51 | | | 18.69 | 32.60 | 20.87 | 34.76 | Outer TS | 3 |
| R53 | −14.80 | 7.88 | −12.94 | 9.76 | −10.96 | 11.75 | Inner TS | 3 |
| R71 | 5.23 | 8.21 | 6.71 | 9.69 | 8.15 | 11.13 | Outer TS | 3 |
| R73 | −86.33 | −80.73 | −85.67 | −80.00 | −84.67 | −78.91 | Direct | 2 |
| R81 | | | | | 24.87 | 45.37 | Outer TS | 2 |
| R82 | −13.28 | −14.28 | −10.86 | −11.86 | −8.19 | −9.17 | Inner TS | 3 |
| R89 | −13.00 | −33.21 | −12.53 | −32.73 | −12.66 | −32.86 | Inner TS | 4 |
| R91 | −48.24 | −67.71 | −46.83 | −66.30 | −45.47 | −64.93 | Inner TS | 3 |
| R92 | 1.60 | 0.27 | 3.14 | 1.81 | 4.65 | 3.33 | Outer TS | 3 |

**Notes.** The presented values were calculated at the CCSD(T)-F12/cc-pVTZ-F12 (black) and MP2/aug-cc-pVDZ (blue) which include corrections for ZPE; TS type (inner = submerged energy; outer = emerged energy; RA = radiative association; reaction paths = number of reaction steps required to form products. The considered temperature and pressure for calculations for the different regions were as following: region I/ $T_{gas}$ = 20 K and $P_{gas} = 2.29 \times 10^7$ K $cm^{-3}$, region II/ $T_{gas}$ = 80 K and $P_{gas} = 7.06 \times 10^7$ K $cm^{-3}$, and region III/ $T_{gas}$ = 150 K and $P_{gas} = 6.08 \times 10^8$ K $cm^{-3}$. The energy units of $\Delta G°$ are given in kcal $mol^{-1}$.

**Table 9.** Computed electronic enthalpies of excitation ($\Delta H°_{exc}$).

| Excited state reaction | kcal $mol^{-1}$ | eV |
|---|---|---|
| $\cdot CH_2(^3B_1) \rightarrow CH_2(^1A_1)$ | 8.87 | 0.39 |
| $\cdot O_2(^3\Sigma g^-) \rightarrow O_2(^1\Delta g)$ | 29.13 | 1.26 |
| $\cdot O_I(^3P_2) \rightarrow O_I(^1D)$ | 49.79 | 2.16 |
| $\cdot OH(^2\Pi) \rightarrow \cdot OH(^4\Pi)$ | 101.39 | 4.39 |
| $CO(^1\Sigma^+) \rightarrow \cdot CO(^3\Pi)$ | 138.65 | 6.01 |
| $H_2(^1\Sigma g^+) \rightarrow \cdot H_2(^3\Sigma)$ | 191.84 | 8.32 |

**Notes.** This table shows the entalphy of excitation from detected ground-state chemical species to their related excited electronic state part of Tables 3, 5 and 7. The values were calculated at CCSD(T)-F12/cc-pVTZ-F12 with corrections for ZPE, at a temperature range of 13.2–150 K and pressures between $2.29 \times 10^7$–$6.90 \times 10^3$ K $cm^{-3}$. The entalphy units are presented in kcal $mol^{-1}$ and in eV (this last only as a reference).

– v. $\cdot OH$ excited radicals form on ice-grain surfaces after applying a high-energy photonic radiation of 2 MeV, as empirically demonstrated (Miyazaki et al. 1993). However,

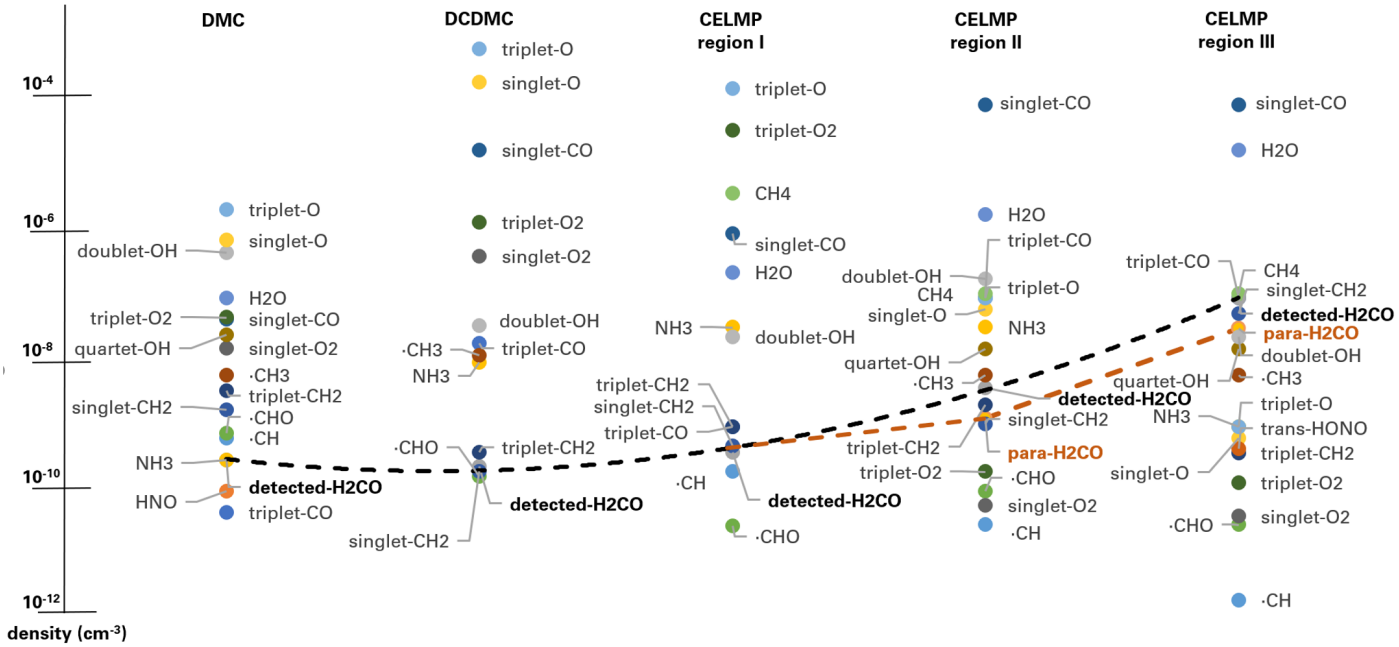


**Fig. 4.** Abundances of reactants, detected $H_2CO$ (dotted black line), and gas-phase para-$H_2CO$ (dotted orange line) (in $cm^{-3}$) in the three studied regions of IRAS 16293. The reactions composed of reactants above the orange dotted line might be the main contributors to para-$H_2CO$ production.

this is an unlikely event to occur inside dense clouds and in envelopes beyond the CO snow line (<20 K), which is mainly reserved for interactions with small fractions of highly energetic CRs. In this way, an ·OH($^4\Pi$) column density of $8 \times 10^{15}$ $cm^{-2}$, as determined by Goldman et al. (1981), was applied for the three regions left (DMC, IRAS 16293 regions II and III).

– vi. Many of the transitions from diatomic singlet ground-state hydrogen leading to triplet excited states mainly correspond to forbidden electronic transitions. However, some laboratory experiments have reported a dominance of triplet electronic states after intense photonic radiation in the 20–100 eV (Aguilar et al. 2008) or 15.1–16.7 eV (Jungen & Glass-Maujean 2016) ranges. This enables the existence of metastable triplet hydrogen in space after photon absorption by the singlet ground-state. Nevertheless, and as already mentioned, this is a rare event to occur in cold regions of the ISM and negatively impacts their abundances. We no longer consider triplet $H_2$ here.

In Fig. 4, the final distribution (abundances) of reagents in cold regions of the ISM of all molecular species that were part of the reactions of these computations have returned as valid in the cold regions of the ISM. In this figure, the dotted black $H_2CO$ line represents the total formaldehyde detected by radio-astronomers, while the dotted orange line represents to para-$H_2CO$ formed in the gas-phase as determined by Ceccarelli et al. (2000) and (2001). The prequalified reactions to produce $H_2CO$ in every astronomic environment are analyzed below, together with their corresponding PES profiles.

### 4.5. Potential energy profiles of prequalified reactions

In order to focus on the energy discussion, the following conventions and their respective units (if any) and signs are applicable:

– a) For reactions with PES coordinates submerged below the reference reactant energies, a minimum in a PES profile corresponds to a maximum in energy required to dissociate the chemical compound.
– b) As the energy released in an early-downhill surface from reactants to intermediates is given in the form of kinetic energy (all prequalified reactions are exothermic and exergonic), the change in enthalpy among them ($-\Delta H^\circ$) is employed, and the units used are kcal $mol^{-1}$.
– c) For the energetically easiest passage from reactants (or intermediates) to products through a saddle point on PES, the Gibbs free-energy of activation ($\Delta^\ddagger G^\circ$) was used, and the units, as in the previous case, will be kcal $mol^{-1}$.
– d) An "inner" transition state is one whose energy at the saddle point is greater in magnitude (submerged) than the energy of the reactants that constitute the input channel. For an "outer" transition state, the concept is the opposite (emerged energy; see item a). The energy considered is the difference between the molecular enthalpy of the transition state and the input channel reactants. The units are kcal $mol^{-1}$ (eV only as an astrophysical reference).
– e) For the inner transition state, (or from reactants to products in a direct reaction), in which the energy is submerged (see item d)) with respect to the reactants energy, the enthalpy difference among them was used. The units are given in kcal $mol^{-1}$.

In accordance with the previous discussion, the following six direct barrierless reactions were initially studied:

– R4- $\cdot^3CO + {}^1H_2 \rightarrow {}^1H_2CO$
– R20- ${}^1CH_2 + O({}^1D) \rightarrow {}^1H_2CO$
– R21- ${}^1CH_2 + \cdot O({}^3P) \rightarrow {}^1H_2CO$
– R22- $\cdot^3CH_2 + O({}^1D) \rightarrow {}^1H_2CO$
– R29- ${}^1CH_2 + \cdot^4OH \rightarrow {}^1H_2CO + \cdot H$
– R73- $\cdot CHO + \cdot^4OH \rightarrow {}^1H_2CO + \cdot O({}^3P)$
– R24- ${}^1CH_2 + {}^1O_2 \rightarrow {}^1H_2CO + O({}^1D)$

Even though these reactions are likely going to progress in the three astrophysical objects studied, reactions R4, R20, R21, and R22 respond to radiative association (RA) processes. Consequently, they will proceed to form products but will be slower than reactions that trigger a leaving group from a kinetic point of view, even if they possess submerged transition states. The most efficient path that we computationally found for R4 is

**Table 10.** Thermodynamic function values of prequalified reactions with their inner transition state per astrophysical scenario (AS).

| AS/(R/id) | Reaction | Submerged energy of intermediates[a] | | | | | Inner TS energy of activation[b] | | | | Submerged TS energy[c] | | | | | |
|---|---|---|---|---|---|---|---|---|---|---|---|---|---|---|---|---|
| | | $\Delta G°$ | | $\Delta H°$ | | $\Delta S°$ | $\Delta^{\ddagger}G$ | | $\Delta^{\ddagger}H$ | | $\Delta G°$ | | | $\Delta H°$ | | |
| | | kcal mol$^{-1}$ | eV | kcal mol$^{-1}$ | eV | cal mol$^{-1}$ K$^{-1}$ | kcal mol$^{-1}$ | eV | kcal mol$^{-1}$ | eV | kcal mol$^{-1}$ | eV | %[d] | kcal mol$^{-1}$ | eV | %[d] |
| DMC | | | | | | | | | | | | | | | | |
| R27 | $^1CH_2 + {}^{\cdot 3}O_2 \rightarrow {}^1H_2CO + {}^3O(\cdot)$ | −39.47 | −1.71 | −45.01 | −1.95 | −55.42 | 3.77 | 0.16 | 3.82 | 0.17 | −35.70 | −1.55 | 90.46% | −41.19 | −1.79 | 91.51% |
| R28 | $^3CH_2 + {}^{\cdot 3}O_2 \rightarrow {}^1H_2CO + {}^3O(\cdot)$ | −30.45 | −1.32 | −36.14 | −1.57 | −56.87 | 3.77 | 0.16 | 3.82 | 0.17 | −26.69 | −1.16 | 87.63% | −32.32 | −1.40 | 89.43% |
| R30 | $^1CH_2 + {}^{\cdot 2}OH \rightarrow {}^1H_2CO + \cdot H$ | −108.22 | −4.69 | −113.64 | −4.93 | −54.14 | 37.87 | 1.64 | 38.07 | 1.65 | −70.35 | −3.05 | 65.00% | −75.56 | −3.28 | 66.50% |
| R33 | $^3CH_2 + {}^{\cdot 2}OH \rightarrow {}^1H_2CO + \cdot H$ | −99.21 | −4.30 | −104.76 | −4.54 | −55.58 | 37.87 | 1.64 | 38.07 | 1.65 | −61.33 | −2.66 | 61.82% | −66.69 | −2.89 | 63.66% |
| R44 | $\cdot CH_3 + O(^1D) \rightarrow {}^1H_2CO + \cdot H$ | −132.98 | −5.77 | −137.84 | −5.98 | −48.53 | 22.38 | 0.97 | 22.44 | 0.97 | −110.60 | −4.80 | 83.17% | −115.39 | −5.00 | 83.72% |
| R45 | $\cdot CH_3 + O(^3P) \rightarrow {}^1H_2CO + \cdot H$ | −82.97 | −3.60 | −88.04 | −3.82 | −50.71 | 22.37 | 0.97 | 22.44 | 0.97 | −60.60 | −2.63 | 73.03% | −65.60 | −2.84 | 74.51% |
| R46 | $\cdot CH_3 + {}^{\cdot 4}OH \rightarrow {}^1H_2CO + {}^1H_2$ | −185.35 | −8.04 | −191.73 | −8.31 | −63.71 | 90.01 | 3.90 | 90.00 | 3.90 | −95.34 | −4.13 | 51.44% | −101.73 | −4.41 | 53.06% |
| R53 | $\cdot CH_3 + {}^1O_2 \rightarrow {}^1H_2CO + {}^{\cdot 2}OH$ | −55.09 | −2.39 | −60.04 | −2.60 | −33.02 | 44.13 | 1.91 | 44.02 | 1.91 | −10.96 | −0.48 | 19.90% | −16.03 | −0.69 | 26.69% |
| R82 | $\cdot CHO + \cdot CHO \rightarrow {}^1H_2CO + {}^1CO$ | −63.30 | −2.74 | −69.76 | −3.02 | −64.61 | 55.18 | 2.39 | 55.15 | 2.39 | −8.11 | −0.35 | 12.82% | −14.61 | −0.63 | 20.95% |
| DCDMC | | | | | | | | | | | | | | | | |
| R28 | $^3CH_2 + {}^{\cdot 3}O_2 \rightarrow {}^1H_2CO + {}^3O(\cdot)$ | −35.12 | −1.52 | −35.64 | −1.55 | −38.88 | 3.79 | 0.16 | 3.80 | 0.16 | −31.33 | −1.36 | 89.20% | −31.84 | −1.38 | 89.34% |
| R33 | $^3CH_2 + {}^{\cdot 2}OH \rightarrow {}^1H_2CO + \cdot H$ | −103.67 | −4.50 | −104.16 | −4.52 | −37.48 | 37.96 | 1.65 | 37.97 | 1.65 | −65.71 | −2.85 | 63.38% | −66.20 | −2.87 | 63.55% |
| R44 | $\cdot CH_3 + O(^1D) \rightarrow {}^1H_2CO + \cdot H$ | −136.95 | −5.94 | −137.40 | −5.96 | −34.40 | 22.42 | 0.97 | 22.43 | 0.97 | −114.53 | −4.97 | 83.63% | −114.98 | −4.99 | 83.68% |
| R45 | $\cdot CH_3 + O(^3P) \rightarrow {}^1H_2CO + \cdot H$ | −87.13 | −3.78 | −87.61 | −3.80 | −36.59 | 22.42 | 0.97 | 22.42 | 0.97 | −64.71 | −2.81 | 74.27% | −65.19 | −2.83 | 74.41% |
| R53 | $\cdot CH_3 + {}^1O_2 \rightarrow {}^1H_2CO + {}^{\cdot 2}OH$ | −58.91 | −2.56 | −59.39 | −2.58 | −36.55 | 44.08 | 1.91 | 44.08 | 1.91 | −14.83 | −0.64 | 25.14% | −15.31 | −0.66 | 25.74% |
| CELMP | region I | | | | | | | | | | | | | | | |
| R27 | $^1CH_2 + {}^{\cdot 3}O_2 \rightarrow {}^1H_2CO + {}^3O(\cdot)$ | −43.98 | −1.91 | −44.55 | −1.93 | −28.26 | 3.79 | 0.16 | 3.80 | 0.16 | −40.19 | −1.74 | 91.38% | −40.75 | −1.77 | 91.48% |
| R28 | $^3CH_2 + {}^{\cdot 3}O_2 \rightarrow {}^1H_2CO + {}^3O(\cdot)$ | −35.08 | −1.52 | −35.68 | −1.55 | −29.71 | 3.79 | 0.16 | 3.80 | 0.16 | −31.29 | −1.36 | 89.19% | −31.88 | −1.38 | 89.36% |
| R30 | $^1CH_2 + {}^{\cdot 2}OH \rightarrow {}^1H_2CO + \cdot H$ | −112.54 | −4.88 | −113.08 | −4.90 | −26.86 | 37.96 | 1.65 | 37.97 | 1.65 | −74.58 | −3.23 | 66.27% | −75.12 | −3.26 | 66.43% |
| R33 | $^3CH_2 + {}^{\cdot 2}OH \rightarrow {}^1H_2CO + \cdot H$ | −103.64 | −4.49 | −104.21 | −4.52 | −28.31 | 37.96 | 1.65 | 37.97 | 1.65 | −65.68 | −2.85 | 63.37% | −66.24 | −2.87 | 63.57% |
| region II | | | | | | | | | | | | | | | | |
| R33 | $^3CH_2 + {}^{\cdot 2}OH \rightarrow {}^1H_2CO + \cdot H$ | −101.77 | −4.41 | −104.63 | −4.54 | −35.71 | 37.91 | 1.64 | 38.04 | 1.65 | −63.86 | −2.77 | 62.75% | −66.59 | −2.89 | 63.65% |
| R44 | $\cdot CH_3 + O(^1D) \rightarrow {}^1H_2CO + \cdot H$ | −135.41 | −5.87 | −137.74 | −5.97 | −29.06 | 22.39 | 0.97 | 22.43 | 0.97 | −113.02 | −4.90 | 83.46% | −115.30 | −5.00 | 83.71% |
| R45 | $\cdot CH_3 + O(^3P) \rightarrow {}^1H_2CO + \cdot H$ | −85.44 | −3.70 | −87.94 | −3.81 | −31.24 | 22.39 | 0.97 | 22.43 | 0.97 | −63.06 | −2.73 | 73.80% | −65.52 | −2.84 | 74.50% |
| R46 | $\cdot CH_3 + {}^{\cdot 4}OH \rightarrow {}^1H_2CO + {}^1H_2$ | −188.08 | −8.16 | −191.56 | −8.31 | −43.49 | 90.01 | 3.90 | 90.01 | 3.90 | −98.07 | −4.25 | 52.14% | −101.55 | −4.40 | 53.01% |
| R92 | $O(^3P) + CH_4 \rightarrow {}^1H_2CO + {}^1H_2$ | −85.05 | −3.69 | −87.38 | −3.79 | −29.22 | 88.18 | 3.82 | 88.19 | 3.82 | 3.14 | 0.14 | −3.69% | 0.81 | 0.04 | −0.93% |
| region III | | | | | | | | | | | | | | | | |
| R30 | $^1CH_2 + {}^{\cdot 2}OH \rightarrow {}^1H_2CO + \cdot H$ | −108.84 | −4.72 | −113.96 | −4.94 | −34.14 | 37.76 | 1.64 | 38.15 | 1.65 | −71.08 | −3.08 | 65.31% | −75.81 | −3.29 | 66.52% |
| R31 | $^1CH_2 + CO_2 \rightarrow {}^1H_2CO + {}^1CO$ | −42.50 | −1.84 | −48.27 | −2.09 | −38.44 | 27.39 | 1.19 | 27.52 | 1.19 | −15.11 | −0.66 | 35.56% | −20.75 | −0.90 | 42.99% |
| R45 | $\cdot CH_3 + O(^3P) \rightarrow {}^1H_2CO + \cdot H$ | −83.78 | −3.63 | −88.30 | −3.83 | −30.16 | 22.33 | 0.97 | 22.51 | 0.98 | −61.45 | −2.66 | 73.35% | −65.79 | −2.85 | 74.51% |
| R46 | $\cdot CH_3 + {}^{\cdot 4}OH \rightarrow {}^1H_2CO + {}^1H_2$ | −185.47 | −8.04 | −192.13 | −8.33 | −44.40 | 90.03 | 3.90 | 89.96 | 3.90 | −95.45 | −4.14 | 51.46% | −102.18 | −4.43 | 53.18% |
| R92 | $O(^3P) + CH_4 \rightarrow {}^1H_2CO + {}^1H_2$ | −83.53 | −3.62 | −87.71 | −3.80 | −27.90 | 88.18 | 3.82 | 88.18 | 3.82 | 4.65 | 0.20 | −5.57% | 0.46 | 0.02 | −0.53% |

**Notes.** The presented values were calculated by the CCSD(T)-F12/cc-pVTZ-F12 level of theory and basis set and include ZPE corrections. [a]Submerged energy of intermediates with respect to the reactants energy. [b]Energy of activation from the respective submerged intermediate energy. [c]Value of the TS submerged energy with respect to the reactants energy. [d]Relative submersion (c/a) in percent.

through two consecutive downhill steps, forming the formaldehyde triplet as an intermediate ($\cdot^3CO + {}^1H_2 \rightarrow {}^3H_2CO + h\nu_1 \rightarrow {}^1H_2CO + h\nu_2$). In the first stage of the reaction, an average enthalpy (range 13.2–150 K) of −64 kcal mol$^{-1}$, calculated at CCSD(T)-F12/cc-pVTZ-F12, is emitted. In the second reaction step, and to establish singlet $H_2CO$ from an excited triplet-state, an energy of −72 kcal mol$^{-1}$ is reached. As a reference, the total average submerged energy computed for products from reactants for the cold regions is −137 kcal mol$^{-1}$. Because R20, R21, and R22 are composed of a methylene group and atomic oxygen but are in different electronic states (see text above), different PES profiles from each other and differences in their yielded and increased energy are expected. R20 is an electronically adiabatic reaction with just one downhill step, which reaches an averaged submerged energy of −236 kcal mol$^{-1}$ for the three regions we studied. However, the triplet reactions R21 and R22 can form singlet $H_2CO$ in two steps. Triplet formaldehyde again appears as the easiest way to pass from reactants to products in both reactions. In the first downhill step, R21 generates an additional averaged energy of −114 kcal mol$^{-1}$, but in the case of R22, −155 kcal mol$^{-1}$ is obtained. R21 and R22 complete their pathway from triplet to singlet $H_2CO$, increasing their energy initially up to −72.34 kcal mol$^{-1}$ (as in R4). The total averaged sunken enthalpy has a value of −186 kcal mol$^{-1}$ for R21 and −227 kcal mol$^{-1}$ for R22. Regarding R29, the computations return two downhill steps in the process of forming $H_2CO$. In the first down course, an average enthalpy of −71 kcal mol$^{-1}$ (just at the limit of UV and UVA radiation) is released forming a planar doublet radical intermediate. This intermediate detaches one hydrogen to reach the more stable $H_2CO$ + H form, spending an average −185.91 kcal mol$^{-1}$ in cold regions. In the process a spin-flip must take place, which will likely slow down the molecular formation velocity. Finally, R73 flows directly in one step from $\cdot CHO + {}^4OH$ to singlet formaldehyde, but it could be suggested or thought that there should be two transitions states. In the process and as a result of breaking $\cdot OH(^4\Pi)$ little bonds forming $CHO + H + O + e^+ \rightarrow H_2CO\ (^1A_1) + H + e^-$, detailed calculations returned convergence in one step, suggesting that the two processes could proceed simultaneously. Again, the energy data for these reactions are from our CCSD(T)-F12/cc-pVTZ-F12 calculations, which incorporate ZPE corrections. Detailed PES profiles of direct barrier-less reactions are available in

Appendix B.1. In addition, the computationally calculated harmonic infrared-band positions, individual molecular and ZPE energies, as well as their spatial coordinates for the main excited species at the CCSD(T)-F12/cc-pVTZ level of theory and basis set are listed in Appendix C.1.

### 4.6. Prequalified reactions with inner transition states

In a pure gas-phase reaction process and as a general description of reactions containing submerged transition state energy with respect to the reactant's energy, entrance channels occur over PESs without barriers to overcome. However, this entry is featured (bounded) by radial and angular anisotropies that may be generated as result of the energies. For the most favored reactions this work, the most relevant radial and angular energies of interaction were computed, and will be shown in the following. Most reactions commonly start to descend into an initial associated complex valley, known as early-downhill surfaces, to directly form an intermediate molecular complex (as mentioned) without entrance barriers. This feature over an attractive PES releases energy (see Table 10) that is generated by the rearrangement of the atoms after the approach of their center of mass. When the related forces between them continue in the appropriate direction, a substantial decrease in the atomic distances will affect their electronic, vibrational, rotational, and translational energy. This excess of energy will accompany the reaction in the form of kinetic energy along the reaction pathway, being the most favored reactions these that require the least amount of energy to proceed to the products. In addition, Table 10 presents (i) the potentially qualified reactions to produce $H_2CO$ in the regions of cold space, and (ii) their relative energies after reactions have progressed through their PES to form the products. Additionally, in order to study their respective energy profiles in detail, we present the Gibbs free-energy computed at the CCSD(T)-F12/cc-pVTZ-F12 level of theory and basis sets under the astrophysical conditions of DMCs and DCDMCs (corrected for ZPE), in Fig. 5. Following these two rules, the most favored reactions are R27 and R28 (methylene and $^3O_2$ based reactions) in DMCs, followed by R44 and R45 (methyl radical and atomic oxygen), and R30 and R33 (methylene with hydroxyl radical). In this way, R46 despite its great exothermicity, is relegated to a less favorable position due to its high internal barrier. R53 and R82 are also not as likely due to a combination of both factors.

R27 ($^1CH_2 + {\cdot}^3O_2 \rightarrow {}^1H_2CO + {\cdot}O(^3P)$) and R28 (${\cdot}^3CH_2 + {\cdot}^3O_2 \rightarrow {}^1H_2CO + {\cdot}O(^3P)$) involve two electronic states of methylene, (ground-state -$X^3B_1$- and singlet-excited state -$a^1A_1$-), combined with molecular oxygen in its triplet ground-state ($^3P$). The reaction starts to descend into an initial downhill surface to form a molecular Criegee intermediate (CI) complex, known as carbonyl oxide, in its triplet electronic state ($^3H_2COO$). Independent of the initial trajectory followed by reactants, the entrance channel belonging to $^1CH_2 + {\cdot}^3O_2$ is established when the relative energy of interaction ($E_{int}$) between the products and the intermediate are equalized radially and angularly. To determine more details about the entrance process, the radial and angular energies of interaction ($E_{int}$) were computed at the CCSD(T)-F12/cc-pVTZ-F12, in steps of 0.1 Å for radial and 10° for angular anisotropies. The complete results are presented in Fig. 6. Such information will provide some kinetic insights beyond the thermodynamics described thus far. This figure represents four different approaches of triplet molecular oxygen over two excited electronic states of methylene. Radially (along the C–O molecular bond) and as expected, the possible association of both channels initiates at different distances (R) about 1.90 Å in R28, while for R27, the association starts around 4.8 Å (beyond the graphic range, see Fig. 6-(1)). The radial interaction in R27 is dominated by dispersion forces (more so than in R28) that are due to the perturbative interactions produced by the excited spin-orbit of the $CH_2$ singlet. As the molecules approach each other radially, the energy gradually increases through the attractive zone until the energetic equilibrium is reached (upright blue bar in Fig. 6-(1)). This point is located in both channels at $R$ = 1.38 Å, producing a at minimum −51.27 kcal mol$^{-1}$ for R27 and −41.98 mol$^{-1}$ for R28. The new bond that is created has a harmonic stretching frequency ($\omega_5$ - A) of 1044 cm$^{-1}$ (calculated at CCSD(T)-F12/cc-pVTZ-F12) after $^3H_2COO$ is formed. Angular interactions have different approaches and provide clues about where geometrical entry bounds might be spatially located, Fig. 6-(2), (3), and (4). When O = O accesses vertically (see Fig. 6–(2$\alpha$)) with the right angle (108.48°), a wide asymmetric entry angle between ≈−140° and +100° in R27 is exhibited, which is slightly narrower at ≈−120° and +80° in R28. In both cases, this orientation is wide enough to facilitate an intermediate formation. In contrast, if O = O horizontally joins Fig. 6-(2-$\beta$) with the same angle, the access is restricted to ≈±50° in R27 and to ≈±40° in R28. This orientation becomes the most probable entrance bottleneck for reactants. Another option appears if molecular oxygen approaches carbon (atom) angularly with the same C-O-O angle (108.48°). The anisotropies of this anisotropy are shown in Fig. 6-(3)-, suggesting that in R27 an angle between −40° and +190° maintains this possibility. It is most favored in the regions centered at ≈ 0° and 140°. In this approach, the access for R28 is reduced to a zone between ≈ 58° and 88° (see Fig. 6-(3), orange curve). Finally, the possibility that molecular oxygen tangentially accesses the complex is considered, with a tilted angle of ≈108.48° confirming the anisotropies exposed in Fig. 6-(4) as a possible cone-shaped input trajectory. Surprisingly, the access to the complex is restricted in certain regions of the cone, more specifically in an angle between ≈90° to 135° and ≈ −90° to −135°, as shown in Fig. 6-(4). Continuing the reaction path along the PES, R27 confirms an electronically adiabatic reaction that flows over triplet electronic states on all molecular associations that appear during the transit from reactants to products. The initial fall releases an enthalpic energy of about −45.01 kcal mol$^{-1}$ in this environment. This energy is enough to overcome the low free-energy barrier belonging to its inner transition state (3.77 kcal mol$^{-1}$), which in addition is submerged by −41.19 kcal mol$^{-1}$ with respect to the products energy. The exit channel from $H_2COO$ in the route the $H_2CO + O(^3P)$ PES valley is conformed by the dissociation of the (O–O) bond, constrained along an imaginary vibrational mode that is calculated to be 552.8i cm$^{-1}$. This reaches the stationary point at 1.34 Å from the oxygen attached to C. On the other hand, R28 has a similar PES profile as R27. They differ in energy values because both reactants in R28 are in the ground-state, forming an initial quintet complex that is more energetic (see Table 10) than the reactant complex compared to R27. This produces an initial first downhill enthalpic step in R28 of -36.14 kcal mol$^{-1}$, which means a difference of 9.02 kcal mol$^{-1}$ compared with the initial reaction step of R27. The remaining reaction path follows the same course as R27. Kinetically, both reactions have been studied for a long time because formaldehyde is important in atmospheric hydrocarbon combustion chemistry. For R27, a rate constant of $5 \times 10^{-11}$ cm$^3$ mol$^{-1}$ s$^{-1}$ (Tsang & Hampson 1986), and $0.93 \pm 0.22 \times 10^{-12}$ cm$^3$ mol$^{-1}$ s$^{-1}$ (Lakshmanan et al. 2019) have been defined. For R28, a rate of $3.2 \pm 0.3 \times 10^{-12}$ cm$^3$ mol$^{-1}$ s$^{-1}$ (e.g., Böhland et al.

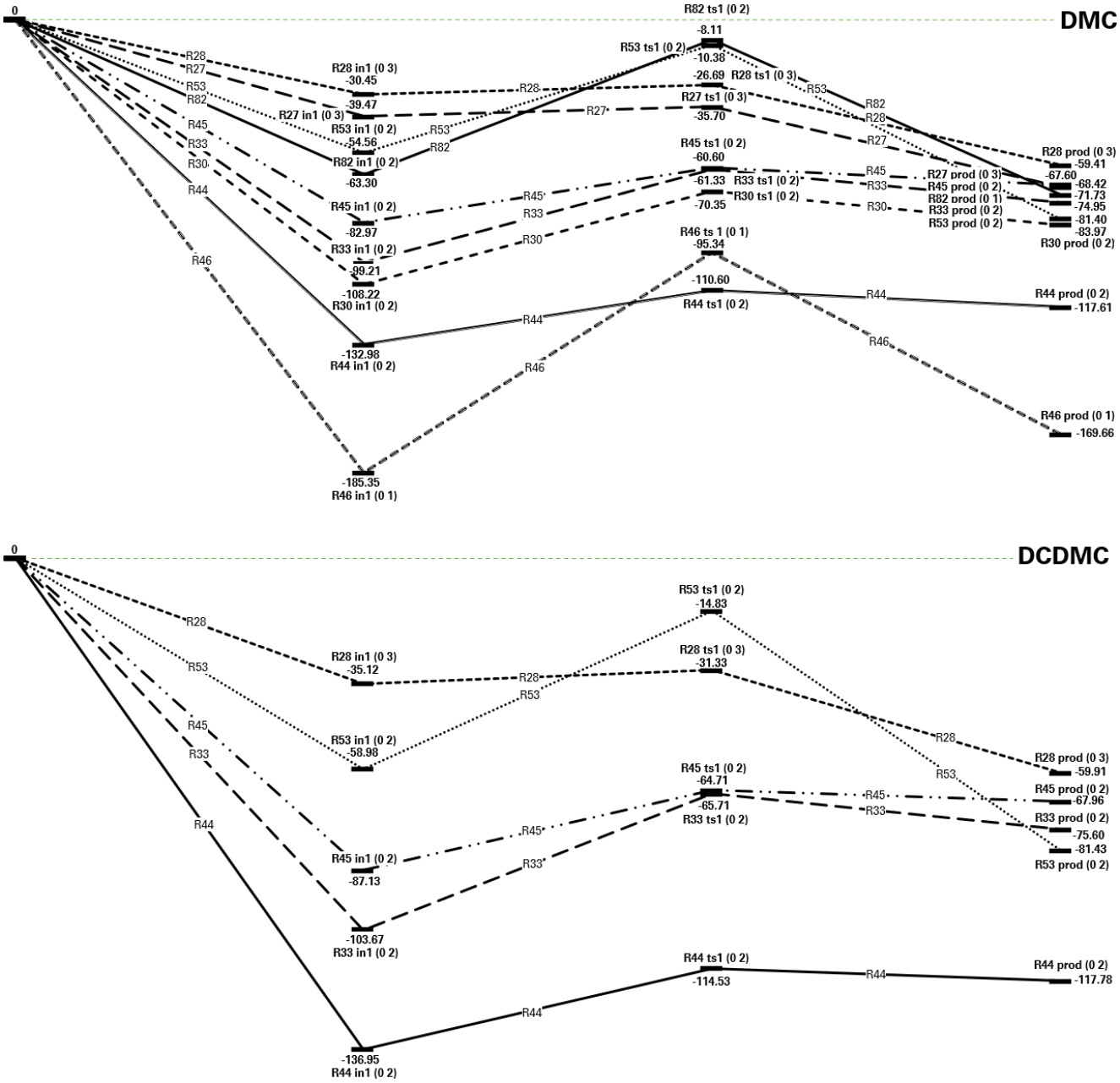


**Fig. 5.** Gibbs free-energy profiles (kcal $mol^{-1}$) of prequalified reactions under DMC and DCDMC astrophysical conditions ($T_{gas}$ = 100 K, $P_{gas}$ = $6.90 \times 10^3$ K $cm^{-3}$ and $T_{gas}$ = 13.2 K, $P_{gas}$ = $5.30 \times 10^4$ K $cm^{-3}$ respectively). Energy values are obtained at CCSD(T)-F12/cc-pVTZ-F12 with the respective corrections for ZPE. In parenthesis we plotted charge and spin multiplicity.

1984; Darwin et al. 1989; Bley et al. 1992; Baulch et al. 1992) and more recently, $0.98 \pm 0.28 \times 10^{-12}$ $cm^3$ $mol^{-1}$ $s^{-1}$ (Lakshmanan et al. 2019) have been determined at close to room conditions. These figures confirm in any case that R27 is favored with respect to the ground-state of R28 in the formation pathway to $H_2CO$ + $O(^3P)$. This is in line with what the thermodynamic profiles and entrance channel anisotropies indicate.

As in the previous case, the two channels R44 ($\cdot CH_3$ + $O(^1D) \rightarrow {}^1H_2CO$ + ·H; radical-excite) and R45 ($\cdot CH_3$ + $\cdot O(^3P) \rightarrow {}^1H_2CO$ + ·H; radical-radical) are characterized by a molecular junction without any entrance potential barrier. Radial anisotropies (see Fig. 7-(1)) indicate that the most probable entry along (R) for R44 is located at a distance of ≈4.1 Å, which differs from the entry calculated for R45, which is determined to be ≈2.5 Å. This interaction, also present in R27 and R28, is also dominated by dispersion forces. These forces will alter the radial trajectory between atomic oxygen and methyl radical in particular, in R44. From an angular entrance, the vertical and horizontal anisotropies show perturbations along the entry pathways (see Fig. 7), where limits of the trajectory are also governed by dispersion interactions, led by electron densities (H) as well as by rotational, vibrational, and translational dynamics. However, vertical-radial pathways in Fig. 7-(2) are defined by an angle of entry between ≈ −70° to +80° for R44 and −70° to +70° for R45. Their asymmetries are in the upper approach (H-interactions in $\alpha$ curves). On the other hand, horizontal-radial motions ($\beta$ curves in Fig. 7-(2)) are conformed between ≈ −90° to +90° for R44 and ≈ −80° to +80°for R45, but maintain the symmetry of the

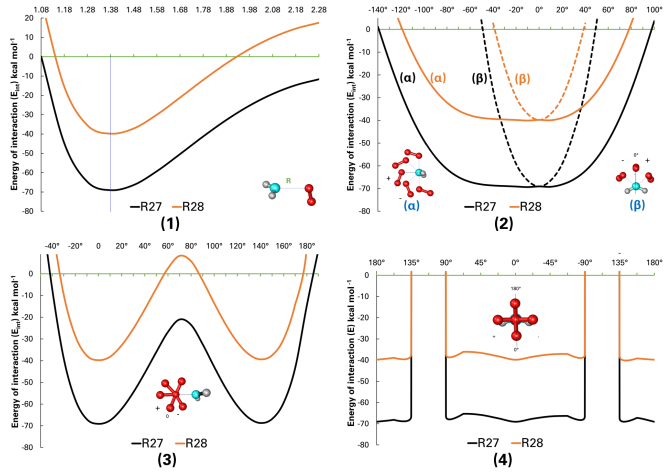


**Fig. 6.** Radial (1) and angular (2), (3), and (4) interaction energy diagrams ($E_{int}$) of R27 (black) and R28 (orange) entrance channels. (1) Upright blue bar represent $R$ at the equilibrium. (2) Dotted lines illustrates the entrance energy curve of the angular $\beta$ anisotropies. Molecular energies were calculated at CCSD(T)-F12/cc-pVTZ-F12, units in kcal mol$^{-1}$, angles in sexagesimal degrees, and molecular distances in Å.

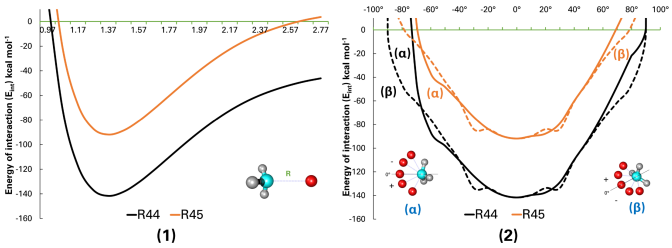


**Fig. 7.** Radial (1) and angular (2) energy of interaction diagrams ($E_{int}$) belonging to R44 and R45 entrance channels. $E_{int}$ = Molecular energy of intermediate ($E_2$) – molecular energy of reagents ($E_1$). Molecular energies ($E_2$ & $E_1$) calculated at CCSD(T)-F12/cc-pVTZ-F12 level of theory and basis sets, units in kcal mol$^{-1}$, angles in sexagesimal degrees, and molecular distances in Å.

$\beta$ curves and widen the angular range of access to the molecule. The energy used in the downhill portion to form methoxy radical ($CH_3O$) and the difference in the internal energy of ($O_2(^3P)$ vs. $O_2(^1D)$) produces a more pronounced initial enthalpy drop in R44 compared to R45 (−137.84 kcal mol$^{-1}$ vs. −88.04 kcal mol$^{-1}$ in DMCs). This is in favor of R44 (see Fig. 10). A proposed exit channel to produce $H_2CO$ + H must be determined from the C atom, assuming that in practice, there are three potential TSs (one per H) that statistically can be involved in the process. In this way, and in accordance with the previous intermediate energy, the transition state in R44 is submerged −115.39 kcal mol$^{-1}$ or (−5.00 eV), below the reactant's enthalpy; R45 is −65.60 kcal mol$^{-1}$ or −2.84 eV, having a moderately submerged free-energy barrier to overcome of 22.37 kcal mol$^{-1}$ under DMC condition (see Table 10 for more details and scenarios). The exit channel flows over a stationary point located along a H–C bond that is constituted by an imaginary frequency of 481.81i cm$^{-1}$, which requires only 16.28% of the enthalpy released in the case of R44 and 25.49% in R45 to form the products. One of these two reactions has been kinetically studied, with rate coefficients that were obtained under normal atmospheric conditions of ∼1 × 10$^{-10}$ cm$^3$ mol$^{-1}$ for R44 (Atkinson et al. (2006) and references therein). No coefficient rates for R45 appear to be listed in astrochemical databases such as KIDA, UMIST, or NIST.

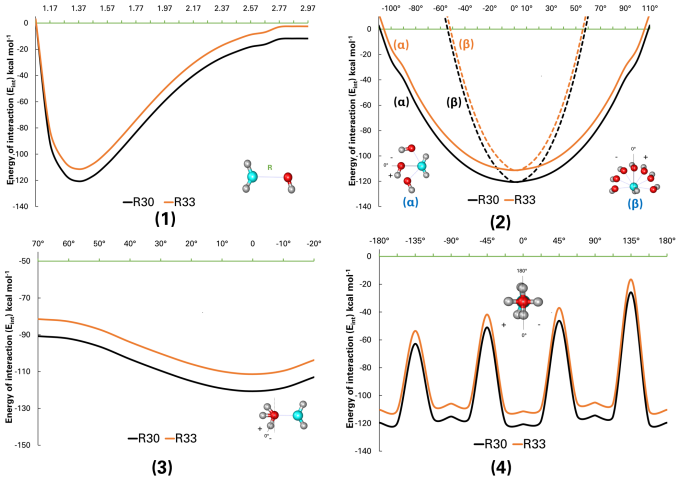


**Fig. 8.** Radial (1) and angular (2), (3), and (4) energy of interaction diagrams ($E_{int}$) belonging to the R30 and R33 entrance channels. $E_{int}$ = Molecular energy of intermediate ($E_2$) - molecular energy of reagents ($E_1$). Molecular energies ($E_2$ and $E_1$) calculated at CCSD(T)-F12/cc-pVTZ-F12, units in kcal mol$^{-1}$, angles in sexagesimal degrees, and molecular distances in Å.

R30 corresponds to an excited-radical reaction, while R33 represents a radical-radical chemical interaction composed of $CH_2(a^1A_1)$ and $\cdot CH_2(X^3B_1)$ reagents, in addition to the doublet hydroxyl radical $\cdot OH(^2\Pi)$. This union produces an initial doublet and quartet set of reactants that in both cases form the hydroxymethyl radical ($CH_2OH$) as an intermediate. As a brief description of the possible entrance channels, when (intermolecular radial distance -R- Table 8(1)) $R > 3$ Å, radial interactions are characterized by the already mentioned dispersion forces that are more pronounced in excited-radical reaction R30. When the radial distance ($R$) between $^2$OH-C is ≈ 3 Å, the joining process behaves gradually and progressively. The energetic equilibrium is reached at a distance $R$ = 1.36 Å, acquiring a maximum energy (E) of −120.65 kcal mol$^{-1}$ for R30 and −111.37 mol$^{-1}$ for R33, as shown in Fig. 8-(1). The corresponding stretching vibrational harmonic mode belonging to the created intermediate ($\nu_4$ - A) is 1207 cm$^{-1}$ (calculated at CCSD(T)-F12/cc-pVTZ-F12). Vertical-angular interactions (Fig. 8-(2),(3), and (4)) demonstrate that the approach between ≈ ±110° enables molecular formation in this orientation, while horizontally angular access is limited to ≈ ±60° in R30. The horizontal and vertical molecular entrance energy difference for R33 in both cases is <10 kcal mol$^{-1}$ below R30, is the lowest variation of all molecular systems studied so far. If the $^2$OH path faces angularly the carbon atom (C belongs to $CH_2$), as is represented in Fig. 8-(3), the interaction will proceed satisfactorily because it presents a favored orientation with an angle of (108.98°). Finally, and as can be denoted by the anisotropies represented in Fig. 8-(4), the interactions show a less restrictive energy profile (compared to R27 and R28), where the most favored regions are those that lie alternatively between 45° centered at the 0° point of the truncated cone pathway. When the chemical union is realized, R30 produces an initial enthalpy in excess of −113.64 kcal mol$^{-1}$ and −104.76 kcal mol$^{-1}$ in R33 under astrophysical conditions such as those in DMCs. In order to complete the reaction to form $H_2CO$ + ·H, a Gibbs free-energy barrier to overcome of 38.07 kcal mol$^{-1}$ is required in both cases. However, this maximum on the PES is submerged enthalpically with respect to the reagents −75.56 kcal mol$^{-1}$ in R30 and −66.69 kcal mol$^{-1}$ in R33. This feature is in favor of

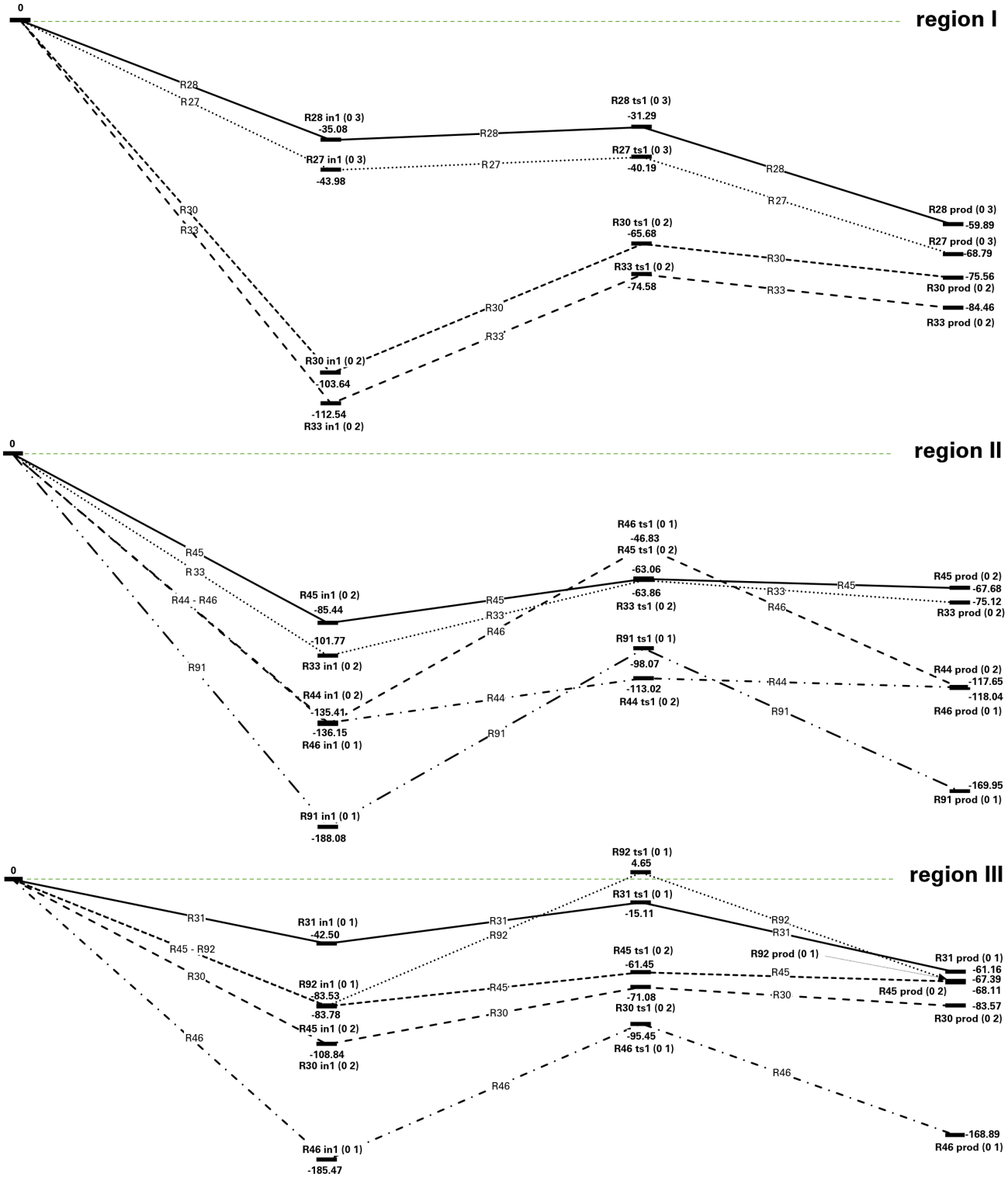


**Fig. 9.** Gibbs free-energy (kcal mol$^{-1}$) profiles of pre-qualified reactions for three regions of IRAS 16293 astrophysical conditions at CCSD(T)-F12/cc-pVTZ-F12 (corrections for ZPE incorporated). Region I: $T_{gas}$ = 20 K and $P_{gas}$ = 2.29 × 10$^7$ K cm$^{-3}$. Region II: . $T_{gas}$ = 80 K and $P_{gas}$ = 7.06 × 10$^7$ K cm$^{-3}$. Region III: $T_{gas}$ = 150 K and $P_{gas}$ = 6.08 × 10$^8$ K cm$^{-3}$. Energy units of $\Delta H°$, $\Delta G°$ in kcal mol$^{-1}$; $\Delta S°$ in cal mol$^{-1}$ K$^{-1}$. In parentheses, we plot the net charge and spin multiplicity.

R30. The exit channel is located along the H-O bond, which requires a Gibbs free-energy of activation of 37.9 kcal to pass over the transitory state to reach products on PES. This detachment is produced through the stretching vibrational mode ($\omega_9$ = 3861 cm$^{-1}$ - A) of hydroxymethyl radical ($CH_2OH$) generating a transition state characterized by an imaginary frequency of ts = −1092 cm$^{-1}$.

From a kinetic viewpoint, and as in previous cases, reactions based on triplet methylene and the hydroxyl radical doublet have been studied from an atmospheric combustion perspective. At

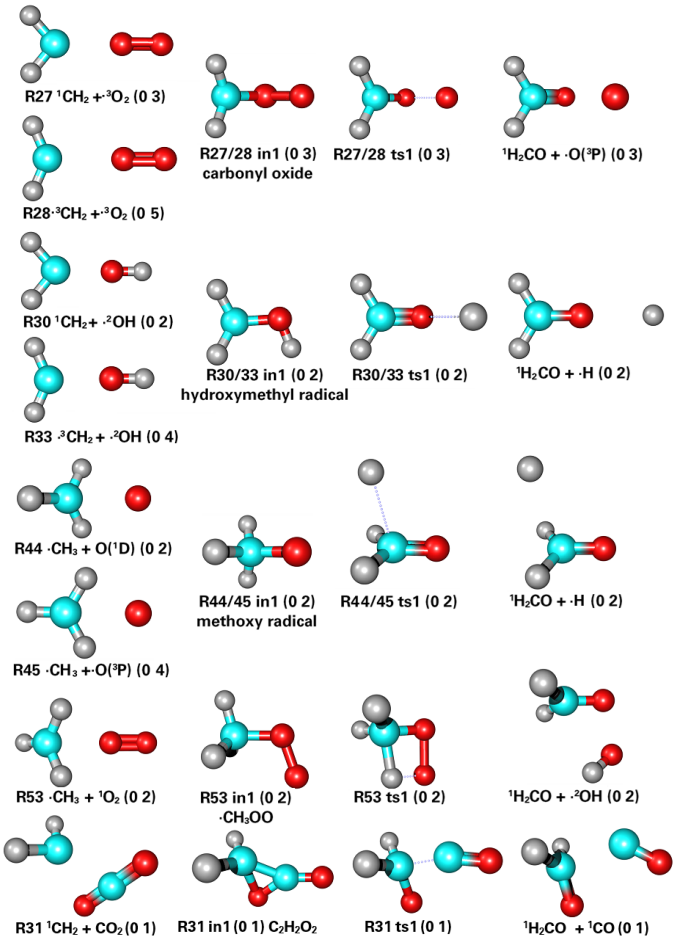


**Fig. 10.** Initial structures of reactants, intermediates, transition states (from IRC), and products of the most relevant reactions determined by this study. In parenthesis we plotted net charge, and spin multiplicity of the molecular complexes.

room conditions, a rate coefficient of $3.01 \times 10^{-11}$ cm$^3$ mol$^{-1}$ s$^{-1}$ was defined for R33 (Tsang & Hampson 1986; Jasper et al. 2007). Even though there are no published rates for R30, recent laboratory studies based on atmospheric conditions of TITAN by Douglas et al. (2018), indicate that the reactivity of $^1CH_2$ tends to increase with decreasing temperature, which could denote a positive factor for reactions R27, R30, or R31 under extremely cold conditions (<20 K). Examining the qualified reactions in DCDMCs (R28, R33, R44, R45 and R53), the presence of reagents with densities above $H_2CO$ (see Sects. 2 and 4.2) is notably reduced. The surrounding energy in DCDMCs, compared to DMCs and the lower number of collisions typical of this environment (see Sect. 2), is a crucial physical factor for determining the formation of new chemical compounds. In this environment, the relative detected abundances of $^1CH_2$, $^4$OH, and ·CHO are below those of formaldehyde. This means that the reactions that are composed of them are less relevant in $H_2CO$ formation. For energy profiles and details in DCDMC, we refer to Fig. 5, and for thermodynamic values to Table 10.

With respect to CELMPs, we present in Fig. 9, the Gibbs energy profiles for the most relevant reactions (defined in Table 10) for the three regions. IRAS 16293 is plotted for reference. In region I, R27, R28, R30 and R33 are presented as the most probable sources of $H_2CO$. In region II, R27 and R28 disappear, which leaves the already discussed reactions R33, R44, and R45. R46 and R91 enter this scenario as reactions to consider because of the abundances of $^4$OH and $CH_4$, respectively, but even though they possess inner barriers, the high free barriers (~90 kcal mol$^{-1}$) relegate them to the background. Region III is slightly more complex, because only $^1$CO, $^3$CO, $H_2O$, $CH_4$, and $^1CH_2$ exceed formaldehyde abundances. Five reactions (R30, R31, R45, R46, and R92) are proposed here as the main avenues responsible for the para-$H_2CO$ formation, but the last two (R46 and R92) continue with high barriers as in the previous region, despite an increasing temperature and pressure (see Table 10). At this point, reactions from Table1 might be considered based on $CH_4$ and $^1$CO ($CH_4 + {}^1CO \rightarrow {}^1H_2CO + {}^1CH_2$ and $CH_4 + {}^1CO \rightarrow {}^1H_2CO + {}^3CH_2$), but both cases show exergonic and exothermic behavior. However, reactions composed of methane and carbon monoxide, a) $CH_4 + {}^3CO \rightarrow H_2CO + {}^3CH_2$ and b) $CH_4 + {}^3CO \rightarrow H_2CO + {}^1CH_2$, are exothermic and exergonic under region III conditions, showing values of $\Delta H^\circ = -36.76$ kcal mol$^{-1}$, and $\Delta G^\circ = -37.60$ kcal mol$^{-1}$ for (a), and $\Delta H^\circ = -21.31$ kcal mol$^{-1}$, and $\Delta G^\circ = -21.93$ kcal mol$^{-1}$, for (b). To finalize this section, a new reaction is proposed for consideration. It is composed of singlet methylene and carbon dioxide. R31 ($^1CH_2 + CO_2 \rightarrow {}^1H_2CO + {}^1CO$; see the Gibbs free-energy profile in Fig. 9 and thermodynamic data in Table 10), has a moderate inner barrier of 27.39 kcal mol$^{-1}$ that is submerged enthalpically −20.75 kcal mol$^{-1}$ (−0.90 eV) below the reactants. According to Doty et al. (2004), $CO_2$ can be present in IRAS 16293 with a column density (N) of $1.5 \times 10^{-17}$ cm$^{-2}$ which represents a fractional abundance (n) compared to $H_2$ in this region of $\sim 2 \times 10^{-5}$ cm$^{-3}$, above $H_2CO$ abundance. If this density is confirmed ($CO_2$ has not been detected in this region yet), R31 may well be one of the most productive reactions to produce $H_2CO$ in region III of IRAS 16293 and similar environments. The structures, reactants, intermediates, transition states, and products of the most relevant reactions for the astrophysical scenarios studied are depicted in Fig. 10.

## 5. Conclusions and astrophysical implications

High-level ab initio quantum chemical computations (CCSD(T)-F12/cc-pVTZ-F12) applied to gas-phase molecular astrochemistry confirm that neutral $H_2CO$ in cold space at LTE conditions can be synthesized by a multi-channel system of reactions. Considering the relative abundance of reactants, the submersion and the internal barriers of inner transition states composed of three reaction paths and their thermodynamic functions at temperature and pressure profiles characteristic of the astrophysical scenarios proposed in this article, we obtained the most likely molecular formation routes of $H_2CO$ for the gas-phase. From this point of view, in diffuse molecular clouds the better positioned reactions are R27 - $^1CH_2 + {}^3O_2 \rightarrow {}^1H_2CO + \cdot O(^3P)$ and R28 - $^3CH_2 + {}^3O_2 \rightarrow {}^1H_2CO + \cdot O(^3P)$, while in dark, cold, and dense molecular clouds $H_2CO$ is dominated by R28 - $^3CH_2 + {}^3O_2 \rightarrow {}^1H_2CO + \cdot O(^3P)$ and R44 - $\cdot CH_3 + \cdot O(^1D) \rightarrow {}^1H_2CO + \cdot H$. In the hotter region III of circumstellar envelopes of low-mass, R45 - $\cdot CH_3 + \cdot O(^3P) \rightarrow {}^1H_2CO + \cdot H$ and R31 - $^1CH_2 + CO_2 \rightarrow {}^1H_2CO + CO$ are likely the most efficient productors of $H_2CO$, in region II, R44 - $\cdot CH_3 + O(^1D) \rightarrow {}^1H_2CO + \cdot H$ and R45 - $\cdot CH_3 + \cdot O(^3P) \rightarrow {}^1H_2CO + \cdot H$ are the most favored, while in the farthest and colder region I, R27 - $^1CH_2 + {}^3O_2 \rightarrow {}^1H_2CO + \cdot O(^3P)$ and R28 - $^3CH_2 + {}^3O_2 \rightarrow {}^1H_2CO + \cdot O(^3P)$, likely represent the two dominant molecular mechanisms in the formation of formaldehyde for the gas-phase.

According to these computational results, in an early evolutive state of DMCs with a gas density ~100 cm$^{-3}$ at a temperature

of ~100 K, and a pressure of $6.9 \times 10^3$ K cm$^{-3}$, in which UV radiation (13.60 eV at most) dominates the gas-phase reactions energetically, the main mechanisms to produce $H_2CO$ seem to be dictated by excited singlet ($CH_2(a^1A_1)$) and triplet ground-state ($\cdot CH_2(X^3B_1)$) methylene, which both combine with the ground triplet-state oxygen of $O_2(^3\Sigma_g^-)$. When the cloud collapses and reaches particle densities from $10^3$ to $10^6$ cm$^{-3}$ and an averaged gas temperature and pressure of $\tilde{1}3.2$ K and $5.3 \times 10^4$ K cm$^{-3}$ accompanied by a surrounding energy that does not exceed 4.18 eV, hydroxyl radical ($\cdot CH_3$) seems to be produced in the gas-phase, but from more elementary constituents, (Feuchtgruber et al. 2000) which generates a reduction of $CH_2(X^1B_1)$ abundance. Under these conditions, triplet methylene ($\cdot CH_2(X^3B_1)$) combined with the triplet ground-state oxygen $O_2(^3\Sigma_g^-)$ is probably the main mechanism responsible for $H_2CO(^1A_1)$ production followed by the union between methyl radical ($\cdot CH_3$) and singlet atomic oxygen ($O(^1D)$). After the DMC gravitationally collapses, and if the cloud mass is one or two times the solar system mass (~$2 \times 10^{30}$ Kg), a new astrophysical solar-like system composed of one or two YSOs with the corresponding circumstellar envelope of gas and dust is created (the astrophysical conditions of IRAS 16293 were used as a model for our computations). At 150 AU from the core, with temperatures and pressures close to 150 K and $6.08 \times 10^8$ K cm$^{-3}$, there is a region of the disk where abundances of o-$H_2CO$ the typical abundances of cold regions exceed by 2–3 orders of magnitude. This $H_2CO$ is composed of o-$H_2CO$ that is depleted from icy grain mantles and the para nuclear isomer, which is thought to be formed in a pure gas-phase. This zone is relatively poor in abundances of potential reagents to produce $H_2CO$ in the gas-phase. Consequently, the possibilities of its formation are quite limited. The most probable reactions that can produce para-$H_2CO$ in sufficient quantities are those composed of the methyl radical ($\cdot CH_3(^2A_2")$) and triplet ground-state $O_I$ ($\cdot O(^3P)$) followed by a hypothetical reaction between $CH_2(a^1A_1)$ and $CO_2(^1\Sigma_g^+)$. At 700 AU from the core, a new region appears in which formaldehyde is present. This time, the abundances decrease by approximately two orders of magnitude compared to the hotter region (see Fig. 4). This effect is thought to occur because o-$H_2CO$ is not fully evaporated from the grains, but a portion of it is present in the gas-phase. o-$H_2CO$ evaporation starts at about 40 K and stops at around 80–90 K (see Fig. 3). The thermal energy emanating from the YSO was determined to be ~50 kcal mol$^{-1}$, which reduces the gas temperature and pressure to ~80 K and $7.06 \times 10^7$ K cm$^{-3}$. According to our calculations, reactions based on the methyl radical ($\cdot CH_3$) with $\cdot O(^1D)$ and $\cdot O(^3P)$ might be the main gas-phase supplier site of $H_2CO$ in this region. Far from the core at ~4000 AU, there is a region in which dust grain mantles are abundant (candidates for protoplanet formation), the temperature and pressure do not exceed ~20 K and $2.29 \times 10^7$ K cm$^{-3}$, and the action of thermal energy emanating from the core is practically negligible. Consequently, this environment contains not enough energy to activate even very low barriers for chemical reactions in the gas-phase. Therefore the $H_2CO$ formation in the gas-phase can be led by ($CH_2(a^1A_1)$) and ($\cdot CH_2(X^3B_1)$), combined with the ground triplet oxygen $O_2(^3\Sigma_g^-)$, which does not require any external source of energy because their transition state is submerged, as we have already mentioned.

In this way and according to our computations, the most probable carbonaceous precursors for the gas-phase production of neutral $H_2CO$ in cold regions of space (ordered by importance) are: $CH_2(a^1A_1)$, $\cdot CH_2(X^3B_1)$ and $\cdot CH_3(^2A_2")$. The states of just before, during, and immediately after gravitational collapses and stellar main-sequence forming processes requires further studies.

*Acknowledgements.* J.C.R.O. wishes to thank all the staff of the Mississippi Center for Supercomputing Research (MCSR) at the University of Mississippi, in Oxford, MS, USA for their availability, and commitment. Additionally, thanks are given to Prof. Emilio J. Martínez-Núñez from Chemical Physics Department of Universidad de Santiago de Compostela (Spain) for his recommendations regarding the AUTOMEKIN program (priv. comm.). R.C.F. also acknowledges funding from NASA grant NNX17AH15G and start-up funds provided by the University of Mississippi. MCSR funding has been provided in part by NSF grant OIA-1757220.

## References

Adler, T., Knizia, G., & Werner, H. 2007, J. Chem. Phys., 127, 221106
Agúndez, M., Cernicharo, J., & Guélin, M. 2015, A&A, 577, L5
Aguilar, A., Ajello, J., Mangina, R., et al. 2008, ApJS, 177, 388
Aikawa, Y., Wakelam, V., Garrod, R., & Herbst, E. 2008, ApJ, 674, 984
Aikawa, Y., Furuya, K., Nomura, H., & Qi, C. 2015, ApJ, 807, 120
Atkinson, R., Baulch, D., Cox, R., et al. 2006, Atmos. Chem. Phys., 6, 3625
Ballesteros-Paredes, J., Vázquez-Semadeni, E., & Scalo, J. 1999, ApJ, 515, 286
Barone, V., Latouche, C., Skouteris, D., et al. 2015, MNRAS, 453, L31
Baulch, D., Cobos, C., Cox, R., et al. 1992, J. Phys. Chem. Ref. Data, 21, 411
Becke, A. 1988, Phys. Rev. A, 38, 3098
Blair, S., Magnani, L., Brand, J., & Wouterloot, J. 2008, Astrobiology, 8, 59
Bley, U., Temps, F., Wagner, H., & Wolf, M. 1992, Berichte der Bunsengesellschaft für physikalische Chemie, 96, 1043
Blitz, M., & Seakins, P. 2012, Chem. Soc. Rev., 41, 6318
Böhland, T., Temps, F., & Wagner, H. 1984, Berichte der Bunsengesellschaft für physikalische Chemie, 88, 455
Bok, B., & Reilly, E. 1947, ApJ, 105, 255
Bonnor, W. 1956, Web of Science, 41
Bottinelli, S., Wakelam, V., Caux, E., et al. 2014, MNRAS, 441, 1964
Bourke, T., Hyland, A., & Robinson, G. 1995, MNRAS, 276, 1052
Burke, M., Dimpfl, W., Sheaffer, P., Zittel, P., & Bernstein, L. 1996, J. Phys. Chem., 100, 138
Butlerow, A. 1861, Justus Liebigs Annalen der Chemie, 120, 295
Cassen, P., & Moosman, A. 1981, Icarus, 48, 353
Carty, D., Goddard, A., Köhler, S., Sims, I., & Smith, I. 2005, J. Phys. Chem. A, 110, 3101
Ceccarelli, C., Castets, A., Loinard, L., Caux, E., & Tielens, A. 1998, A&A, 338, L43
Ceccarelli, C., Loinard, L., Castets, A., Tielens, A., & Caux, E. 2000, A&A, 357, L9
Ceccarelli, C., Loinard, L., Castets, A., et al. 2001, A&A, 372, 998
Ceccarelli, C., Vastel, C., Tielens, A., et al. 2002, A&A, 381, L17
Cecchi-Pestellini, C., Casu, S., & Scappini, F. 2001, MNRAS, 326, 1255
Choughuley, A., Subbaraman, A., Kazi, Z., & Chadha, M. 1975, Origins of life, 6, 527
Cleaves II, H. 2008, Precambrian Res., 164, 111
Cody, G., Heying, E., Alexander, C., et al. 2011, Proc. Natl. Acad. Sci., 108, 19171
Combes, F., & Pineau des Forets, G. 1999, H2 in Space (USA: NASA)
Coutens, A., Ligterink, N., Loison, J., et al. 2019, A&A, 623, L13
Crimier, N., Ceccarelli, C., Maret, S., et al. 2010, A&A, 519, A65
Darwin, D., Young, A., Johnston, H., & Moore, C. 1989, J. Phys. Chem., 93, 1074
Delidovich, I., Simonov, A., Taran, O., & Parmon, V. 2014, ChemSusChem, 7, 1833
d'Hendecourt, L., Allamandola, L., Grim, R., & Greenberg, J. 1986, A&A, 158, 119
Dickens, J., & Irvine, W. 1999, AJ, 518, 733
Dickman, R. 1977, Sci. Am., 236, 66
Di Francesco, J., Hogerheijde, M., Welch, W., & Bergin, E. 2002, AJ, 124, 2749
Doty, S., Schöier, F., & Van Dishoeck, E. 2004, A&A, 418, 1021
Douglas, K., Blitz, M., Feng, W., et al. 2018, Icarus, 303, 10
Dunning, Jr, T. 1989, J. Chem. Phys., 90, 1007
Ebert, R. 1955, Z. Astrophys., 37, 217
Eschenmoser, A. 1994, Orig Life Evol. Biosph., 24, 389
Feuchtgruber, H., Helmich, F., van Dishoeck, E., & Wright, C. 2000, ApJ, 535, L111
Frisch, M., Trucks, G., Schlegel, H., et al. 2016, Gaussian Inc. Wallingford CT, 1
Fukui, K. 1981, Acc. Chem. Res., 14, 363
Furukawa, Y., Chikaraishi, Y., Ohkouchi, N., et al. 2019, Proc. Natl. Acad. Sci., 116, 24440

Gans, B., Boyé-Péronne, S., Broquier, M., et al. 2011, Phys. Chem. Chem. Phys., 13, 8140
Goicoechea, J., & Cernicharo, J. 2001, ApJ, 554, L213
Goldman, A., Murcray, F., Gillis, J., & Murcray, D. 1981, ApJ, 248, L133
Goldsmith, P., Melnick, G., Bergin, E., et al. 2000, ApJ, 539, L123
Guzmán, V., Pety, J., Goicoechea, J., Gerin, M., & Roueff, E. 2011, A&A, 534, A49
Guzmán, V., Goicoechea, J., Pety, J., et al. 2013, A&A, 560, A73
Hasegawa, T., & Herbst, E. 1993, MNRAS, 261, 83
Hill, J., & Peterson, K. 2010, Phys. Chem. Chem. Phys., 12, 10460
Hily-Blant, P., Maret, S., Bacmann, A., et al. 2010, A&A, 521, L52
Hohenberg, P., & Kohn, W. 1964, Phys. Rev, 136, B864
Hollis, J., Jewell, P., & Lovas, F. 1995, AJ, 438, 259
Hund, F. 1925, Z. Phys., 33, 855
Hund, F. 1927, Zeitschrift für Physik, 43, 788
Jaber, A., Ceccarelli, C., Kahane, C., & Caux, E. 2014, ApJ, 791, 29
Jasper, A., Klippenstein, S., & Harding, L. 2007, J. Phys. Chem., 111, 8699
JØrgensen, J., Favre, C., Bisschop, S., et al. 2012, ApJ, 757, L4
Jungen, C., & Glass-Maujean, M. 2016, Phys. Rev. A, 93, 032514
Kaminsky, J., Mata, R., Werner, H., & Jensen, F. 2008, Mol. Phys., 106, 1899
Kandori, R., Nakajima, Y., Tamura, M., et al. 2005, AJ, 130, 2166
Klessen, R., & Glover, S. 2014, Physical Processes in the Interstellar Medium (Honoken: Wiley)
Knizia, G., Adler, T., & Werner, H. 2009, J. Chem. Phys., 130, 054104
Kohn, W., & Sham, L. 1965, Phys. Rev., 140, A1133
Lakshmanan, S., Pratihar, S., & Hase, W. 2019, J. Phys. Chem., 123, 4360
Larralde, R., Robertson, M., & Miller, S. 1995, Proc. Natl. Acad. Sci., 92, 8158
Larsson, B., Liseau, R., Pagani, L., et al. 2007, A&A, 466, 999
Launhardt, R., Nutter, D., Ward-Thompson, D., et al. 2010, ApJ, 188, 139
Lazcano, A., & Miller, S. 1996, Cell, 85, 793
Leopold, D., Murray, K., Stevens Miller, A., & Lineberger, W. 1985, J. J. Chem. Phys., 83, 4866
Linstrom, P., & Mallard, W., eds. 1997, NIST Chemistry WebBook, NIST Standard Reference Database 69 (Gaithersburg: National Institute of Standards and Technology)
Liseau, R., Goldsmith, P., Larsson, B., et al. 2012, A&A, 541, A73
Liszt, H., & Lucas, R. 1995, A&A, 299, 847
Liszt, H., Lucas, R., & Pety, J. 2006, A&A, 448, 253
Liszt, H., Pety, J., Gerin, M., & Lucas, R. 2014, A&A, 564, A64
Lodriguito, M., Lendvay, G., & Schatz, G. 2009, J. Chem. Phys., 131, 224320
Loew, O. 1889, Berichte der deutschen chemischen Gesellschaft, 22, 478
Maciel, W. 2013, Astrophysics of the Interstellar Medium (Berlin: Springer)
Mangum, J., Darling, J., Menten, K., & Henkel, C. 2008, ApJ, 673, 832
Maret, S. 2003, SF2A-2003: Semaine de l'Astrophysique Française, meeting held in Bordeaux, France, June 16-20, 2003, eds. F. Combes, D. Barret, T. Contini, & L. Pagan (EdP-Sciences, Conference Series), 191
Marka, C., Schreyer, K., Launhardt, R., Semenov, D., & Henning, T. 2011, A&A, 537, A4
Marmet, P. 2000, 21st Century Science and Technology, 13, 5
Martínez-Núñez, E. 2015a, J. Comput. Chem., 36, 222
Martínez-Núñez, E. 2015b, Phys. Chem. Chem. Phys., 17, 14912
Martin, R., & Barrett, A. 1978, ApJS, 36, 1
McGuire, B. 2018, ApJS, 239, 17
Meinert, C., Myrgorodska, I., de Marcellus, P., et al. 2016, Science, 352, 208
Menor-Salván, C., ed. 2018, Prebiotic Chemistry and Chemical Evolution of Nucleic Acids (Berlin: Springer International Publishing)
Meyer, D., Cardelli, J., & Sofia, U. 1997, AJ, 490, L103
Miller, S. 1953, Science, 117, 528
Millar, T. J., Duley, W. W., & Williams, D. A. 1979, MNRAS, 186, 685
Minn, Y., & Greenberg, J. 1979, A&A, 77, 37
Miyazaki, T., Nagasaka, S., Kamiya, Y., & Tanimura, K. 1993, J. Phys. Chem., 97, 10715
Möller, C., & Plesset, M. S. 1934, Phys. Rev., 46, 618
MOPAC2016 2016, Stewart Computational Chemistry, Colorado Springs, CO, USA
Muhle, S., Seaquist, E. R., & Henkel, C. 2007, ApJ, 671, 1579
Muncaster, R. 1979, Arch. Ration. Mech. Anal., 70, 79
Noble, J. A., Theule, P., Mispelaer, F., et al. 2012, A&A, 543, A5
Ohishi, M., Irvine, W., Kaifu, N., & Singh, P. 1992, IAU Symp., 150, 171
Oró, J., Kimball, A., Fritz, R., & Master, F. 1959, Arch. Biochem. Biophys., 85, 115
Palmer, P., Zuckerman, B., Buhl, D., & Lewis, E. 1969, ApJ, 156, L147
Parise, B., Du, F., Liu, F., et al. 2012, A&A, 542, L5
Park, J. H., Lee, J. W., Sim, K. J., Han, J. W., & Yi, W. K. 2008, Bull. Korean Chem. Soc., 29(1), 177
Persson, M. V., JØrgensen, J. K., Müller, H. S. P., et al. 2018, A&A, 610, A54
Peterson, K., Adler, T., & Werner, H. 2008, J. Chem. Phys., 128, 084102
Pezzella, M., Koner, D., & Meuwly, M. 2020, J. Phys. Chem. Lett., 11, 2171
Polehampton, E., Menten, K., Brünken, S., Winnewisser, G., & Baluteau, J. 2005, A&A, 431, 203
Rickard, L. J., Palmer, P., Buhl, D., & B., Z. 1977, ApJ, 213, 654
Ridgway, S. T., Hall, D. N., Kleinmann, S. G., Weinberger, D. A., & Wojslaw, R. S. 1976, Nature, 264, 345
Rivilla, V., Beltrán, M., Vasyunin, A., et al. 2018, MNRAS, 483, 806
Rodríguez, A., Rodríguez-Fernández, R., Vázquez, S., et al. 2018, J. Comput. Chem., 39, 1922
Roueff, E., Dartois, E., Geballe, T., & Gerin, M. 2006, A&A, 447, 963
Rowlinson, J. 2005, Mol. Phys., 103, 2821
Ruiz-Mirazo, K., Briones, C., & de la Escosura, A. 2014, Chem. Rev., 114, 285
Sakai, N., Sakai, T., Hirota, T., & Yamamoto, S. 2009, ApJ, 702, 1025
Sakai, N., Shirley, Y., Sakai, T., et al. 2012, ApJ, 758, L4
Schöier, F., Jörgensen, J., van Dishoeck, E., & Blake, G. 2002, A&A, 390, 1001
Schlegel, H. 1982, J. Comput. Chem., 3, 214
Schwarz, K., & Bergin, E. 2014, ApJ, 797, 113
Sheffer, Y., Lambert, D., & Federman, S. 2002, ApJ, 574, L171
Sheffer, Y., Rogers, M., Federman, S., et al. 2008, ApJ, 687, 1075
Shuter, W. 1982, The Milky Way (Berlin: Springer), 6, 171
Snow, T., & McCall, B. 2006, ARA&A, 44, 367
Snyder, L., Buhl, D., Zuckerman, B., & Palmer, P. 1969, Phys. Rev. Lett., 22, 679
Snyder, L., Kuan, Y., Ziurys, L., & Hollis, J. 1993, ApJ, 403, L17
Spitzer, Jr., L. 1998, Physical Processes in the Interstellar Medium (Hoboken: Wiley-Interscience), 227
Stewart, J. 2013, J. Mol. Modeling, 19, 1
Tang, X. D., Henkel, C., Menten, K. M., et al. 2017, A&A, 598, A30
Tielens, A., & Whittet, D. 1997, Symp. Int. Astron. Union, 178, 45
Tsang, W., & Hampson, R. 1986, J. Phys. Chem. Ref. Data, 15, 1087
Turner, B. 1995, ApJ, 449, 635
van der Tak, F., van Dishoeck, E., & Caselli, P. 2000, A&A, 361, 327
van der Wiel, M. H. D., Jacobsen, S. K., Jörgensen, J. K., et al. 2019, A&A, 626, A93
van Dishoeck, E. 2014, Faraday Discuss., 168, 9
van Dishoeck, E., Blake, G., Jansen, D., & Groesbeck, T. 1995, ApJ, 447, 760
Vasyunin, A., & Herbst, E. 2013, ApJ, 769, 34
Velusamy, T., Langer, W. D., Goldsmith, P. F., & Pineda, P. F. 2017, AJ, 838, 165
Wang, Y., Evans, N. J., Zhou, S., & Clemens, D. P. 1995, ApJ, 454, 217
Wang, J., Liu, K., Min, Z., et al. 2000, J. Chem. Phys., 113, 4146
Ward-Thompson, D., Motte, F., & André, P. 1999, MNRAS, 305, 143
Werner, H., Knowles, P., Manby, F., et al. 2020, J. Chem. Phys., 152, 144107
Wiebe, D. Z., Kirsanova, M. S., Shustov, B. M., & Pavlyuchenkov, Y. N. 2008, Astron. Rep., 52, 976
Wiesemeyer, H., Güsten, R., Heyminck, S., et al. 2012, A&A, 542, L7
Wooden, D., Charnley, S., & Ehrenfreund, P. 2004, Composition and Evolution of Interestellar Clouds (Tucon: University of Arizona Press), 33
Woon, D. 2002, ApJ, 569, 541
Yamamoto, S. 2017, Introduction to Astrochemistry (Tokypo: Springer), 65
Zhixing, C. 1989, Theor. Chim. Acta., 75, 481
Ziurys, L., Hollis, J., & Snyder, L. 1994, ApJ, 430, 706
Zuckerman, B., Palmer, P., Snyder, L. E., & Buhl, D. 1969, Theor. Chim. Acta., 157, L167

## Appendix A: Main $H_2CO$ detection in space.

**Table A.1.** Main detection of Formaldehyde ($H_2CO$) and isotopologues in outer space in chronological order.

| Ref. | Astrophysical Object/s | Researcher(s) | Publication | Molecular Species |
|---|---|---|---|---|
| 1 | M17, W3, W3 (position OH), W49, NGC 2024, DR 21, W43, W44, W51, Sgr A, Sgr B2, W33, NGC 6334, Cas A and 3C 123 | L.E. Snyder, D. Buhl, B. Zuckerman, and P. Palmer | Phys. Rev. Lett. 22, 679–681 (1969) | $H_2CO$ |
| 2 | Heile´s Cloud 1, Cloud 2, Cloud 4, and L134 | P. Palmer, B. Zuckerman, D. Buhl, and L.E. Snyder | The Astrophysical Journal, Vol. 156, June 1969 | $H_2CO$ |
| 3 | Sgr A and Sgr B2 | B. Zuckerman, P. Palmer, L.E. Snyder, and D. Buhl. | The Astrophysical Journal, Vol. 157, September 1969 | $H_2{}^{13}CO$ |
| 4 | Sgr B2 | F.F.Gardner, J.C. Ribes, and B.F.C. Cooper | Astrophys. Lett. 157, 181–183 (1971) | $H_2C^{18}O$ |
| 5 | NGC 7538 | D. Downes and T.L. Wilson | The Astrophysical Journal, 191:L77-L78, 1974 July 15 | $H_2CO$ |
| 6 | NGC 2264, B68, B72, B133, B134, B227, B238, and B335 | L.J. Rickard, P. Palmer, D. Buhl, and B. Zuckerman | The Astrophysical Journal, 213:654-672, 1977 May 1 | $H_2CO$ |
| 7 | Dark clouds near NGC 2264 | Y.K. Minn, and J.M. Greenberg | Astronomy and Astrophysics vol. 77, p. 37-34 (1979) | $H_2CO$ |
| 8 | L134 N and Heiles's Cloud 2 (CLD2) of the TMC Complex | W.D. Langer, M.A. Frerking, R.A. Linke, and R.W. Wilson | The Astrophysical Journal, 232:L169-L173, 1979 September 15 | HDCO |
| 9 | Orion region: Lynds dust clouds L1630, 1641 and part of 1647 | R.J. Cohen, N. Matthews, R.W. Few, and R.S. Booth | Mon. Not. R. Astron. Soc. (United Kingdom); Journal Volume: 203:3. Feb. 01, 1984. | $H_2CO$ |
| 10 | Draco Nebula | U. Mebold, J. Cernicharo, L. Velden, K. Reif, C. Crezelius, and W. Goerigk | Astronomy and Astrophysics 151, 427-437 (1985) | $H_2CO$ |
| 11 | Four CO clouds in high galactic latitudes | A. Heithausen, U. Mebold, and H.W. de Vries | Astronomy and Astrophysics (ISSN 0004-6361), vol. 179, no. 1-2, June 1987, p. 263-267. | $H_2CO$ |
| 12 | Protoplanetary Nebula CRL 618 | J. Cernicharo, M. Guélin, J. Penalver, J. Martín-Pintado, and R. Mauersberger | Astron. Astrophys. 222, L1–L4 (1989) | $H_2CO$ |
| 13 | Orion KL | B.E. Turner | The Astrophysical Journal, 362:L29-L33,1990 October 10 | $D_2CO$ |
| 14 | NRAO 150-L1495: 4C+27.13, B219/3C 123, L1605-4C +10.20, L485-G24.8+0.1, L628-G37.8—0.2. | A.G. Nash | The Astrophysical Journal Supplement Series, 72:303-322,1990 February | $H_2CO$ |
| 15 | Comet LEVY (1990c) | F.P. Schloerb and W.G. Five | Asteroids, Comets, Meteors 1991, pp. 533-536 Lunar and Planetary Institute, Houston, 1992 | $H_2CO$ |
| 16 | Protoplanetary nebula OH231.8+4.2 | M. Lindqvist, H. Olofsson,A. Winnberg, L.A. Nyman | Astronomy and Astrophysics (ISSN 0004-6361), vol. 263, no. 1-2, p. 183-189 | $H_2CO$ |
| 17 | Comet 109P/Swift-Tuttle (1862 111) | D. Bockelée-Morvan, R. Padman, J.K. Davies and J. Crovisier | Planet. Space Sri., Vol. 42, No. 5, pp. 655662, 1994 | ortho $H_2CO$ |
| 18 | Comet C/1996 B2 (Hyakutake) | Biver et al. | THE ASTRONOMICAL JOURNAL, 118:1850 - 1872, 1999 October | ortho and para $H_2CO$ |
| 19 | Comet C/1999 H1 (LEE) | N. Biver, D. Bockelee-Morvan, J. Crovisier, F. Henry, J.K. Davies, H.E. Matthews, P. Colom, E.. Gerard, D.C. Lis, T.G. Phillips, F. Rantakyro, L. Haikala, and H.A. Weaver6 | THE ASTRONOMICAL JOURNAL, 120:1554È1570, 2000 September | $H_2CO$ |
| 20 | Massive young stars GL 2591, NGC 7538 IRS1 and NGC 7538 IRS9 | F.F.S. van der Tak , E.F. van Dishoeck , and P. Caselli | ASTRONOMY AND ASTROPHYSICS Thesaurus codes are: 09.13.2; 08.03.2; 08.06.2 | $H_2CO$ |
| 21 | Small cloud L1689N in the ρ Ophiuchus complex | C. Ceccarelli, C. Vastel, A.G.G.M. Tielens, A. Castets, A.C.A. Boogert4, L. Loinard5, and E. Caux | Astronomy and Astrophysics 381, L17–L20 (2002) | $D_2CO$, $H_2CO$ |
| 22 | IRAS 16293–2422 | F.L. Schoier, J.K. JØrgensen, E.F. van Dishoeck, and G.A. Blake | Astronomy and Astrophysics 390, 1001-1021 (2002) | o-$H_2CO$, p-$H_2CO$, o-$H_2{}^{13}CO$, p-$H_2{}^{13}CO$, o-HDCO, p-HDCO |
| 23 | NGC1333-IRAS4A, NGC1333-IRAS4B, NGC1333-IRAS2, L1448-MM, L1448-N, L1157-MM, L1527, VLA1623 and IRAS16293-2422 | S. Maret | EDP Sciences 2003 | ortho and para $H_2CO$; $H_2{}^{13}C^{16}O$ |
| 24 | Low-mass protostar IRAS 16293-2422 | S. Cazaux, A.G.G.M. Tielens, C. Ceccarelli, A. Castets, V. Wakelam, E. Caux, B. Parise, and D. Teyssier | The Astrophysical Journal, 593:L51–L55, 2003 August 10 | $H_2CO$ |
| 25 | CARBON STAR IRC +10216 | K.E. Saavik Ford, D.A. Neufeld, P. Schilke and G.J. Melnick | The Astrophysical Journal, 614:990–1006, 2004 October 20 | $H_2CO$ |
| 26 | NGC 1333-IRAS 4B, NGC 1333-IRAS 2, L1448-MM and L1527 | S. Maret, C. Ceccarelli, E. Caux, A.G.G.M. Tielens, J.K. JØrgensen4, E. van Dishoeck, A. Bacmann, A. Castets, B. Lefloch, L. Loinard, B. Parise, and F.L. Schöier | Astronomy and Astrophysics 416, 577-594 (2004) | ortho and para $H_2CO$ |
| 27 | Comets C/1995 O1 (HALE-BOPP), C/2002 T7 (LINEAR), AND C/2001 Q4 (NEAT) | S.N. Milam, A.J. Remijan and coworkers | The Astrophysical Journal, 649:1169–1177, 2006 October 1 | $H_2CO$ |
| 28 | High-mass protostar W33A and RAFGL 7009S | E. Roueff, E. Dartois, T.R. Geballe, and M. Gerin | Astronomy and Astrophysics 447, 963–969 (2006) | $H_2CO$ |
| 29 | M82 | S. Mühle and E.R. Seaquist and C. Henkel | The Astrophysical Journal, 671:1579Y1590, 2007 December 20 | p-$H_2CO$ |
| 30 | NGC 7293 | E. D. Tenenbaum, S.N. Milam, N.J. Woolf, and L.M. Ziurys | The Astrophysical Journal, 704:L108–L112, 2009 October 20 | $H_2CO$ |
| 31 | NGC 7538S | Göran Sandell, and M. Wright | arXiv.org > astro-ph > arXiv:1004.0643v1; Accepted by ApJ; 20 pages, 20 figures | $H_2CO$ |
| 32 | MON R2, S156, DR17/L906 and M17/M18 | X.D. Tang, J. Esimbek, J.J. Zhou, G. Wu, and D. Okoh | RAA 2014 Vol. 14 No. 8, 959–970 | $H_2CO$ |
| 33 | IK Tau | L. Velilla Prieto, C. Sánchez Contreras , J. Cernicharo , M. Agúndez, G. Quintana-Lacaci, V. Bujarrabal, J. Alcolea, C. Balança, F. Herpin, K. M. Menten, and F. Wyrowski | Astronomy and Astrophysics 597, A25 (2017) | ortho and para $H_2CO$ |
| 34 | HD 163296 | M.T. Carney, M.R. Hogerheijde, R.A. Loomis, V.N. Salinas, K.I. Öberg, C. Qi, and D.J. Wilner | Astronomy and Astrophysics 605, A21 (2017) | $H_2CO$ |
| 35 | Nearby T Tauri star TW Hya | K.I. Öberg, V.V. Guzmán, C.J. Merchantz, C. Qi, S.M. Andrews, L.I. Cleeves, J. Huang1, R.A. Loomis, D.J. Wilner, and C. Brinch | arXiv:1704.05133v1 [astro-ph.GA] 17 Apr 2017 | $H_2CO$ |
| 36 | IRAS 16293−2422 B | M.V. Persson, J.K. JØrgensen, H.S.P. Müller, A. Coutens, E.F. van Dishoeck, V. Taquet, H. Calcutt, M.H.D. van der Wiel, T.L. Bourke, and S. F. Wampfler | Astronomy and Astrophysics 610, A54 (2018) | $H_2CO$; $H_2{}^{12}C^{17}O$; $H_2C^{18}O$; $H_2{}^{13}CO$; HDCO; $HDC^{18}O$; $D_2CO$; $D_2{}^{13}CO$ |

## Appendix B: PES profiles of barrier-less reactions.

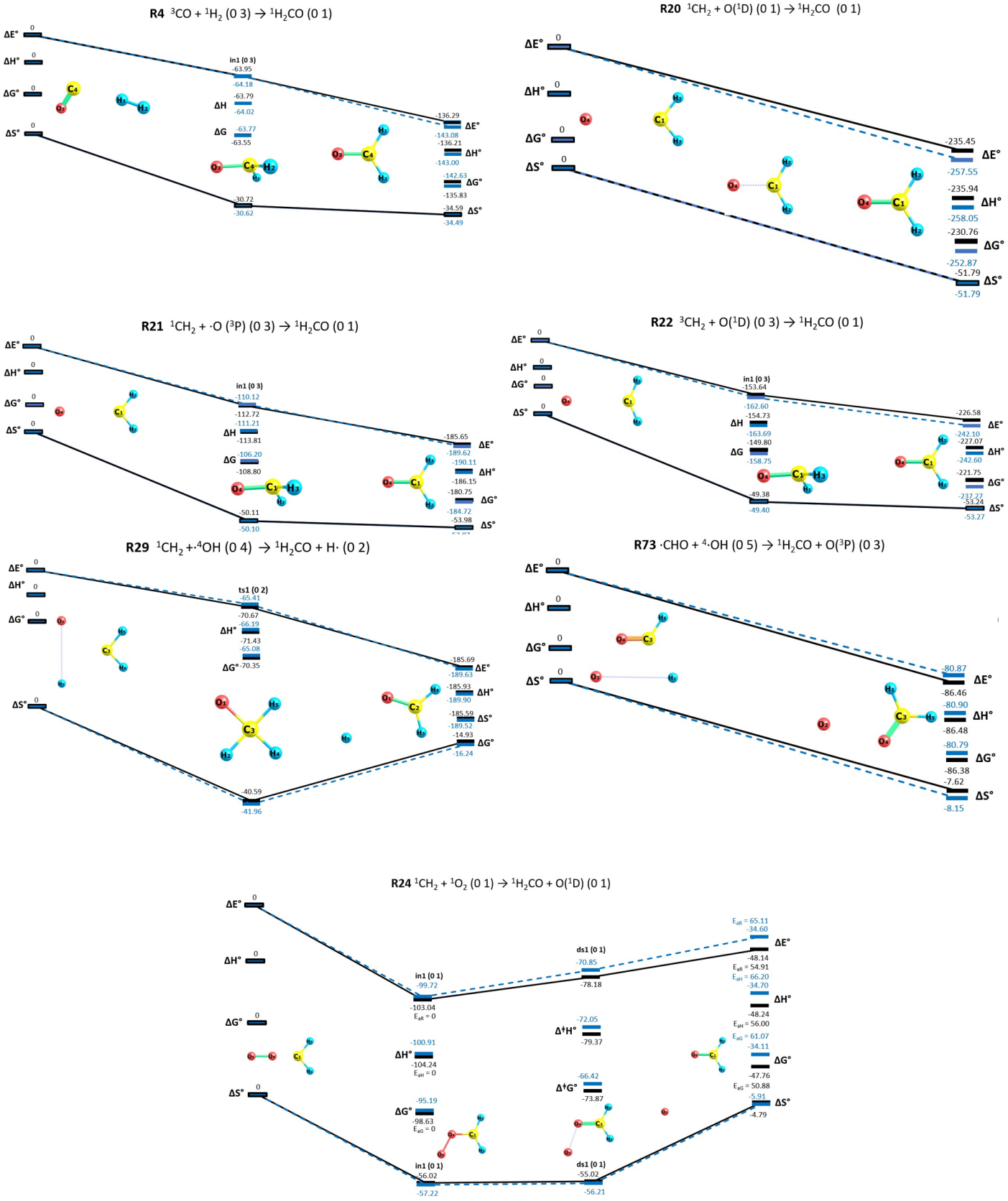


**Fig. B.1.** Barrier-less PES profile reactions. R4/R73 - $T_{gas}$ = 13.2 K, $P_{gas}$ = 5.30 x $10^4$ K cm$^{-3}$. R20/R21/R22 - $T_{gas}$ = 100 K, $P_{gas}$ = 6.90 x $10^3$ K cm$^{-3}$. R29 - $T_{gas}$ = 80 K, $P_{gas}$ = 7.06 x $10^7$ K cm$^{-3}$. Black lines CCSD(T)-F12/cc-pVTZ-F12, dotted blue lines MP2/aug-cc-pVDZ. ΔE°, ΔH°, ΔG°) units in kcal mol$^{-1}$, ΔS° in cal mol$^{-1}$ K$^{-1}$. In parentheses, charge, and spin multiplicity.

## Appendix C: Main excited reactants and intermediates.

**$O_1(^1D)$**


| Normal Modes | Position ($cm^{-1}$) | Molecular Energy (H) | ZPE (H) |
|---|---|---|---|
| n/a | n/a | -74.921351323 | n/a |
| **Atom** | **X** | **Y** | **Z** |
| O | 0.000000000 | 0.000000000 | 0.000000000 |

**$O_2(^1\Delta_g)$**

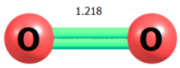


| Normal Modes | Position ($cm^{-1}$) | Molecular Energy (H) | ZPE (H) |
|---|---|---|---|
| *w1 (Ag)* | 1506.73 | -150.144630207 | 0.00343258 |
| **Atom** | **X** | **Y** | **Z** |
| O | 0.000000000 | 0.000000000 | -0.609141989 |
| O | 0.000000000 | 0.000000000 | 0.609141989 |

**·OH($^4\Pi$)**


| Normal Modes | Position ($cm^{-1}$) | Molecular Energy (H) | ZPE (H) |
|---|---|---|---|
| *w1 (A1)* | 68.78 | -75.500748147 | 0.00015669 |
| **Atom** | **X** | **Y** | **Z** |
| O | 0.000000000 | 0.000000000 | -0.19852207 |
| H | 0.000000000 | 0.000000000 | 3.151213371 |

**CO($^3\Pi$)**

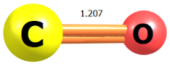


| Normal Modes | Position ($cm^{-1}$) | Molecular Energy (H) | ZPE (H) |
|---|---|---|---|
| *w1 (A1)* | 1746.22 | -112.977859629 | 0.00397818 |
| **Atom** | **X** | **Y** | **Z** |
| C | 0.000000000 | 0.000000000 | -0.689690279 |
| O | 0.000000000 | 0.000000000 | 0.517761288 |

**$CH_2(^1A_1)$**

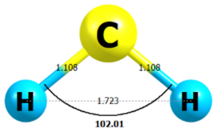


| Normal Modes | Position ($cm^{-1}$) | Molecular Energy (H) | ZPE (H) |
|---|---|---|---|
| *w1 (A')* | 1401.25 | -39.075088704 | 0.01668209 |
| *w2 (A')* | 2923.5 | | |
| *w3 (A')* | 2997.84 | | |
| **Atom** | **X** | **Y** | **Z** |
| C | 0.000000000 | 0.000000000 | 0.000000000 |
| H | 0.000000000 | 0.697448107 | 0.861406961 |
| H | 0.000000000 | 0.697454778 | -0.86139734 |

**$H_2CO(^3\Pi)$**

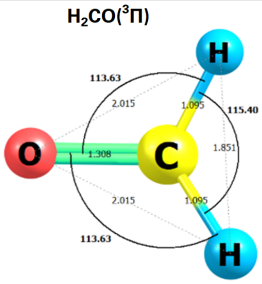


| Normal Modes | Position ($cm^{-1}$) | Molecular Energy (H) | ZPE (H) |
|---|---|---|---|
| *w1 (A)* | 756.9 | -114.263082116 | 0.0233965 |
| *w2 (A)* | 881.12 | | |
| *w3 (A)* | 1267.26 | | |
| *w4 (A)* | 1311.27 | | |
| *w5 (A)* | 2971.54 | | |
| *w6 (A)* | 3081.79 | | |
| **Atom** | **X** | **Y** | **Z** |
| C | 0.000000000 | 0.000000000 | 0.000000000 |
| H | -0.289533074 | 0.508520413 | 0.925645657 |
| H | -0.289531172 | 0.508538577 | -0.925636271 |
| O | -0.266140539 | -1.281112689 | -0.000012841 |

**$H_2COO(^3\Pi)$**

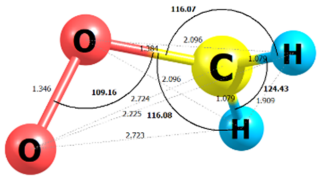


| Normal Modes | Position ($cm^{-1}$) | Molecular Energy (H) | ZPE (H) |
|---|---|---|---|
| *w1 (A)* | 40.88 | -189.348061221 | 0.027773921 |
| *w2 (A)* | 372.89 | | |
| *w3 (A)* | 617.06 | | |
| *w4 (A)* | 1018.59 | | |
| *w5 (A)* | 1090.16 | | |
| *w6 (A)* | 1117.64 | | |
| *w7 (A)* | 1466.75 | | |
| *w8 (A)* | 3156.95 | | |
| *w9 (A)* | 3310.41 | | |
| **Atom** | **X** | **Y** | **Z** |
| C | 0.000000000 | 0.000000000 | 0.000000000 |
| H | -0.003336534 | -0.002667973 | 1.079001957 |
| H | 0.891894855 | 0.001947089 | -0.60727344 |
| O | -1.152513728 | 0.461981965 | -0.610636523 |
| O | -1.147836834 | 1.808065872 | -0.602404932 |

**tras-HCOH($^3\Pi$)**

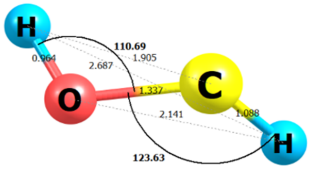


| Normal Modes | Position ($cm^{-1}$) | Molecular Energy (H) | ZPE (H) |
|---|---|---|---|
| *w1 (A)* | 410.18 | -114.25807303 | 0.02469868 |
| *w2 (A)* | 1095.47 | | |
| *w3 (A)* | 1181.12 | | |
| *w4 (A)* | 1297.28 | | |
| *w5 (A)* | 3104.32 | | |
| *w6 (A)* | 3753.10 | | |
| **Atom** | **X** | **Y** | **Z** |
| O | -1.318376702 | -0.221868253 | -0.035589951 |
| C | 0.000000000 | 0.000000000 | 0.000000000 |
| H | -1.558532622 | -0.943222007 | 0.557418861 |
| H | 0.456869746 | 0.833951184 | 0.529635829 |

**Fig. C.1.** Calculated infrared-band positions ($cm^{-1}$), individual molecular and ZPE energies (Hartrees), and spatial coordinates of the main excited reactants and intermediates (as mentioned in sections 4.4 and 4.5). Calculations at the CCSD(T)-F12/cc-pVTZ-F12 level of theory and basis set, angles in sexagesimal degrees, and inter-atomic distances in Angstroms (Å).